Pontificia Universidad Católica de Chile
Instituto de Física
Facultad de Física

Spontaneous formation in air of DPPC Supported Lipid Bilayers (SLBs) evaporated in a solvent free process on silicon substrates

By

Marcelo Cisternas Fruns

A dissertation presented to the Faculty of Physics at
Pontificia Universidad Católica de Chile
in partial fulfillment
of the requirements for the degree
Doctor en Física

Supervisor : Dr. Ulrich G. Volkmann
Examining Committee : Dr. Griselda García
Dr. Donovan Díaz
Dr. Tomás Pérez-Acle

June 2021

Acknowledgements

I would like to thank to my advisor, Professor Dr. Ulrich G. Volkmann for his support and patience during this process and his laboratory group SurfLab UC specially to M. J. Retamal, N. Moraga, F. Palacios, S. Molina, N. Gomez, H. Zelada and T. P. Corrales for all contributions that they did to my thesis.

I want to give special thanks to my family, Andrea, Matilde and Katalí for their unconditional support through the difficult moments.

Finally, I would like to thank CONICYT (ANID) for their financial support of my PhD degree scholarship and the FONDECYT grant numbers 1141105 y 1180939.

Table of contents

List of Figures

List of Tables:

Abstract

Artificial membranes are models for biological systems and are important to gain deeper insight into biological membranes and for various applications. We introduce a dry two-step self-assembly method consisting of the high-vacuum evaporation of phospholipid molecules over silicon, followed by a subsequent annealing step in air. We evaporate dipalmitoylphosphatidylcholine (DPPC) molecules over bare silicon without the use of polymer cushions or solvents. High-resolution ellipsometry and AFM temperature-dependent measurements are performed in air to detect the characteristic phase transitions of DPPC bilayers. Complementary AFM force-spectroscopy breakthrough events are induced to detect single- and multi-bilayer formations. These combined experimental methods confirm the formation of stable non-hydrated lipid bilayers with phase transitions between gel to ripple phases at 311.5 ± 0.9 K, ripple to liquid crystalline phases at 323.8 ± 2.5 K and liquid crystalline to fluid disordered phases at 330.4 ± 0.9 K, which was consistent with such structures reported in wet environments. We find that the AFM tip induces a restructuring or intercalation of the bilayer that is strongly related to the applied tip-force. These dry supported lipid bilayers show long-term stability. These findings are relevant for the development of functional biointerfaces, specifically for fabrication of biosensors and membrane protein platforms. The observed stability is relevant in the context of lifetimes of such systems protected by bilayers in dry environments, such as e.g. SARS-CoV-2 virus.

Graphical Abstract

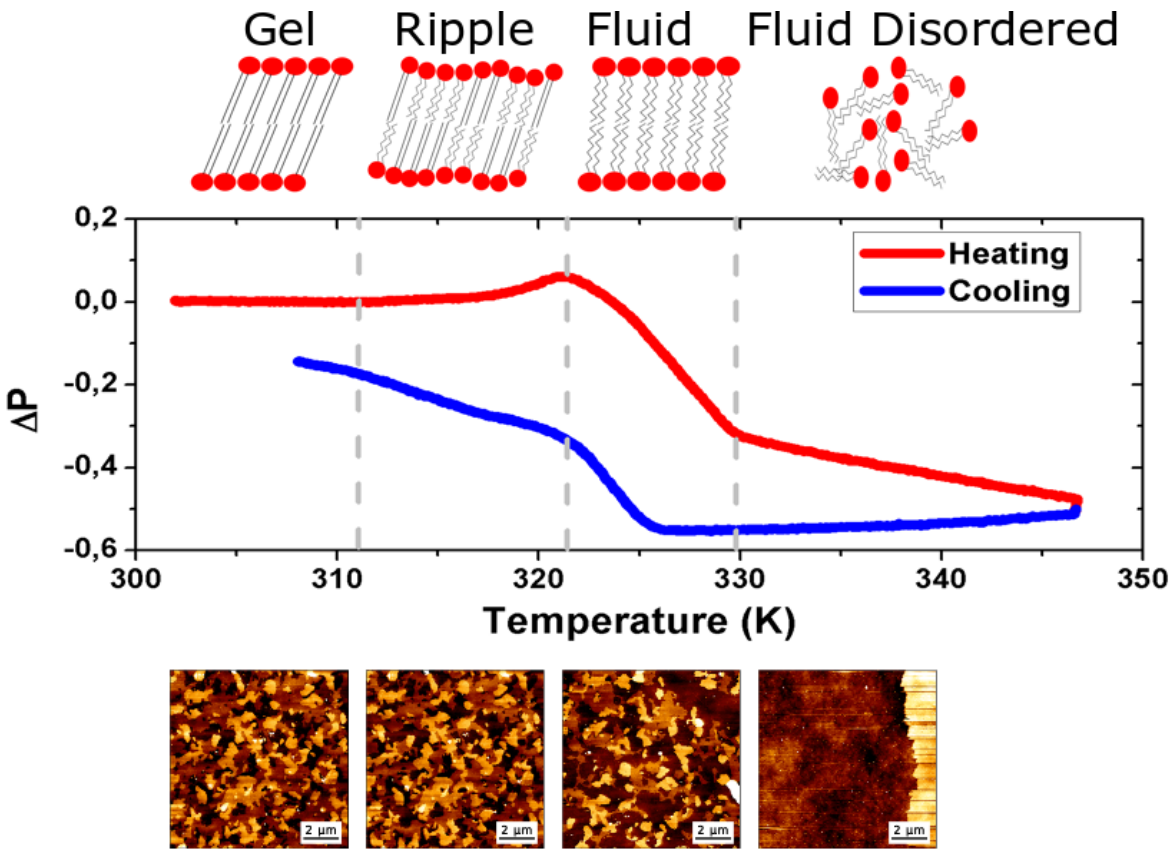

KEYWORDS: *Supported Lipid Bilayers, Atomic Force Microscopy, Very High Resolution Ellipsometry, Physical Vapor Deposition, Artificial Membranes, Bio-Silica Interfaces*

Significance

In this study, we found strong evidence for the formation of stable membranes of supported phospholipid bilayers (SLBs) evaporated directly onto SiO_2/Si, without further hydration. Previously, it has been shown via Raman Spectroscopy that the evaporation process under high vacuum does not alter the chemical composition of the molecules. For each sample eight temperature cycles from room temperature to the liquid phase were performed. After one or two temperature cycles the characteristic phase transitions of the SLBs were observed in air with Very High Resolution Ellipsometry. The common microscopic model of Dignam and Fedyk was used for data interpretation. With Atomic Force Microscopy, we observed the rupture force of the supported DPPC bilayers. The membranes exhibited force-dependent dynamics when imaged by Atomic Force Microscopy.

1.Introduction

1.1. Motivation

The study of the behavior of artificial membranes has gained importance in recent times [1]–[3], because they represent models of behavior analogous to biological membranes found in nature. Such biological membranes are the basis of cellular membrane structures and their principal function is to maintain the equilibrium of the interior of the cell (intracellular medium) with the exterior of the cell (extracellular medium). The principal component of the cell membrane are lipids and proteins that alter their behavior in response to a physical or chemical stimuli.

The formation and study of an adequate environment that permits us to form stable artificial membranes, is the principal motivation of this thesis. Our previous studies have shown that such membranes can be evaporated in high vacuum [4], but the stabilization and the activation of the system are not widely studied and such understanding would form an important (fundamental) step towards the development of bionanosensors [5], [6].

Bionanotechnology is an emerging field that combines nanoscale technologies with biological systems in order to create functional devices with different applications such as: drug delivery, biosensors, carriers of small molecules and templates for pharmaceutical designs [7]–[10]. A cornerstone material in the semiconductor industry and nanotechnology is silicon. An important goal for bionanotechnology is to create potential silicon-based chips that biomimic the cell membrane, i.e. a bio-silica interface

[11]–[14]. Such a bio-silica interface could be used to study the insertion of proteins within membranes. A first step to mimicking the cell membrane over a solid surface is to form phospholipid bilayers, which are referred to as a Supported Lipid Bilayers (SLB) [15]. One method to form a SLB is by using small vesicles, which are suspended in water and set to interact with a silicon surface. Once the vesicles interact with the hydrophilic silicon surface, they self-assemble into a SLB [16]. There have been many studies reporting different methods to form SLBs from vesicles, such as polymer cushioned lipid bilayers [17]–[20], hybrid bilayers supported over alkane-thiol self-assembled monolayers (SAM) [21], [22], tethered lipid bilayers [23], [24] and freely suspended bilayers [25], [26]. Another method to form SLBs, without starting from a vesicle, is by using the Langmuir-Blodgett trough method [27]–[29], where a solid substrate is successively immersed within a compressed layer of lipids, which then assemble at a liquid-air interface. Furthermore, a recent solvent-assisted method using isopropanol has been reported to form SLB, where lipid molecules are dissolved in isopropanol and flowed through a liquid reaction chamber, generating a bilayer over a glass slide [30]. All the aforementioned methods involve the use of solvents to dissolve lipid molecules, transport small vesicles or assemble a transfer monolayer over liquid-air interfaces. A main disadvantage of liquid-based methods is that they are dependent on specific phospholipid and solvent type, concentration and surface tension between the liquid-solid interface.

Work towards the creation of a solvent-free bio-silica interface has been reported by Retamal et al. (2014), who have shown that supported bilayers of Dipalmitoylphosphatidylcholine (DPPC) can be evaporated from their vapor phase over a cushion of chitosan, which is also previously evaporated onto the substrate [4]. Using Raman Spectroscopy, Retamal et al. showed that the evaporation process did not alter the chemical composition of the molecules [4]. Furthermore, ellipsometric measurements of these DPPC/Chitosan/SiO_2/Si samples in air, previously hydrated with a drop of water, showed evidence of gel to ripple, ripple to liquid crystalline and liquid crystalline to fluid disordered phase transitions at 301 K, 315 K and 328 K, respectively.

The reported phase transitions are consistent with previous reports in liquid [31]–[35]. Although promising, some drawbacks of the chitosan cushion arise due to its dynamics during evaporation. In particular, Retamal et al. have shown, in separate work, that vapor deposited chitosan exhibits on silicon surfaces a solid-state dewetting process, that occurs during the evaporation process on the substrate at room temperature [36].

In this work, we have focused on evaporating DPPC molecules directly onto a monocrystalline silicon substrate, covered with its native SiO_2 layer. The evaporation of molecules is performed in high vacuum conditions with *in-situ* ellipsometric thickness monitoring. After the evaporation process, the chamber is vented with air and heating ramps at a rate of 2 K / minute are performed. Using ellipsometry, we monitorized the optical thickness of the samples and observe the characteristic phase transitions of DPPC. In parallel, AFM is used to study the morphological changes of the sample after each heating ramp. Combined AFM and ellipsometric measurements show evidence of the formation of a phospholipid bilayer system which self-assembles in air, i.e. without applying liquid to the system. Using AFM we have performed force curves that show the rupture of several bilayers at increasing loads. Finally, we have observed the dynamical restructuring of the bilayer by increasing the AFM force setpoint of the imaging mode. The morphology, dynamics and rupture forces obtained corroborate with the ellipsometric measurements and point to a well formed DPPC bilayer in air. We cannot discard that this bilayer is formed via adsorption of a monolayer of water over the hydrophilic silicon surface after the sample is exposed to air. The relative humidity in the laboratory is approximately 20%.

1.2. Artificial Membrane

The term artificial membrane refers to a membrane formed synthetically in a laboratory for different purposes [1]–[3], [5], [6] using different techniques [27]–[29], [37]–[40]. The objective of the creation of an artificial membrane is to imitate the processes of biological membranes (nature).

A biological membrane is one of the essential components of cells found in all living beings. The biological membrane is formed by a series of lipids that act as a selective barrier surrounding the cell and cell organelles. These lipids self-assemble into bilayers to form phospholipid membranes composed principally of carbon and hydrogen with smaller amounts of oxygen, nitrogen, phosphorus, among others. In addition to phospholipids, other lipids are present in biological membranes, for example as glycolipids or cholesterol.

One of the main functions of the biological membrane is to maintain the chemical composition inside the cell (with limited volume); that is differences in the extracellular medium, generating differences in concentration between intra- and extracellular media. To maintain this different concentration, the selective passive diffusion and selective active transport allow in tandem the passage of molecules through the membrane due to the presence of different channels formed by different proteins. The proteins can be categorized into two, depending how they are membrane bound; first, peripheral proteins, that are slightly membrane bound through electrostatic interactions. Second, transmembrane proteins, that are inside the membrane passing through completely.

1.3. DPPC

The 1,2-dipalmitoyl-sn-glycero-3-phosphocholine DPPC is one of the most used lipids in the formation of artificial membranes. The DPPC is the principal component of pulmonary surfactant [41] and in its structure has a hydrophilic polar head and hydrophobic alkane double-chain. Its chemical formula is $C_{40}H_{80}NO_8P$ and its characteristic molecule length is 2.5 nm [31], [42].

To create phospholipid bilayers, there are different techniques as Langmuir-Blodgett [27]–[29], Dip-Coating [37], [38], Spin-Coating [39], [40], among others. In all of these techniques, the use of water is essential to produce the formation and the operation of the phospholipid membranes. Furthermore, water molecules join the membranes' hydrogen bonds in what is principally an electrostatic interaction (dipole-dipole) which forms the origin of the hydrophobic effects of the phospholipid molecules. In this work a new technique (process) was developed in Surface Laboratory (Surflab) in the Instituto de Fisica at Pontificia Universidad Catolica de Chile by our group [4], [43] and we demonstrate that the application of extra hydration after the evaporation process is not necessary for stable phospholipid bilayers formation on SiO_2/Si substrates.

The DPPC has a polar head with a nitrogenous group with positive charge and two identical hydrophobic chains composed by 16 carbons each. This phospholipids in presence of an adequate humid environment and atmospheric pressure, shows phase transitions in its structure (see figure 1.1), which are temperature dependent and are well known. These phases are: Crystalline (L_C), Gel ($L_{\beta'}$), Ripple ($P_{\beta'}$), Fluid (L_α) [32], [44] and Fluid Disordered [35]. The L_C phase is characterized by a rigid phase and the bilayer is in its base form when the lipids are totally vertical. The $L_{\beta'}$ phase, is characterized by a lipid chain inclination around 30° with respect the vertical axes or with respect the L_C

phase. The $P_{\beta'}$ phase is characterized by the increase of the chain disorder (or movement), that does not occur homogenously in the surface, and an undulated form is observed in the bilayer surface. The L_{α} phase is characterized by an augmentation of the membrane disorder, showing only a local ordering. The fluid disordered phase is characterized by any order in the membrane which can be observed, and the lipids are not in the bilayer structure formation. The phase transition temperature has been reported, in the case of L_C- $L_{\beta'}$ phase transition, the temperature when the transition occurs is between 293 K and 296 K, for $L_{\beta'}$- $P_{\beta'}$ phase transition the temperature range is 306 K to 310.5 K, for $P_{\beta'}$- L_{α} phase transition the temperature range is 314 K to 325 K and finally for L_{α}-fluid disordered phase transition occur between 326 K and 333 K [31], [32], [44]–[51]

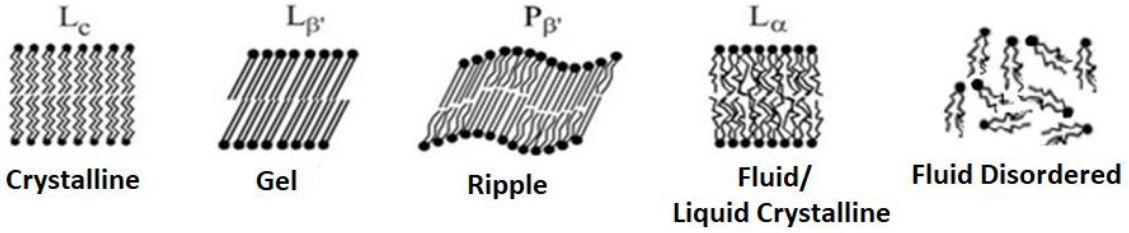

Figure 1.1: Scheme of the different phases of a phospholipid bilayer [52].

The Supported Lipid Bilayer (SLB) is the name of a planar structure sitting on top of a solid support. This structure has one side in contact with a free solution and the other side is in contact with a thin layer of water or other hydration liquid on the solid substrate. One of the advantages of this system, is its stability [53]. The approach of this thesis is totally different. It was possible to form and study stable SLBs which show similar characteristics as the widely studied "wet" SLBs. In other words, the dry SLBs show similar adsorbate-adsorbate and adsorbate-substrate interactions as physisorbed conventional SLBs [15]. The SLBs will not be destroyed even if a hole is made in the membrane. Moreover, the bilayer structure can be maintained for long periods of time, starting from several months up to a year.

2.Experimental Method

2.1. Very High Resolution Ellipsometry (VHRE)

Very High Resolution Ellipsometry is a non-invasive technique that permits us to measure optical properties of thin films. This technique has been proven to be an effective method to study wetting, growth and phase diagrams of organic multi films adsorbed on surfaces [54], [55]. VHRE is very sensitive to measure the thickness of a film and its resolution is 0.05 Å in average in an area equivalent of the laser spot illuminated on the sample.

The VHRE technique is based on the analysis of the polarization state of the reflected light from the adsorbed surface, which is given by:

$$\rho = \frac{\frac{E_{rp}}{E_{ip}}}{\frac{E_{rs}}{E_{is}}} = \frac{R_p}{R_s} \tag{2.1}$$

Where E_i and E_r correspond to the incident and reflected electric field respectively, R correspond to the intensities and the subscripts s and p correspond to the parallel and perpendicular polarization component of the light respectively.

The Fresnel coefficients for the reflected and transmitted wave are given by:

$$r_s = \frac{n_t \cos\theta_i - n_i \cos\theta_t}{n_i \cos\theta_t + n_t \cos\theta_i} \tag{2.2}$$

$$t_s = \frac{2n_i \cos\theta_i}{n_i \cos\theta_t + n_t \cos\theta_i} \tag{2.3}$$

$$r_p = \frac{n_i \cos\theta_i - n_t \cos\theta_t}{n_i \cos\theta_i + n_t \cos\theta_t} \tag{2.4}$$

$$t_p = \frac{2n_i \cos\theta_i}{n_i \cos\theta_i + n_t \cos\theta_t} \tag{2.5}$$

The reflected light has both transmitted and reflected components emerging from the interaction with the film. Hence, considering a total amplitude of the reflected waves as the addition of all amplitudes, we will obtain:

$$R = r_{01} + t_{01}t_{10}r_{12}e^{-2i\beta} + t_{01}t_{10}r_{10}r_{12}^2 e^{-4i\beta} + t_{01}t_{10}r_{10}^2 r_{12}^3 e^{-6i\beta} + \cdots \tag{2.6}$$

With,

$$\beta = 4\pi \frac{d}{\lambda} \sqrt{n_1^2 - n_0^2 \mathrm{sen}^2\theta_0}. \tag{2.7}$$

The formula 2.6 R then corresponds to a summation-geometric progression that can be reduced to:

$$R = r_{01} + \frac{t_{01} + t_{10}e^{-2i\beta}}{1 + r_{01}r_{12}e^{-2i\beta}} \tag{2.8}$$

$$R = \frac{r_{01} + r_{12}e^{-2i\beta}}{1 + r_{01}r_{12}e^{-2i\beta}} \tag{2.9}$$

Therefore:

$$R_p = \frac{r_{01p}+r_{12p}e^{-2i\beta}}{1+r_{01p}r_{12p}e^{-2i\beta}} \tag{2.10}$$

$$R_s = \frac{r_{01s}+r_{12s}e^{-2i\beta}}{1+r_{01s}r_{12s}e^{-2i\beta}} \tag{2.11}$$

Replacing equation 2.10 and 2.11 in the equation 2.1, we obtain:

$$\rho = \frac{(r_{01p}+r_{12p}e^{-2i\beta})(1+r_{01s}r_{12s}e^{-2i\beta})}{(1+r_{01p}r_{12p}e^{-2i\beta})(r_{01s}+r_{12s}e^{-2i\beta})} \tag{2.12}$$

Grouping terms and using the Fresnel coefficients, finally we obtain:

$$\rho = \tan\Psi\, e^{i\Delta} \tag{2.13}$$

The equation 2.13 in combination with equation (2.1) are known as ellipsometric general equation of Azzam y Bashara [56]. The ellipsometric angles Δ and Ψ are related with the experimentally measured angles as the follows:

$$\Psi = A \tag{2.14}$$

$$\Delta = 2P + \frac{\pi}{2} \tag{2.15}$$

Where A and P correspond to the analyzer and polarizer angles respectively. A and P are empirically measured in our ellipsometer, using a controller (Newport PMC200-P2) which produces a measurement accuracy of ±0.002 °. The VHRE setup can be observed schematically in figure 2.1. Due to β being related to the refractive index and the thickness of the film, we can write β in terms of the polarization angle as:

$$\beta = 4\pi\frac{d}{\lambda}\sqrt{n_1^2 - n_0^2 sen^2\theta_0} = 4\pi\frac{dn_1}{\lambda}cos\theta_1 = C\left(2P + \frac{\pi}{2}\right) \tag{2.16}$$

where C is a constant [57], [58].

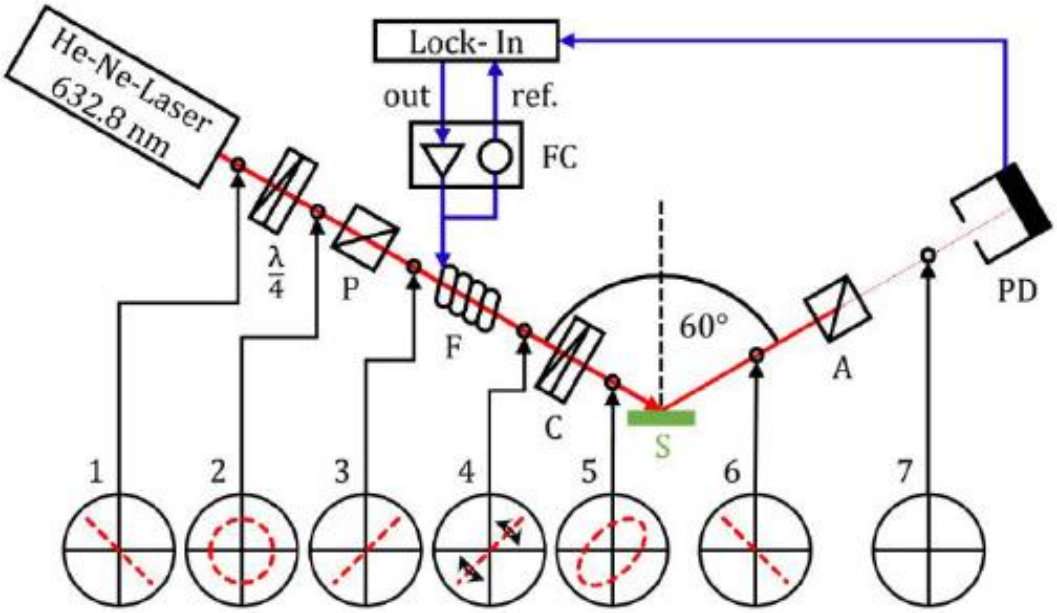

Figure 2.1: Scheme of the VHRE of surflab UC [59].

The VHRE setup is composed of a He-Ne laser with a characteristic (peak) wavelength of 632.8 nm, a quarter wave plate that permit us to change the polarization of the laser from linear to circular. A polarizer P was used to select conveniently the linear polarization plane. A fixed Soleil-Babinet compensator C [60] was used with the objective to stop the laser polarization from changing from linear to elliptical due to the beam front (i.e., the elliptical polarizability depends on the polarizer P). The ellipticity generated by a combination of the polarizer and compensator (P and C) should be the inverse of the ellipticity produced by the sample, then, the light reflected from the sample will have a linear polarization that could be nullified by the use of analyzer (A) that is physically identical to the polarizer. With this combination PCSA (Polarizer, Compensator, Sample and Analyzer) we can operate in null ellipsometry, which means, the intensity after the analyzer is null. The compensator was fixed in -45 ° [56], and the analyzer is fixed in some angle that is characteristic of each sample. For thin layers, i.e. below 500 Å, it is then necessary to change the polarizer angle to null the laser intensity after the analyzer: In the case of sample thicknesses above 500 Å, it is then necessary change both polarizer and analyzer to null the laser intensity.

The VHRE setup features a feedback system that compares the modulation signal of the intensity received by the photodetector with the reference signal obtained with a Lock-in amplifier or Phase Sensitive Detector (PSD), observed schematically in figure 2.1. The Lock-in amplifier has in the input an oscillated signal with a frequency of 756.2 Hz which is used to generate a small oscillation in the current of the Faraday glass coil (reference signal) in order to detect an oscillated signal (input signal) with the photodetector. The rectified signal of Lock-in amplifier is close to the 0 VCC. If some properties of the film change, a gap in the minimum of the light intensity occurs and the photodetector will measure a different signal, changing the output signal of the Lock-in amplifier, i.e. different of 0 V. When this different signal enters the Faraday controller, this will send a DC current to the Faraday coil/Faraday glass in order to rotate the

polarization plane of the incident light to the sample to get again a null intensity in the photodetector.

2.2. Atomic Force Microscopy (AFM)

Atomic Force Microscopy (AFM) is a technique which has revolutionized the topic of this thesis and the characterization of micro or nanostructured surfaces in general, due to its resolution vastly exceeding the resolution of the classical optical microscope. Surflab UC has the *NanoWizard 3* BioScience by JPK Company. AFM functions by scanning the surface of a sample with a probe or tip that in general has a curvature radius around 10 nm. The AFM tips are typically made with silicon (Si) and in some cases are coated with other materials to enhance certain properties such as; light reflectivity, conduction or to analyze magnetic samples, depending of the customer requirements. With this equipment, we measure the interatomic forces generated between the tip and sample surface during the scan process. These forces are Van der Waals type and result in a generation of a topography image of the sample surface [61].

The basic operation of AFM is as follows: an infrared laser is incident upon the tip which is coated with a reflective material whichreflects the laser toward a mirror then toward a four-quadrant detector. This detector permits one to observe small changes in the lasers' reflective position due to the AFM tip deflection from the surface. Using mechanic movements in the holder with piezoelectric system makes possible to return the laser to the initial position. This mechanism permits one to generate a topographical image of the sample surface. AFM can work in three different modes: contact mode, tapping® mode and non-contact mode.

In contact mode the tip scans the surface of the sample touching it all the time. This scan mode is used typically in hard samples as metals, minerals, among others. With this mode, soft samples as a biological samples could be destroyed or damaged

due to the constant contact with the AFM tip, resulting in unreal image of the sample topography.

Tapping® mode consists of the tip being in a constant oscillation with a frequency close to its resonance frequency during the surface is scanned. This oscillation is given by piezoelectric crystals placed in the cantilever holder, which vibrates in response to an alternating current. Tapping or Intermediate Contact Mode is more complex than the contact mode due to it requiring the use of a Lock-in amplifier or a PSD. The characteristic resonant frequency of each cantilever is given by the manufacturer and this value should be configured within the AFM. Intermediate Contact Mode is very useful for soft samples due to the contact being only at one point which avoids dragging the material with the tip. Another advantage of this mode is that it can be possible to obtain information about the different phases of the soft matter and the oscillation amplitude of the tip, both information are strongly related with the hardness of the scanned material and therefore is possible to distinguish material from different nature present in the sample.

In non-contact mode, the AFM tip never touches the sample surface, i.e. the distance between tip and surface remains constant. This mode is widely used in magnetic and electric measurements to create a topography image from attractions and repulsions between tip and sample [62].

The principal benefits of the AFM technique is that in general it is a non-invasive method if used in the adequate mode and the sample can be tested in air and/or liquid, for biological or soft organic matter, vacuums are avoided as the systems will lose water and therefore will be denaturalized. A disadvantage of AFM technique is the time necessary to form an image, which is higher compared with other techniques.

3. Materials and sample preparation

3.1. Substrate preparation

The substrate used was a monocrystalline silicon wafer (100) covered with its native oxide layer (15−25 Å), which was obtained from Virginia Semiconductor Inc. Substrates were cleaned in a mixture of H_2SO_4 (sulfuric acid at 95−97%) and H_2O_2 (hydrogen peroxide at 30%), both acquired from Merck. The mixture was formed in a 7:3 ratio and at 363 K the substrates were submerged in the mixture for 30 minutes (to clean the substrate using the "piranha" chemical bath) [63] [19]. The substrates were then rinsed twice and stored in ultrapure water (Merck). Before use, the substrates were dried applying a jet of ultrapure nitrogen gas (99.995% purity) purchased from Linde, Santiago, Chile. Cleaning efficiency was confirmed using Very High Resolution Ellipsometry (VHRE), able to detect even traces of organic contaminations. After the cleaning process, the substrate is functionalized hydrophilic to ensure that the polar heads of the DPPC phospholipid anchor on the substrate surface.

3.2. Physical Vapor Deposition with Ellipsometric Monitoring

Dry DPPC in powder form, purchased from Avanti Polar Lipids Inc., Alabaster, Alabama, USA, was placed inside of a Knudsen cell (see figure 3.1) itself inside of the high vacuum evaporation chamber (see figure 3.2). The DPPC (untreated/as purchased) was to be evaporated onto the cleaned silicon substrate as described as follows: The Knudsen cell is a thermal cavity of glass that is heated using a resistance. This cavity has a small hole in one of its ends with the objective to direct the material to be evaporated to the center of the substrate surface. The material distribution of the material deposited onto the substrate can be approximated by the following equation [64]:

$$z(x) = \frac{z_0}{\left(1+\left[\frac{x}{r}\right]^2\right)^2} \tag{3.2.1}$$

Where x is the distance between the substrate center and deposition point on the surface, r is the distance between the Knudsen cell hole and the substrate (in our vacuum chamber correspond to 40 mm approximately) and Z_0 is the value of the film thickness in the center of the sample (in our case this value is typically 60 Å). The film distribution on the bare silicon substrate is observed in figure 3.3. The vertical lines correspond to the edges of the substrate which are 10 x 10 mm^2. In the borders of our substrate, the film thickness is approximately 97% of film thickness in the center. The sample thickness was monitored *in situ* with VHRE to evaporate the required thickness of the film.

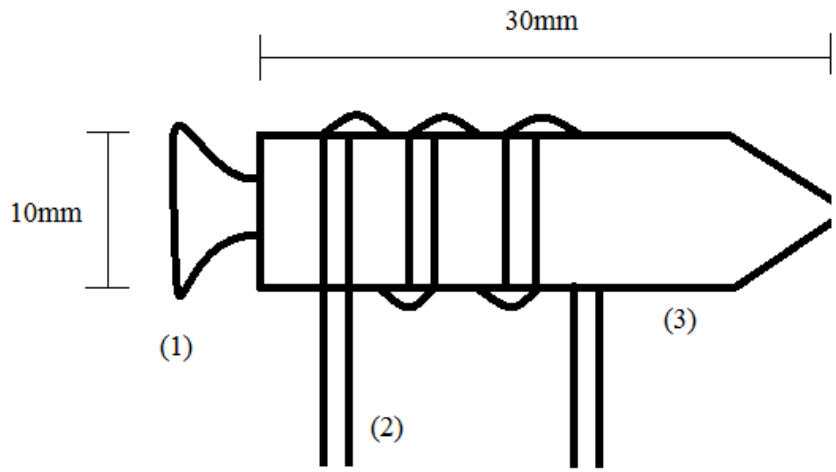

Figure 3.1: Scheme of the Knudsen cell. (1) Back cover, to seal the place where the material is placed. (2) Resistance (Thermocoax® coil compatible with ultra-high vacuum UHV) coiled wrapped glass. (3) Molded glass with a hole in its ends to direct the material to be evaporated.

The evaporation process was started in high vacuum ($\sim 10^{-6}$ Torr). During evaporation, when the temperature inside the Knudsen cell grows to approximately 443 K, the pressure in the chamber increases up to $\sim 10^{-4}$Torr. Substrate temperature was kept at room temperature ~296 K, and the deposition rates were approximately 3.2 x 10^{-2} Å/s. The optical thickness of each thin film was monitored *in situ* with VHRE during the phospholipid deposition process, comparing the variation of the absolute ellipsometric polarizer angle P of the sample with the initial polarizer angle P_0, corresponding to the bare substrate. The layer thickness was calculated using the Drude model [65] for single layers by relating the polarizer (P) and analyzer (A) angles to the ellipsometric parameters $\Delta = 2P + 90°$ and $\psi = A$. With these ellipsometric parameters one can obtain the value of the refractive index or the thickness of a film using the multiple reflections of the light variant upon the interaction with the medium-sample interface (i.e. vacuum/DPPC interface) and with the sample-substrate interface (i.e. DPPC/SiO_2 interface).

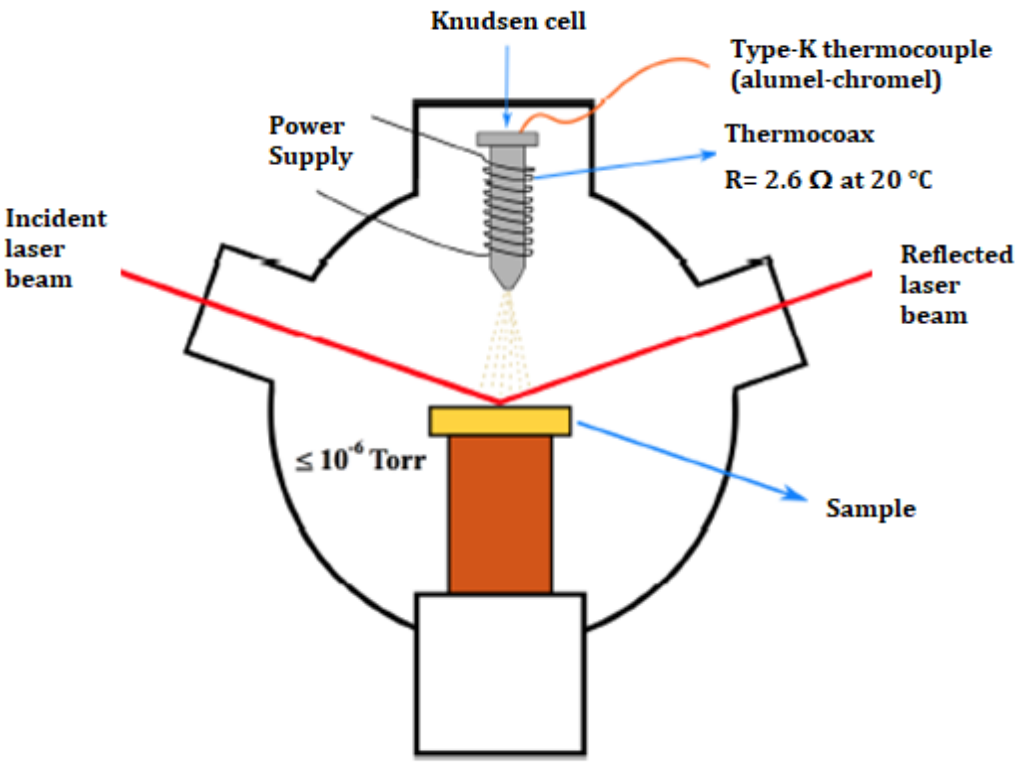

Figure 3.2: Evaporation Chamber [66].

The thickness of the films can be obtained using the Fresnel coefficients with the following equation:

$$\Delta P = \Gamma(\varepsilon_t, \varepsilon_n, \varepsilon_s)D \tag{3.2.2}$$

Where D corresponds to the thickness of the film. ε_t and ε_n are the dielectric constants tangential and normal of the film respectively and ε_s is the real dielectric constant of the substrate. The Γ expression is given by:

$$\Gamma(\varepsilon_t, \varepsilon_n, \varepsilon_s) = \frac{2\pi}{\lambda_0}\cos\varphi\left(\frac{1}{1-\varepsilon_s}\right)\frac{\varepsilon_t-\varepsilon_s-1+\frac{\varepsilon_s}{\varepsilon_n}}{\cot^2\varphi-\frac{1}{\varepsilon_s}}\frac{180}{\pi} \quad (3.2.3)$$

Where λ_0 is the laser wavelength and φ is the incidence angle with values of 6328 Å and 60.5 ° respectively. The other constants values are given in the table 3.1. When the light interacts with a surface, a percentage of this intensity is absorbed and propagates through the material. In this case, it is convenient use both real and complex part of the refractive index of the materials to compensate the losses due to the absorption process in the surface.

Parameter	Value
Incident angle	60.5 °
Laser wavelenght	6328 Å
Refractive index of the substrate [65]	3.877+0.019*i*
Dielectric constant of the sample	15.03+0.14*i*
Refractive index of the DPPC [38]	1.47
Dielectric constant of DPPC	2.1609

Table 3.1: Values of different constants used to determine the relationship between the thicknesses of the film with respect the changes in the polarizer angle (ΔP).

If we assume that $\varepsilon_t = \varepsilon_n = \varepsilon$, due to $D \ll \lambda_0$ and using the value from the table 3.1 [38], [65], the relationship between thickness of the film and ΔP of DPPC, for film thickness below 500 Å, is given by:

$$\Delta P = \frac{d}{18.5\ \text{Å}} \quad (3.2.4)$$

After deposition, the high vacuum chamber was vented with air at atmospheric pressure and the sample was analyzed as a function of sample temperature with VHRE and / or taken out of the chamber for further analysis with AFM. Temperature ramps from room temperature (RT) to 347 K were performed within the ellipsometer setup at a heating rate of 2 K / minute.

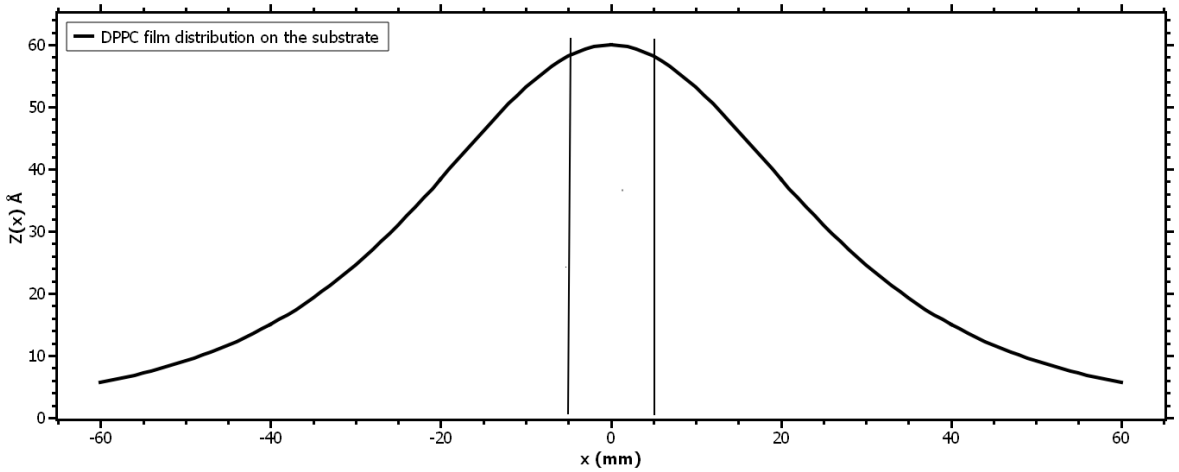

Figure 3.3: DPPC film distribution on the bare silicon substrate for deposition from our Knudsen cell.

3.3. AFM equipment

A *NanoWizard 3 AFM integrated apparatus* from JPK Instruments was used to obtain and process AFM data in to topographic information and the corresponding mechanical properties of the prepared films. AFM cantilevers purchased from Nano and More, Watsonville, CA, USA were used. The dimensions of our cantilevers were: thickness, 1 μm; length, 225 μm; and width, 48 μm. The resonant frequency was ~40 kHz, and the force constant was 0.6 – 1.5 N/m. To obtain the highest lateral resolution, images of 256 × 256 pixels were taken using QI^{TM} mode. The images were analyzed using Gwyddion and/or JPK Data Processing software. Force Mapping mode (also known as Force Volume) was used to collect an array of force curves containing mechanical properties of the samples, which can also lead to spatial reconstruction of topographic maps [67]. The JPK QI^{TM} mode was used to obtain topographical images and force curves. In addition, force curves were measured using Force Mapping mode in order to achieve a higher precision, due to an increased control of the parameters such as vertical speed and force.

4.Results

4.1 Design and construction of an electric system to measure ion conductivity across the membrane.

In a previous work, we made an electric system (see figure 4.1) to detect variations in the ion conductivity across the phospholipid membrane, with the aim to measure the changes in the capacitive response due to ion channel formation across the artificial membrane. Applying multiple square pulses at low power using a signal generator, we measured the ion current which reaches to the silicon wafer using an oscilloscope to compare different systems exposed to a liquid medium that simulated the natural cell membrane environment.

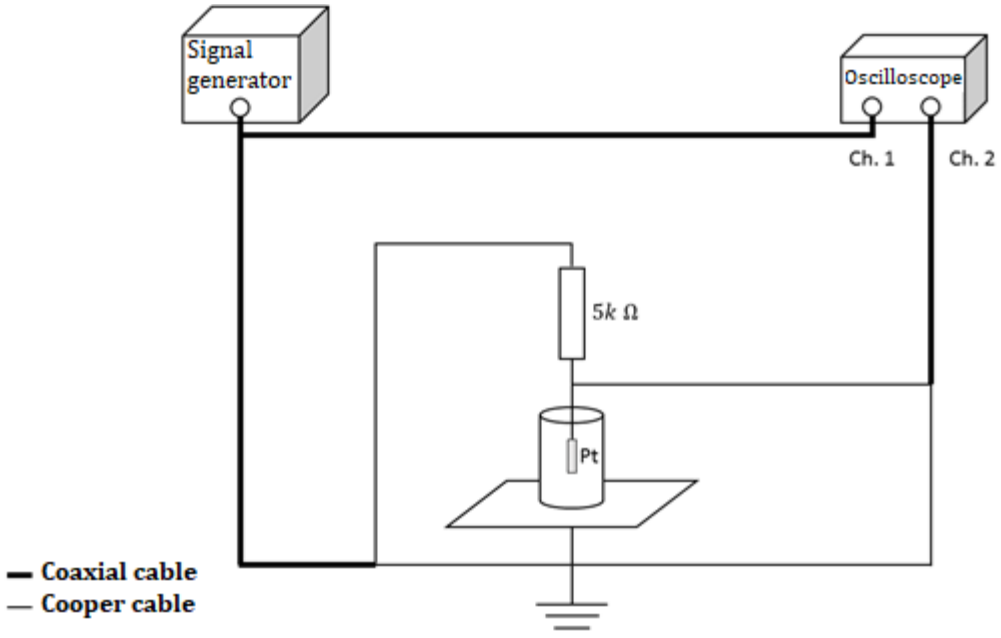

Figure 4.1: Scheme of a system to measure the capacitive response of an artificial membrane.

The results obtained using the system shown in figure 4.1 for different substrate coverages are observed in figure 4.3. These results show that the behavior of the varying systems stimulated by multiple square pulses is represented by a typical capacitive response (see figure 4.2) observed in the charge and discharge of a capacitor, i.e. we can study the system in a similar way as a capacitor, attributing the changes in the capacitance to changes in the system conductivity. The different systems studied were Si/SiO2/chitosan, Si/SiO2/chitosan/DPPC and Si/SiO2/chitosan/DPPC+Protein. It was possible to observe that the time response τ (or characteristic time of the capacitor), corresponding to half time of the charge and discharge of a capacitance, decreased when the proteins are inserted into the bilayer. The equation that represent the value of τ is given by:

$$\tau = RC \ln 2 \tag{4.1.1}$$

The change of the time response in the bilayer could be attributed to an increase in the bilayer conductivity due to the ion channel formations. These novel results were used within the application of a provisional patent (U.S. Provisional Patent Application (2014): "Nano-interface for molecular signal transduction" / "Nano-interfaz para la transduccion de senales moleculares". Inventor(s): U. G. Volkmann, T. Perez-Acle, S. Gutierrez, M. J. Retamal, and M. Cisternas. U.S. Provisional Patent Application Number: 62/037,027 (14 August 2014).) [68] and a definitive patent (Definitive Patent application (2015): “Interface ultradelgada y autohidratante que comprende un biopolímero hidratante y una bicapa lipídica." Inventor(s): U. G. Volkmann, T. Perez-Acle, S. Gutierrez, M. J. Retamal, and M. Cisternas. PCT application number: PCT/CL2015/050033 (August 13, 2015).).

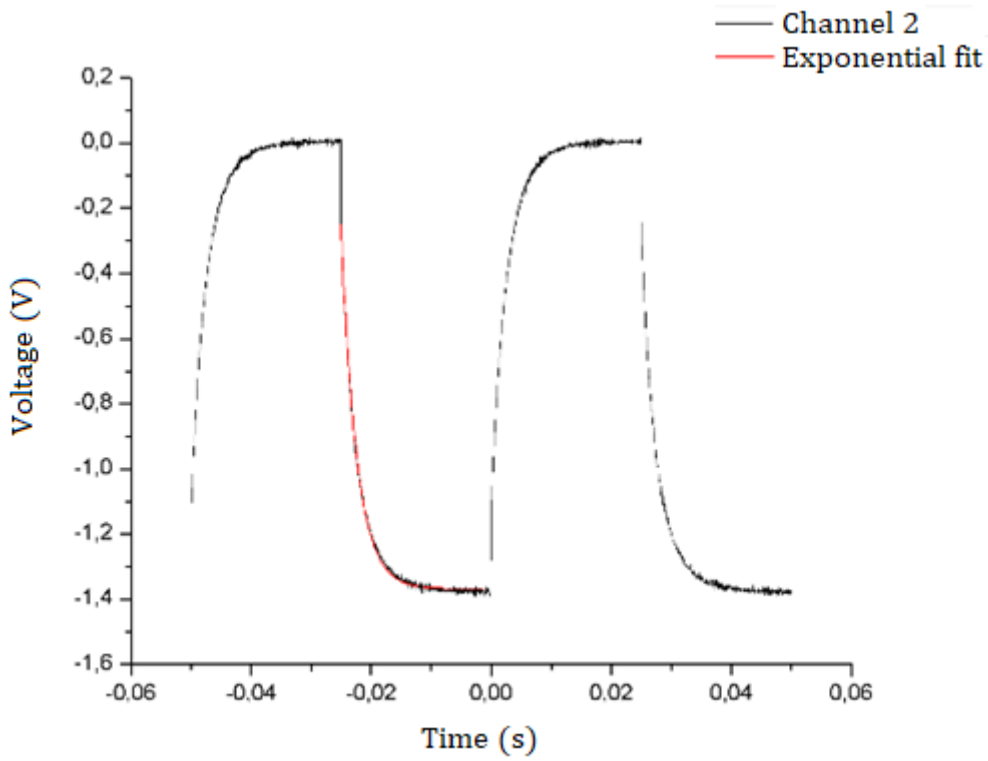

Figure 4.2: Data obtained of the capacitive response of the system.

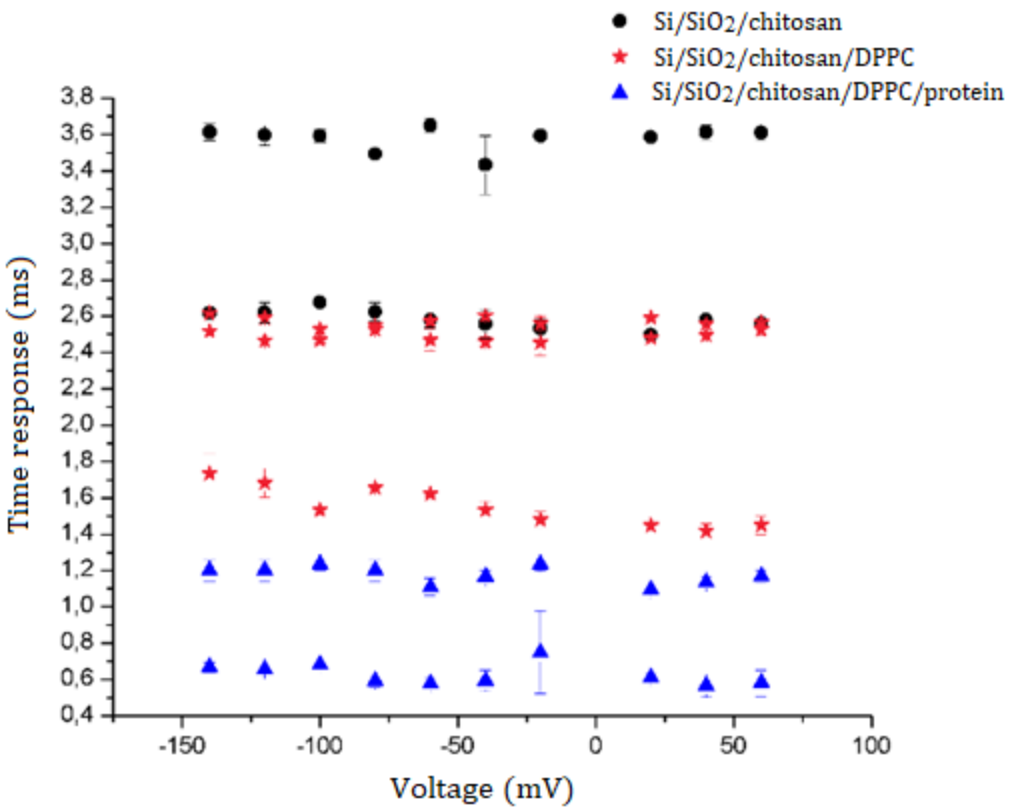

Figure 4.3: Characteristics time response of the different systems analyzed.

Using these preliminary results, a laboratory prototype was designed and constructed to perform the measurements more rigorously. This device (see figure 4.4) was constructed using a copper flat plate, as an electrode upon which the Silicon substrate was placed to collect the electric measurements. The silicon used was doped with boron to produce a high current conductivity in order to minimize the substrates' contribution to the capacitive measurements. The liquid container was made with Teflon to avoid all kinds of interactions of the container with the aqueous medium.

Figure 4.4: Laboratory prototype to measure the capacitive response of the system.

The results obtained using this prototype are shown in figures 4.5 to figure 4.7. First, we tried to observe the protein insertion whilst monitoring the characteristic response time of the system with respect of time before and after the protein were introduced to the aqueous medium. It was possible to observe that the characteristic response time measured with the prototype (see figure 4.5) was very similar in magnitude to the first system used (see figure 4.3 in blue data) for Silicon/chitosan/DPPC/protein. In figure 4.6 one can observe that the characteristic response times are dependent on the voltage frequency given by the power supply. These results were used to select the voltage range suitable for the measurements. The dependence on electrode distance was analyzed with the prototype (see figure 4.7). These results suggested that for further/future work, a new design for maintaining a controlled electrode distance would be desired.

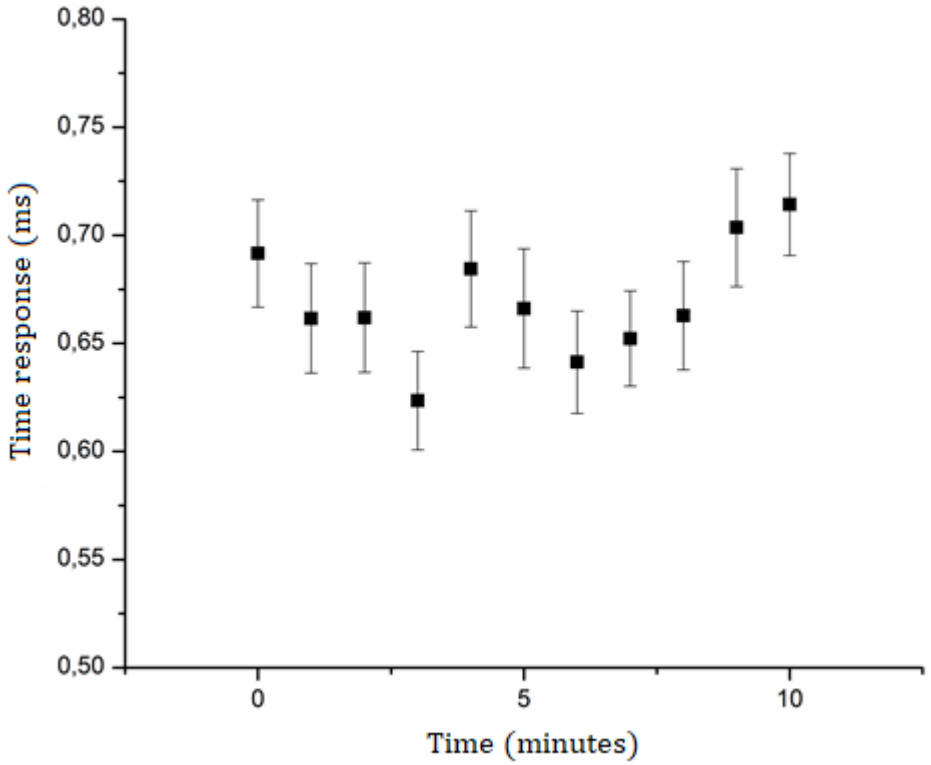

Figure 4.5: Study of the change of the characteristic response time with respect to time for the system SiO_2/chitosan/DPPC/protein.

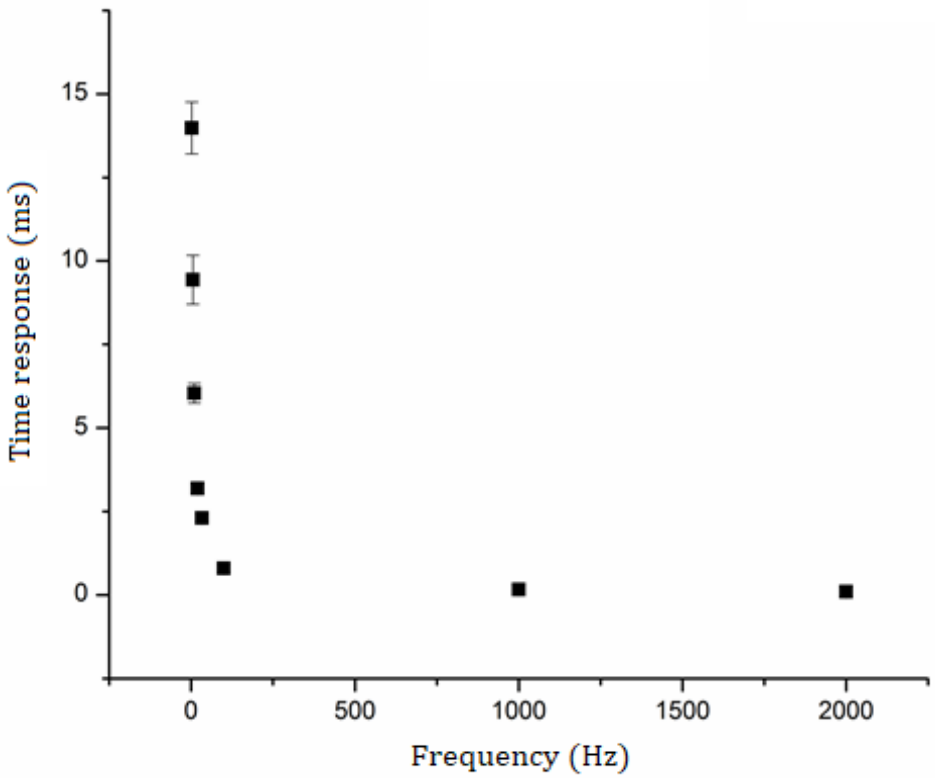

Figure 4.6: Study of the change of the characteristic response time with respect to frequency of the external voltage applied for the system SiO_2/chitosan.

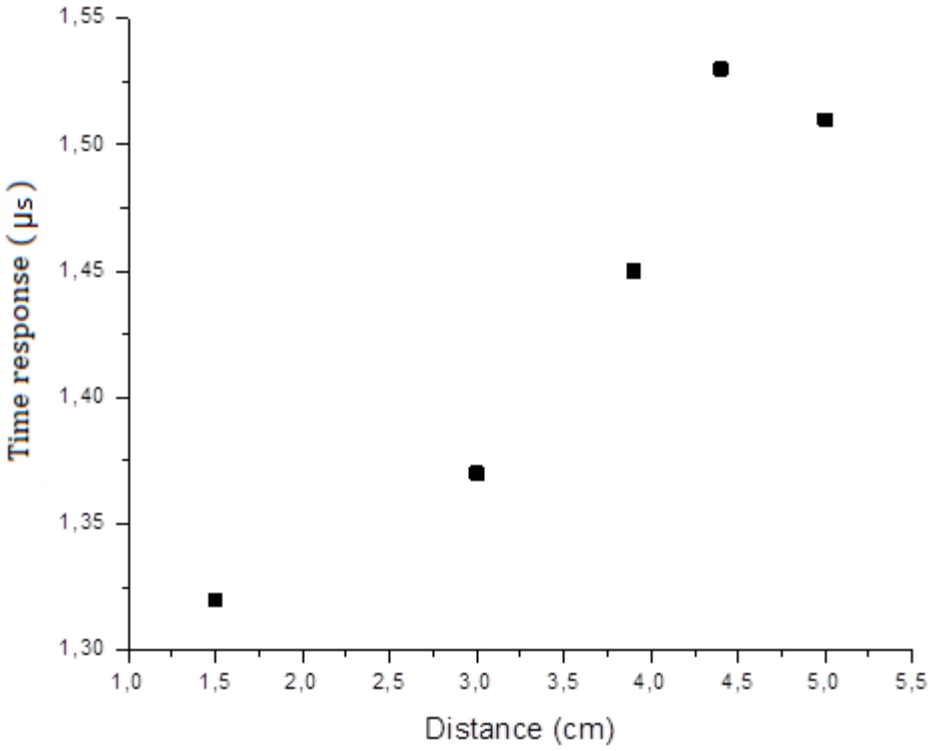

Figure 4.7: Study of the change in the characteristic response time with respect the electrode distance for the system SiO_2/chitosan.

4.2 Design of a new ellipsometer in vertical configuration.

The new results generated new concerns about the phospholipid bilayer formation after the evaporation process in air and aqueous medium. It will be necessary to understand how the electric pulses and the bilayer thickness is altering the bilayer behavior itself. To answer these concerns, it was deemed necessary to construct a new Ellipsometer in a vertical configuration (see figure 4.8 and figure 4.9) to perform measurements in aqueous medium to be contrasted with measurements in air.

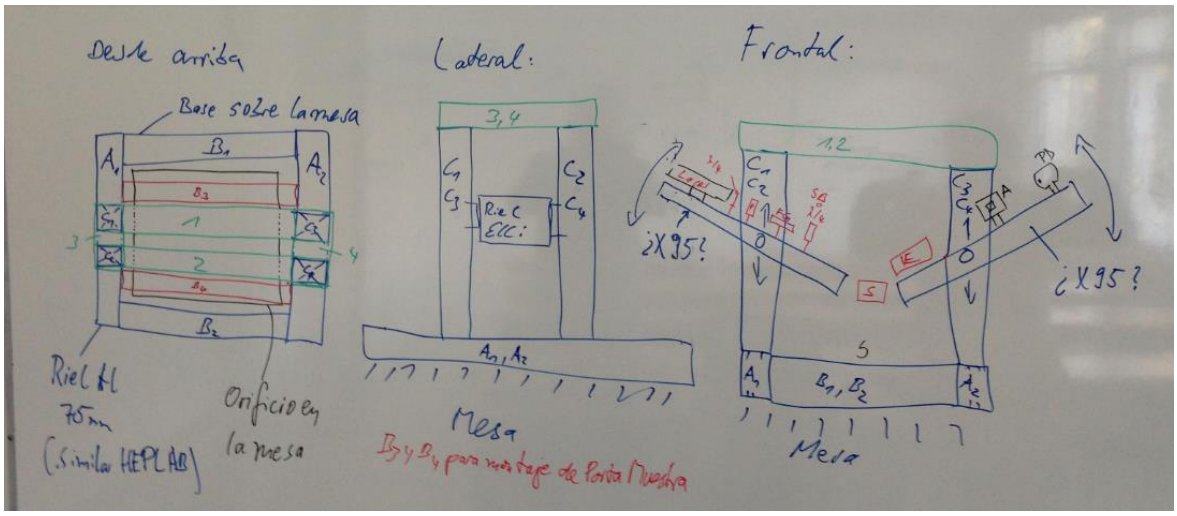

Figure 4.8: Draft of the Ellipsometer for construction in Surflab.

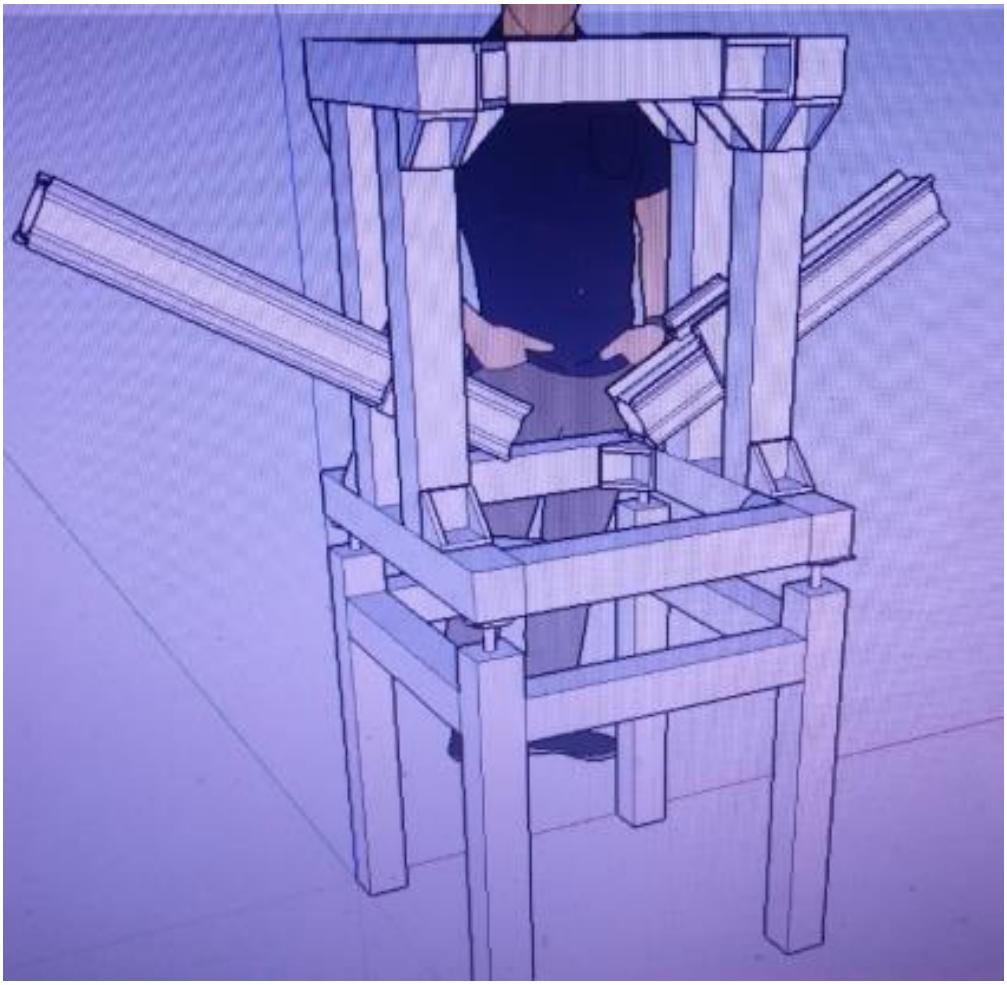

Figure 4.9: *3D scheme of the ellipsometer for construction in Surflab* [59].

4.3 Design of an accessory to measure phase transitions of SLB in aqueous medium for the ellipsometer present in the laboratory

Alongside the design and construction phase of the new ellipsometer, an accessory for the ellipsometer already present in the laboratory was also designed and constructed (see figure 4.10 and figure 4.11 respectively). The accessory was intended for the measurement of temperature ramps in aqueous media in a horizontal configuration. The material used to construct this accessory was Teflon to avoid all kind of interaction between the cell and the aqueous medium.

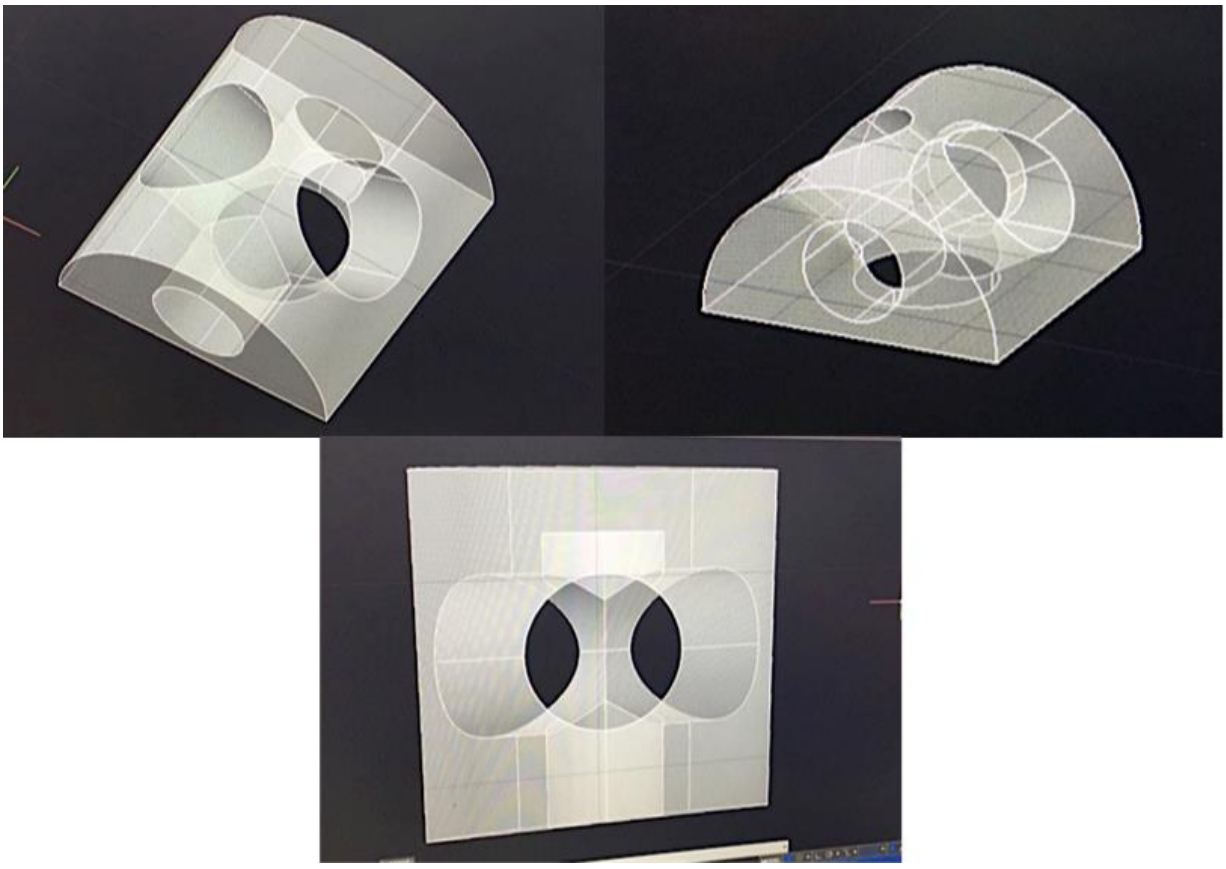

Figure 4.10: Alternate views of the 3D scheme of the accessory designed to measure temperature ramps of supported lipid bilayer in aqueous medium, in horizontal formation, in the ellipsometer present in the laboratory.

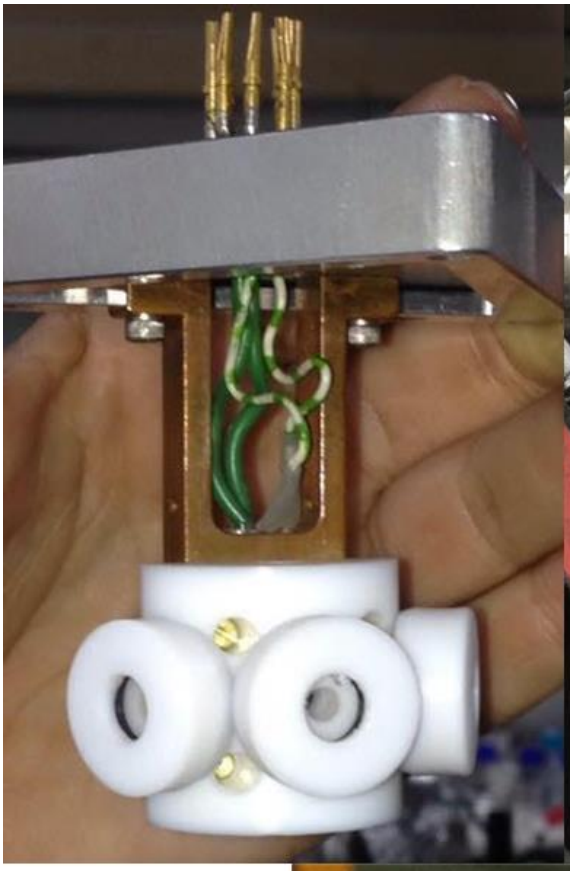

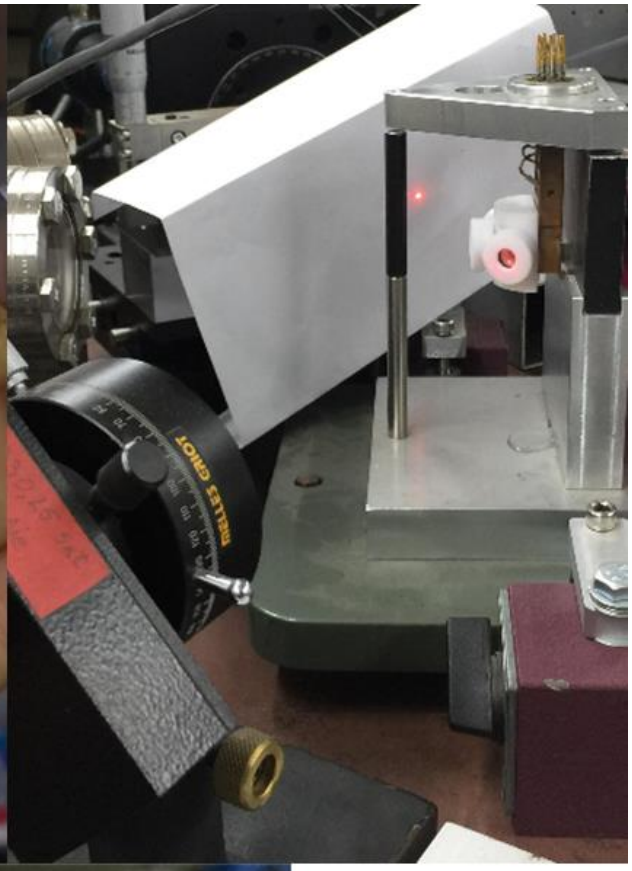

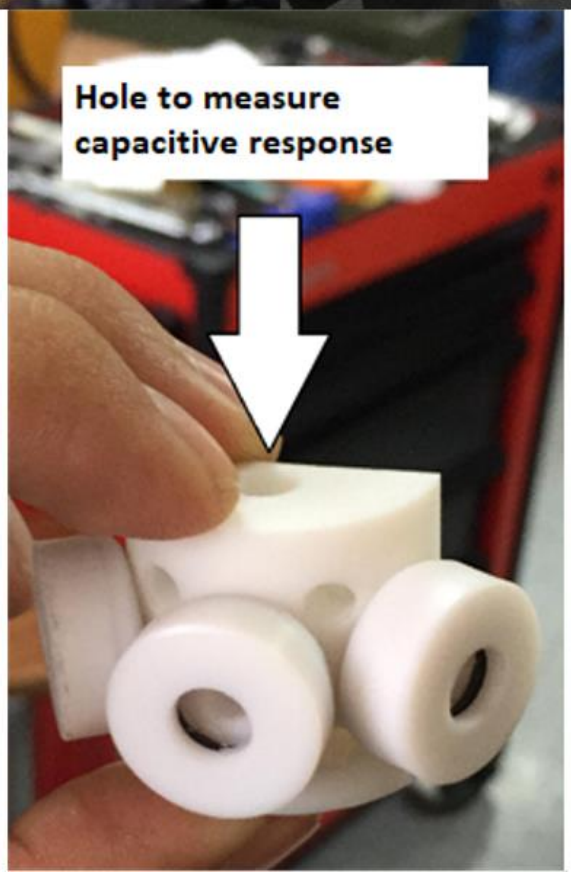
Hole to measure
capacitive response

Figure 4.11: *Constructed accessory for the measurement of temperature ramps in phospholipid bilayers immersed in aqueous media in the ellipsometer present in the laboratory.*

Using the new accessory, it was possible to measure the temperature ramps of the phospholipid bilayers and any corresponding phase transitions of the layers. These results are shown in figure 4.12. Using figure 4.12 it was possible to obtain the temperature of the characteristic phase transitions of the DPPC bilayers. There was variation between curves measured in air and in aqueous media due to bubble formations inside the cell. For the same reason it was not possible to measure the cooling part of the temperature cycle because the laser geometry was misaligned due to the bubble formations.

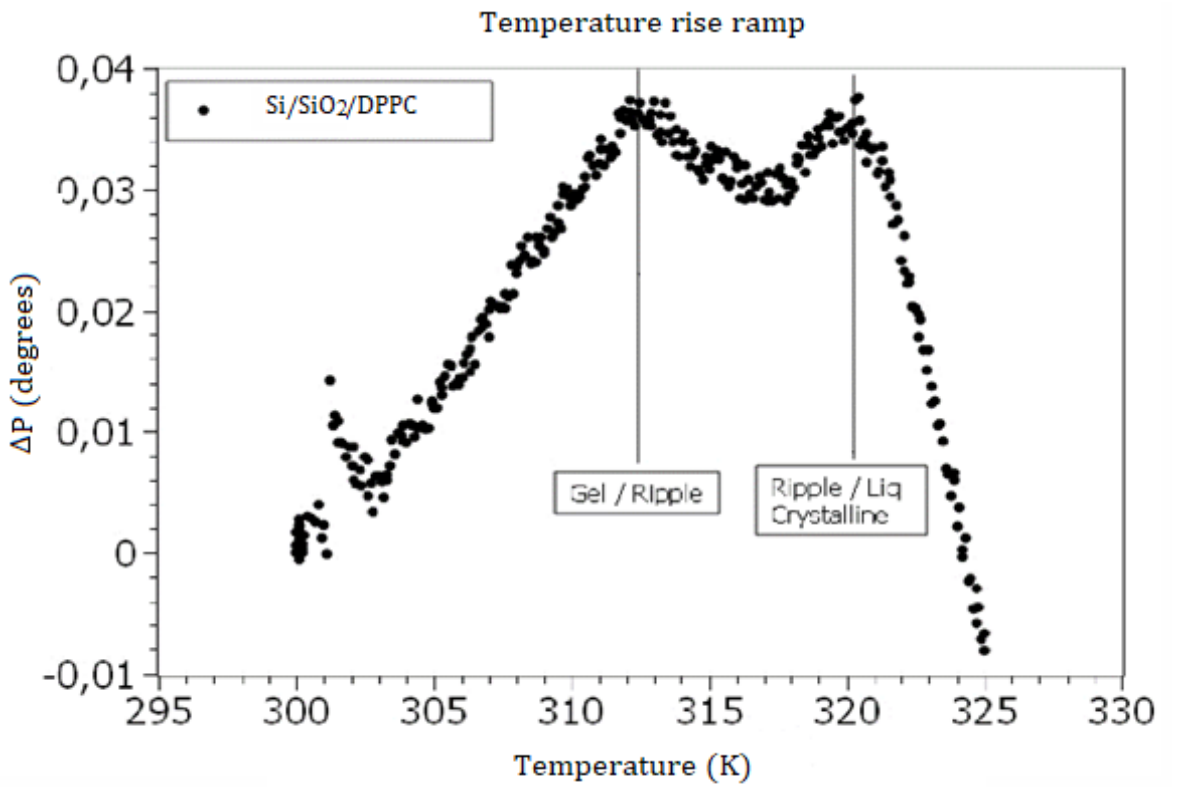

Figure 4.12: Ellipsometric signal measured during the temperature ramp performed on a phospholipid bilayer in water. In this graph, it is possible to observe phase transitions in the phospholipid bilayer characterized by the curves' inflection points.

The principal disadvantage of this new accessory was that during the temperature ramps, air bubbles were formed inside the accessory windows. To avoid the air bubble formations, we will measure temperature ramps in aqueous medium inside a glass cell designed for the new ellipsometer in a vertical configuration.

4.4 Phase transitions measurements of SLB in air

In parallel to the construction of the new ellipsometer, a study of the behavior of the evaporated phospholipids over silicon substrates in air medium was performed. The idea behind the study was to investigate the behavior of the evaporated films without further hydration, during multiple temperature cycles with the specific aim to understand how the molecules are organized on the silicon substrate. The experimental objective was to observe collective phenomena in the DPPC molecules with respect to different evaporated film thicknesses starting from 10 Å to 100 Å. The results showed an interesting collective phenomena. In the first ramp, it was possible to observe an unstable behavior, attributed to a reorganization process during the temperature ramp. From the second to fifth temperature ramps it was possible to observe a new stable behavior that was reproducible with respect to time. We will start analyzing the temperature dependence of the ellipsometry signal for samples with thicknesses below 30 Å (see figure 4.13 to figure 4.15).

For the 10 Å DPPC evaporated sample (see figure 4.13) it was only possible to observe changes in the Ellipsometric measurements in the first ramp. These changes confirmed the topographical changes of the system. After that, the system displayed stable behavior. It is important to note that in the first ramp, ΔP is around 0.2 degrees while in the following ramps this change was around 0.02 degrees – corresponding to instances when it was not possible to observe collective phenomena. A similar behavior was observed in the 10 Å sample shown in figure 4.14. In this sample, it was only possible to observe changes in the Ellipsometric measurements in the first ramp and after that the system passed to a stable behavior, similar to the 30 Å sample. It is important to note that in the first ramp, ΔP was around 0.4 degrees while in the following ramps this change was around 0.04 degrees when it is not possible to observe collective phenomena again, e.g. as observed for the rotator phase in alkanes [65]. The behavior of the third sample shown in figure 4.15 was similar to the other two samples. It was

possible to observe changes in the Ellipsometric measurements only in the first ramp and in the following measurements it was not possible to observe collective phenomena.

10 Å of DPPC evaporated over silicon substrate:

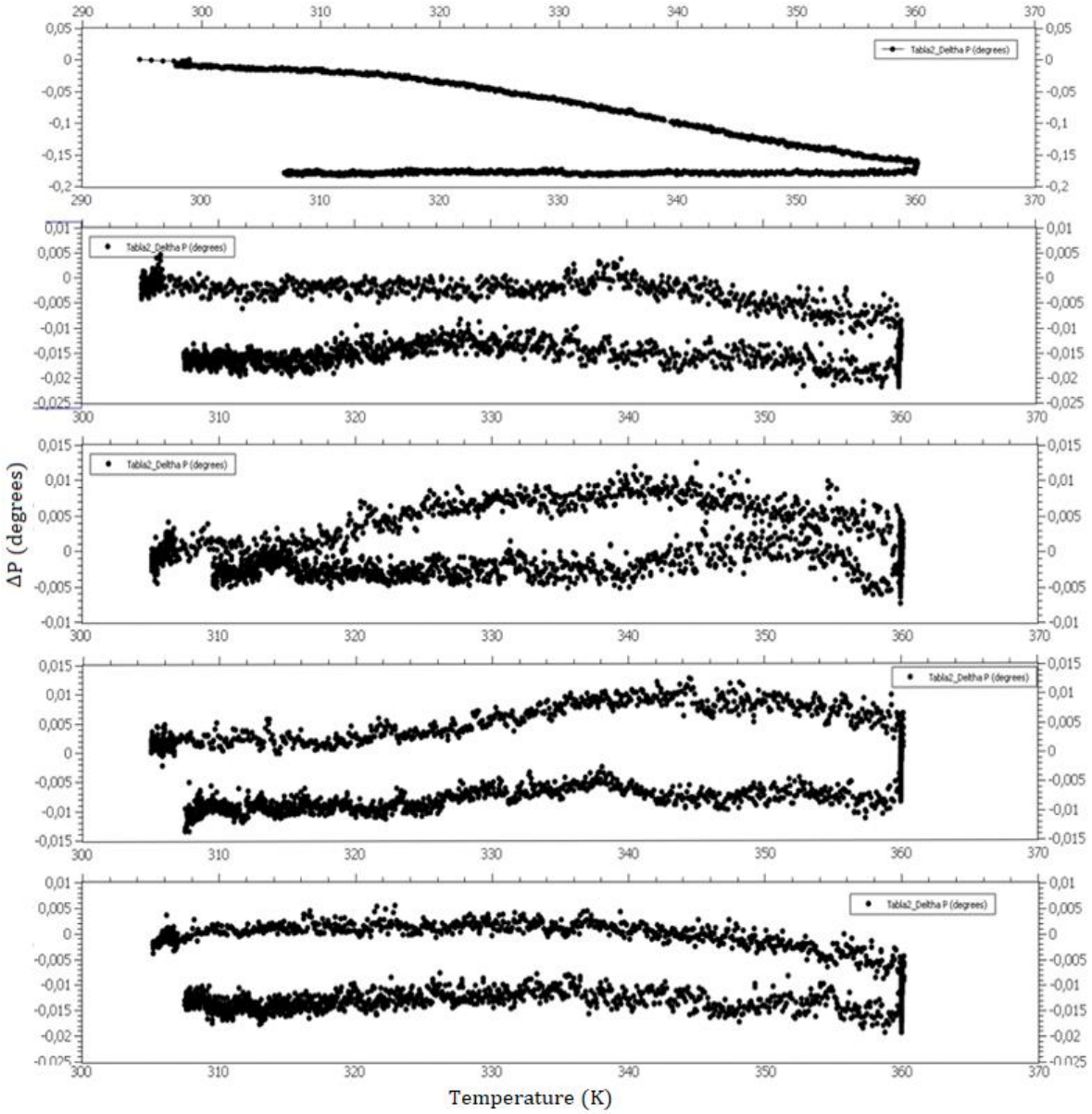

Figure 4.13. ΔP vs temperature ellipsometric measurement of 10 Å thick *of evaporated DPPC film. The graphs shown from top to bottom are the first to the fifth temperature ramp, resp.*

15 Å of DPPC evaporated over silicon substrate:

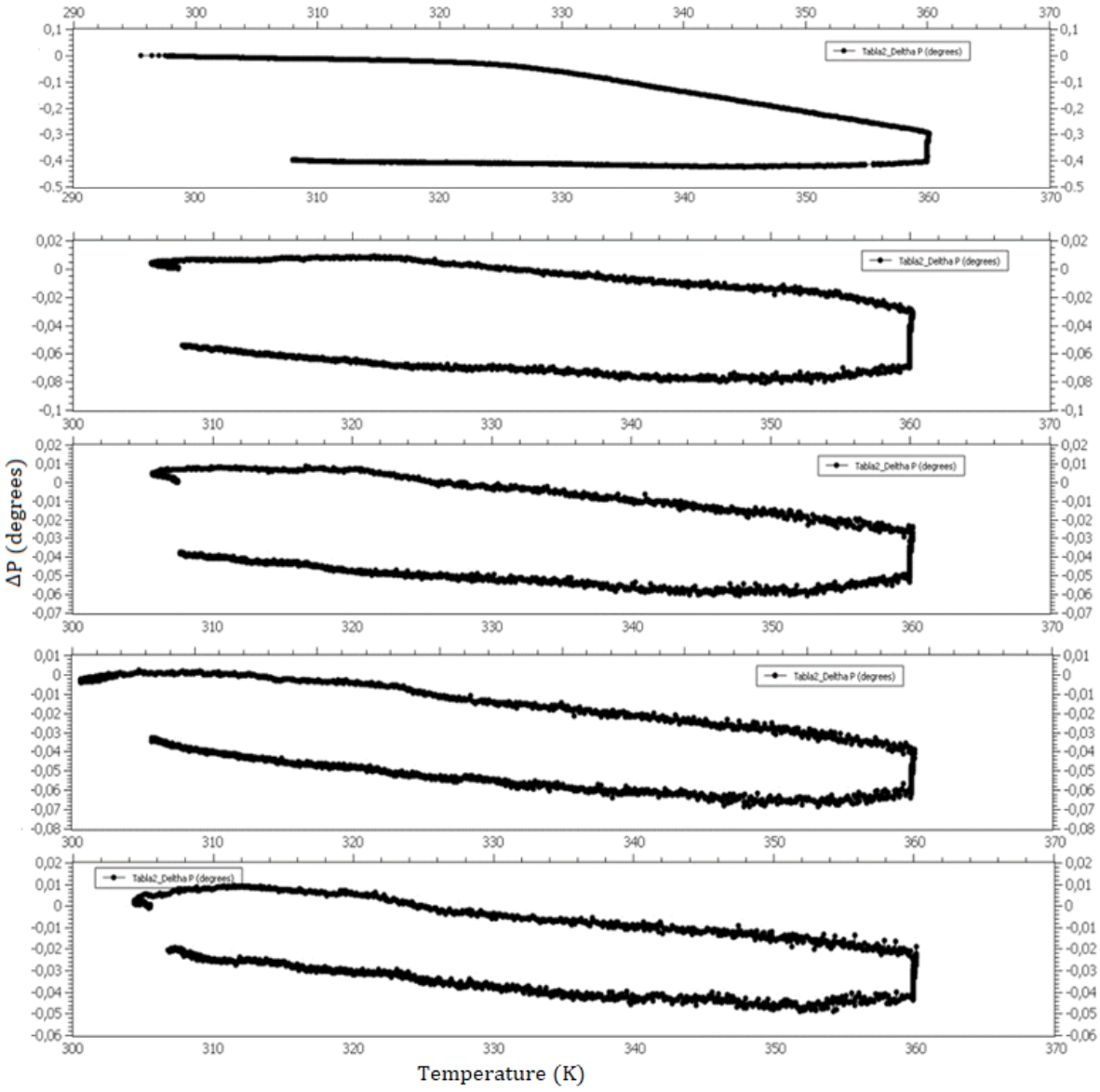

Figure 4.14: ΔP vs temperature ellipsometric measurement of 15 Å thick *of evaporated DPPC film. The graphs shown from top to bottom are the first to the fifth temperature ramp, resp.*

25 Å of DPPC evaporated over silicon substrate:

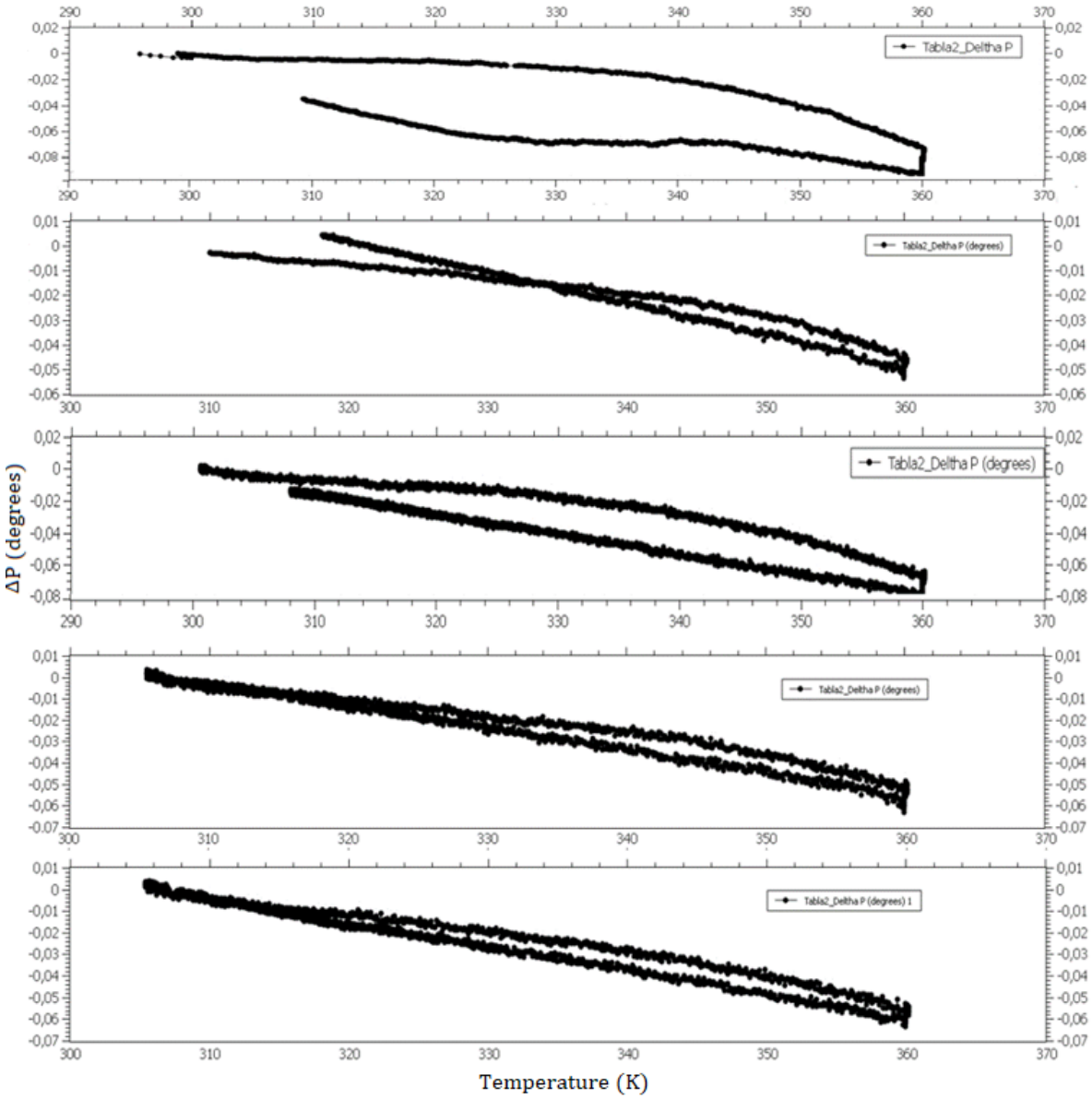

Figure 4.15: ΔP vs temperature ellipsometric measurement of 25 Å thick *of evaporated DPPC film. The graphs shown from top to bottom are the first to the fifth temperature ramp, resp.*

The results obtained from samples with thicknesses above 40 Å displayed very different behavior to the previous thinner films. These results can be observed in figure 4.16 and figure 4.17. In the case of figure 4.16, the thickness of the sample was around 40 Å and this sample showed collective phenomenon. It was possible to observe equally for the other samples, changes in in response to the first ramps that were attributed to morphological changes on the surface. These changes were due to the kinetic energy gained by the molecules during the temperature ramp, reaching stable behavior for the following temperature ramps. The changes in the slope of the curve for the second and the following temperature cycles were attributed to the phase transitions in the bilayer, because these changes occur close to the phase transition temperature reported in the literature, obtained in liquid (water or solvent). However, in this case the bilayer was immersed in a dry medium (air). This finding suggested that it was possible that the bilayer was formed in the absence of water. To answer this question, one should perform similar measurements in a nitrogen atmosphere to observe if the phase transitions are present there also. If the phase transition disappears, then the bilayer could be formed with the air humidity, without need of further hydration.

40 Å of DPPC evaporated over silicon substrate:

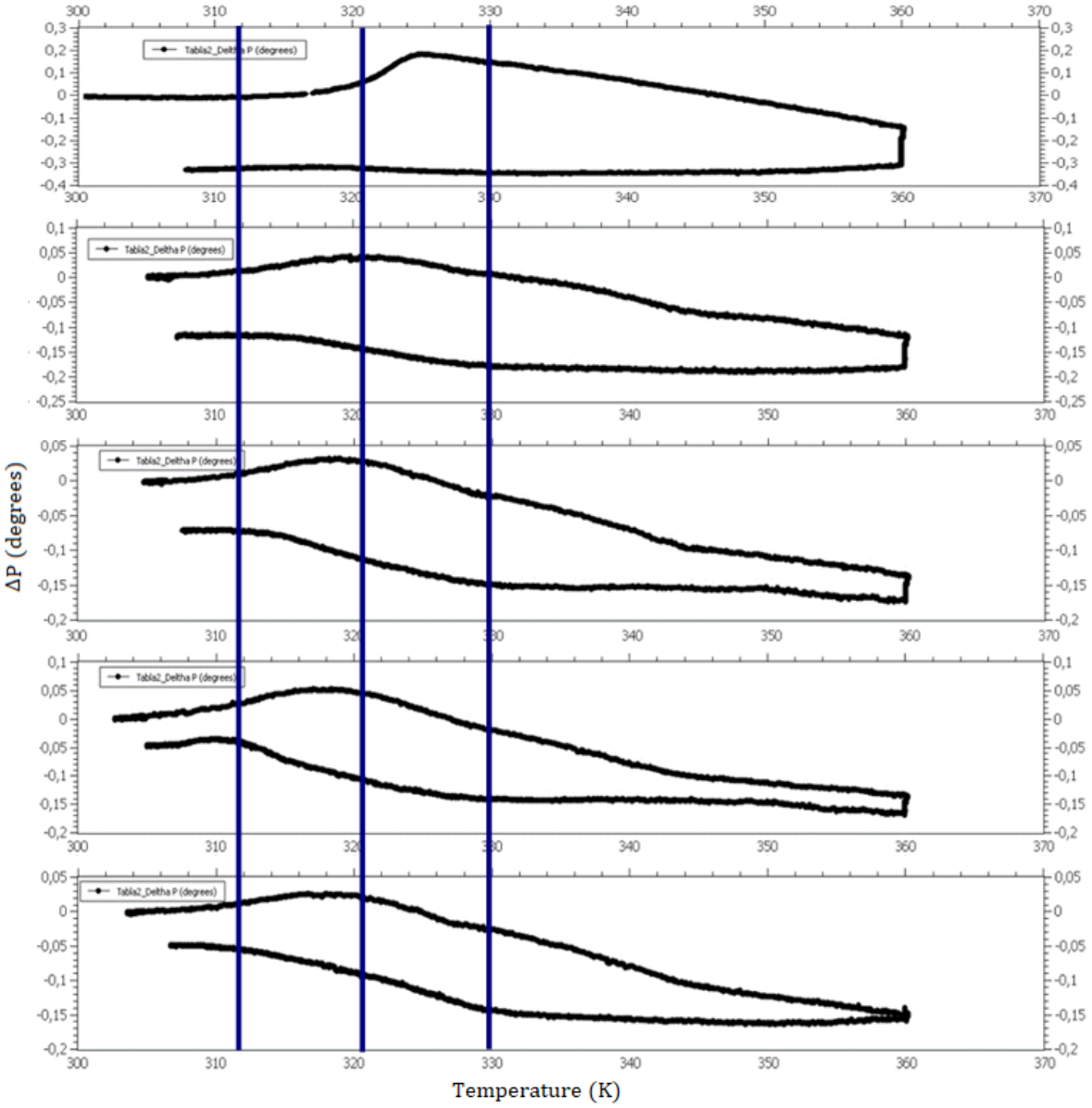

Figure 4.16: ΔP vs temperature ellipsometric measurement of 40 Å thick *of evaporated DPPC film. The graphs shown from top to bottom are the first to the fifth temperature ramp, resp.*

In figure 4.17, the thickness of the sample was 100 Å and collective phenomena was observed also. It was possible to observe the same behavior as the other sample in the first ramp that can be attributed to morphological changes due to the kinetic energy gained by the molecules during the temperature ramp followed by stable behavior for the following temperature ramps. The changes in the slope of the curve were attributed to phase transitions in the bilayer because for the same reason described for figure 4.16, these changes occur close to the phase transition temperature reported in the literature and with similar critical values obtained herein for the sample with a thickness of 40 Å.

100 Å of DPPC evaporated over silicon substrate:

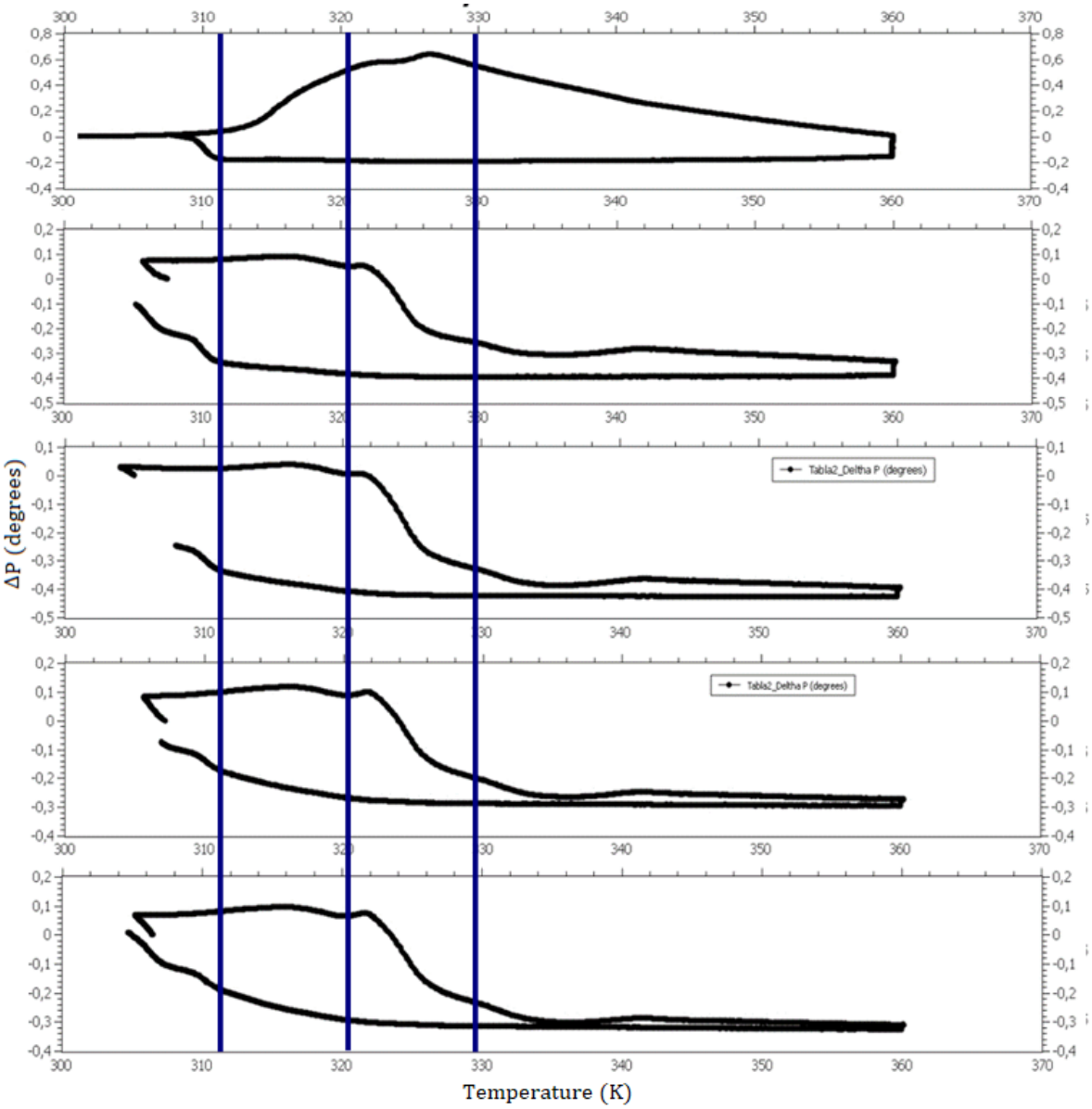

Figure 4.17: ΔP vs temperature ellipsometric measurement of 100 Å thick *of evaporated DPPC film. The graphs shown from top to bottom are the first to the fifth temperature ramp, resp.*

4.5 Measurements of the topography effects due to the temperature cycles applied to SLBs in air and in water using AFM

To quantify the topographical changes in the sample surfaces due to the thermal cycles applied, AFM images were performed before, during and after the temperature ramps, in air and in water media (see figure 4.18). It was possible to observe in figure 4.18 a) and b) that the sample topography changed after the temperature ramps – occurring during the thermal cycle realized in the AFM. This result confirmed that the measurement obtained using the ellipsometric curves that of ΔP, show us that the morphological changes occurred during the first temperature ramp. This behavior was observed in air and in water media and suggested that the temperature cycle affects dramatically the topography of the sample. These changes are related to a new stable morphology of the material on the silicon substrate.

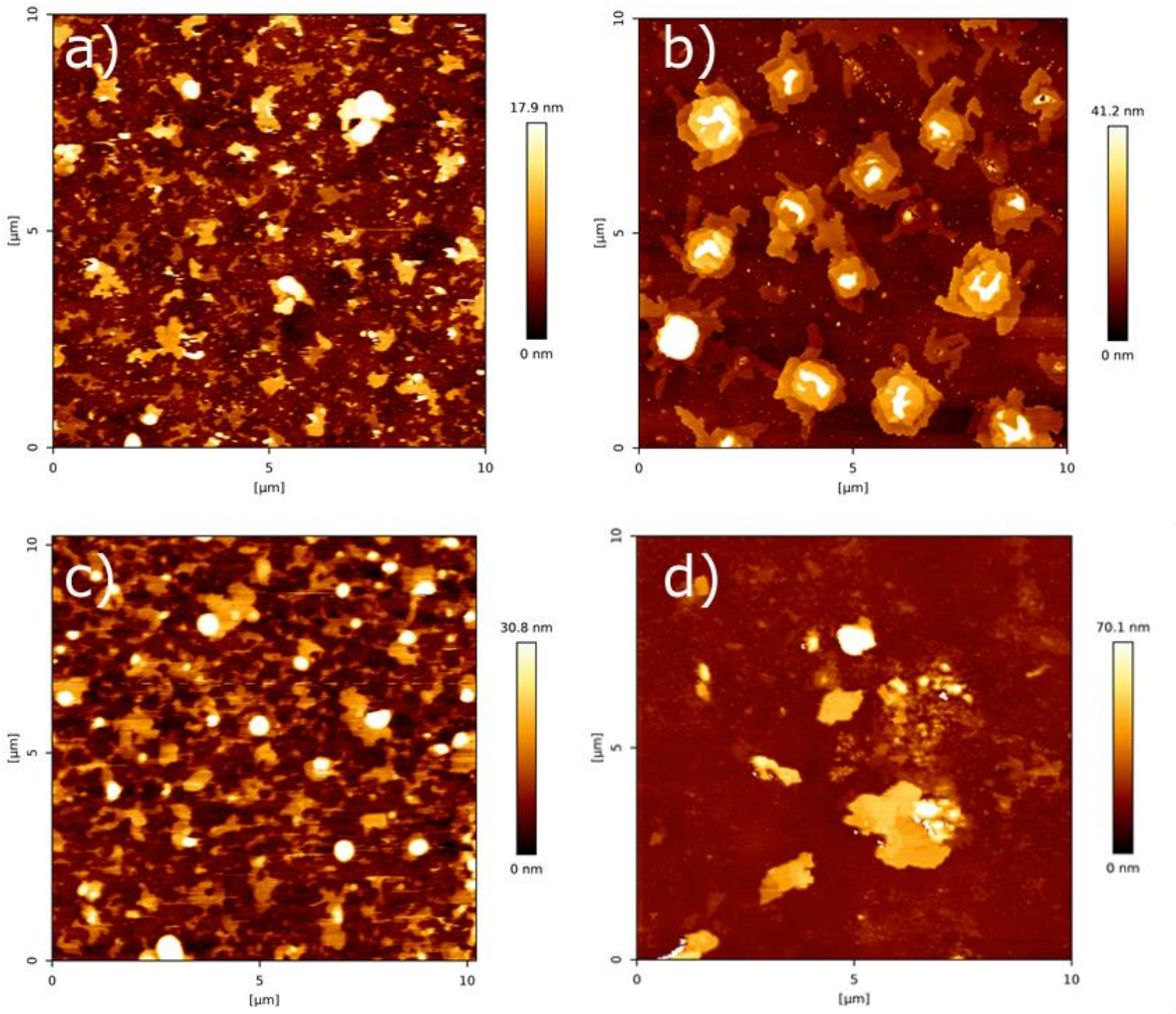

Figure 4.18: 10 µm x 10 µm AFM topographical images taken at room temperature of the sample before a) and c) and after b) and d) the temperature ramps in air a) and b) and in water c) and d), from room temperature to 360 K.

4.6 Determination of the appropriate thickness of the DPPC evaporated to form a homogeneous film on the silicon substrate

To decide the specific thicknesses to be used to insert the protein in the Supported Lipid Bilayer (SLB) created in a dry process, the topography of samples with different thicknesses where observe using AFM. The criteria used to determine the suitable thickness is the major coverage percentage. The images of the samples with thicknesses in between 20 Å to 100 Å are shown in figure 4.19. For samples with thicknesses above 60 Å we found complete coverage of evaporated material and concluded that this thickness (60 Å) is optimal to form artificial membranes.

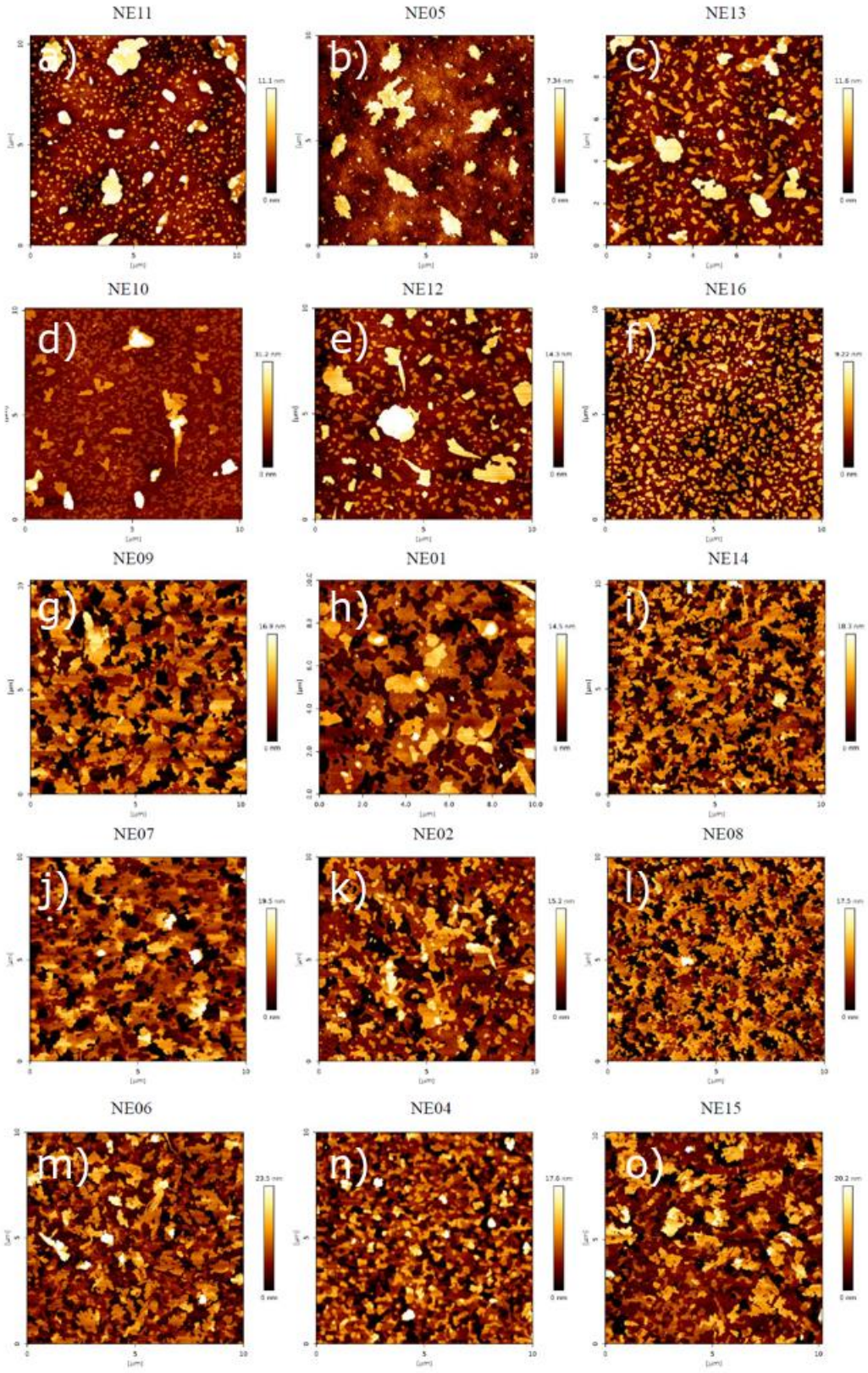
NE11
a)
NE05
b)
NE13
c)
NE10
d)
NE12
e)
NE16
f)
NE09
g)
NE01
h)
NE14
i)
NE07
j)
NE02
k)
NE08
l)
NE06
m)
NE04
n)
NE15
o)

Figure 4.19: Topographic images 10 µm x10 µm obtained using AFM for samples with thickness of: 20 Å *figures a), b) and c). 40* Å *figures d), e) and f). 60* Å *figures g), h) and i). 80* Å *figures j), k) and l). 100* Å *figures m), n) and o)* [69].

4.7 Supported Lipid Bilayer formation

In Figure 4.20 we show an AFM image of DPPC as deposited over silicon and force spectroscopy curves obtained on the different evaporated regions using quantitative imaging (QI^{TM}) mode. Figure 4.20 a) shows the island-like topography of the sample right after the evaporation process. Figure 4.20 b) shows a height distribution of the topography, from where we can identify three clearly separated height levels. From these height distributions we obtain the three main peaks centred at 4.01 ± 0.93 nm (level 1), 8.08 ± 0.94 nm (level 2) and 12.17 ± 0.98 nm (level 3). These step heights are multiples of 4 nm, which is the characteristic height of a DPPC bilayers [31], [70]. Figure 4.20 c) shows an adhesion map of the same region, while Figure 4.20 d) shows an adhesion distribution. From Figure 4.20 d), we can say that the entire surface is covered with a layer that has roughly the same adhesion, i.e., only one peak is seen centred at 9 nN, this is higher than our measured value for the bare silicon substrate, on which we measure an adhesion force of 5 nN (Figure 6.13).

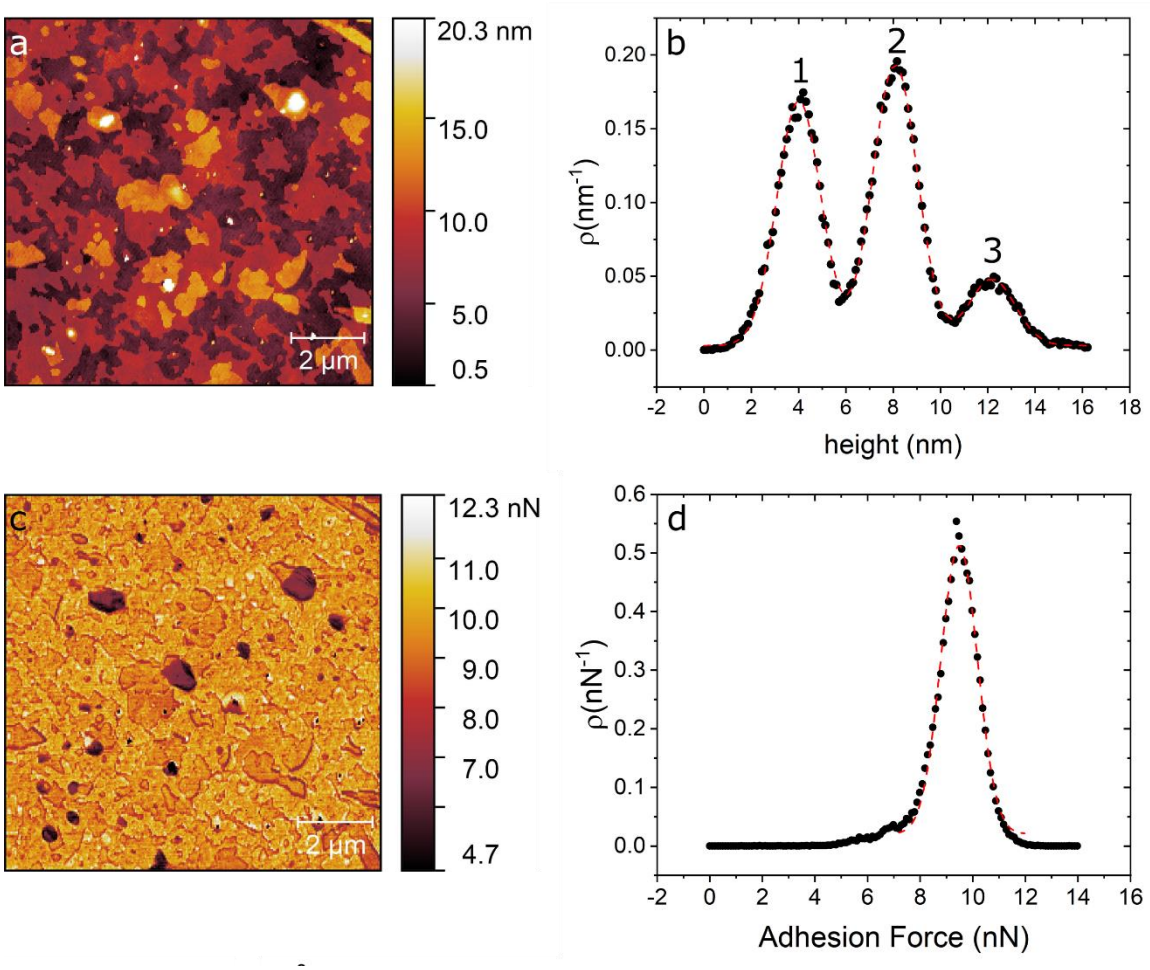

Figure 4.20. a) AFM topography image of DPPC/SiO_2/Si taken directly after evaporation. b) Height distribution of the topography map showing the three distinct levels at 4 nm, 8 nm and 12 nm. c) Adhesion map of the same region. (d) Adhesion distribution centered at 9 nN [71].

In order to test the mechanical properties of the membrane in Figure 4.20, we performed force curves using AFM [72]. Figure 4.21 shows the representative AFM force curves taken using force mapping mode on a 7 µm × 7 µm area. Breakthrough events are seen as sudden drops in the force curves. These breakthrough events are seen at all points, and show 1, 2 or 3 breakthrough events (Figure 4.21 a)–c)), respectively. Force curves with one breakthrough are attributed to the rupture of the first level, i.e., only one bilayer (Figure 4.21 a)). Meanwhile, force curves with two and three

breakthrough events are related to ruptures in levels 2 and 3 (Figure 4.21 b) and c)). The rupture forces show that we have a complete coverage of the substrate with one DPPC bilayer, i.e. we always see at least one rupture event. On top of this complete bilayer we have partial coverage of two and three additional bilayers (see Figure 4.20 a)). By averaging all curves with one rupture we obtained an average of 5.3 ± 2.4 nN. Force curves showing two ruptures (level two) show a first rupture at 5.6 ± 1.2 nN followed by a second rupture at 5.1 ± 1.1 nN. Finally, the force curves with three rupture events (level 3) rupture first at 5.3 ± 2.0 nN, followed by a second rupture at 5.2 ± 1.8 nN and a third rupture at 5.0 ± 1.7 nN. As seen, all ruptures in dry, non-hydrated SLBs occurred around 5nN and are independent of the number of layers. The averages and individual rupture forces are tabulated in Tables 6.1–6.3. To compare the mechanical properties of SLBs immersed in liquid, we applied AFM force curves to phospholipid bilayers fabricated under the same procedure (formed by physical vapour deposition in high vacuum) immersed in pure water in the AFM JPK NanoWizard™ Heating Cooling Module HCM™ accessory. We applied tip forces up to 15 nN and no rupture of the bilayer membrane was observed (see Figure 6.1).

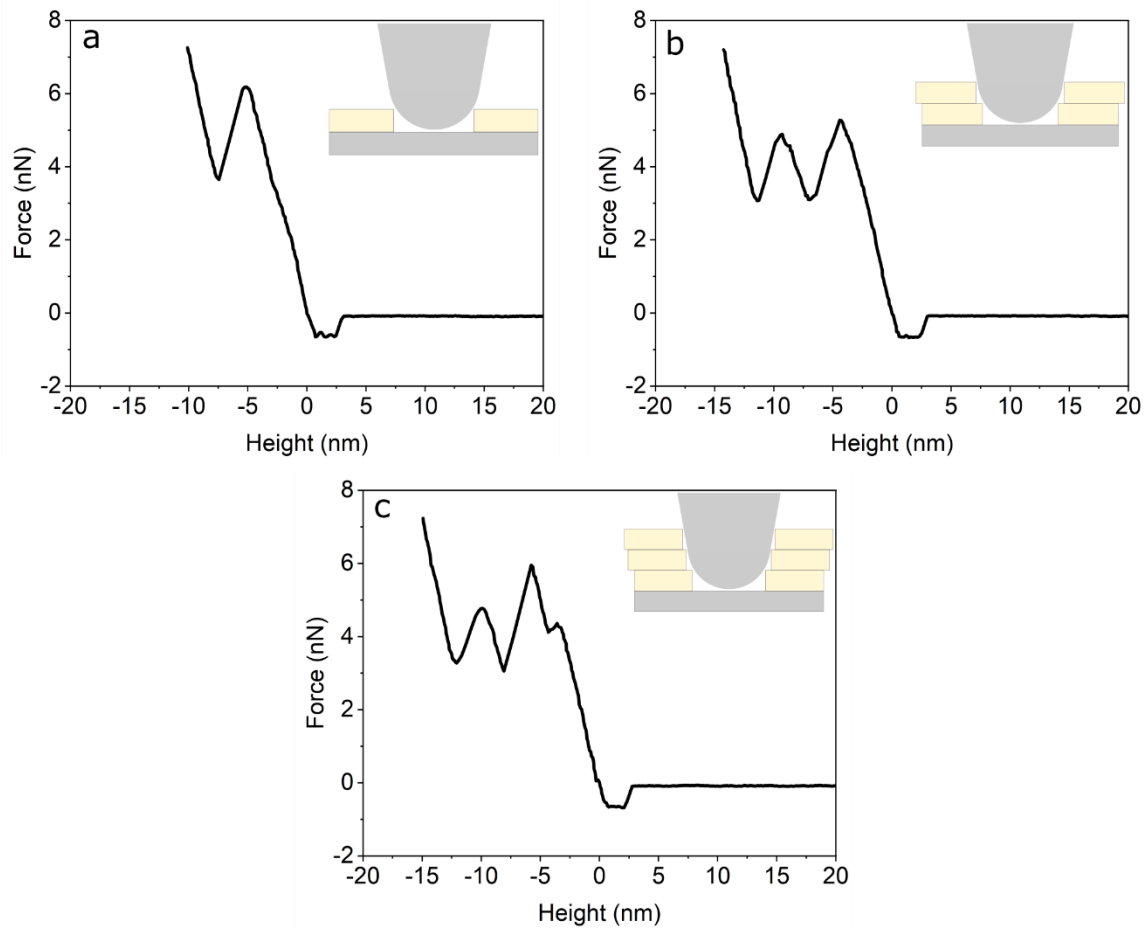

Figure 4.21. a) Force curve on the first bilayer (level 1). b) Force curve on the second bilayer (level 2). c) Force curve on the third bilayer (level 3)[71].

The measured AFM rupture forces in Figure 4.21 in dry conditions (~5 nN) were clearly lower than the values reported for liquid conditions. Rupture forces reported in the literature for a single bilayer of DPPC in physiological conditions are 20 nN, and this rupture force decreases to 13 nN in the absence of Mg^{2+} [73]. Our measurements of the mechanical properties of SLBs immersed in pure water show that the rupture force of the bilayers increased by at least three-fold, compared to dry phospholipid bilayers fabricated under exactly the same procedure (physical vapour deposition in high vacuum). In other words, the hydrated SLBs re stronger than the stable dry SLBs investigated herein (see Figure 6.1). On the other hand, the observed stability of these evaporated SLBs, analyzed with AFM with surfaces in water, confirmed that the first

DPPC bilayer, on top of the SiO_2/Si substrate, is anchored correctly with its polar head towards the SiO_2 substrate (head down configuration). In the opposite case, if anchored with the alkane legs towards the substrate (tail down configuration), the bilayer in contact with the substrate would be displaced or removed from the substrate, as we observed during previous studies of alkane layers adsorbed by velocity controlled dip-coating on the same substrate (dotriacontane $C_{32}H_{66}/SiO_2/Si$) [74]. In the case of nonpolar molecules, like alkanes, water intercalates between the hydrophilic SiO_2 substrate and the alkane molecules and displaces the alkanes, similar to the effect of penetrating oil on water films (WD-40™ or Caramba™ effect). The hydrophilic nature of the silicon substrate, which is defined by the cleaning procedure [63], combined with air humidity, could induce the formation of stable SLBs in air after the first heating cycle. However, this eventual adsorption of water from the laboratory atmosphere is very unlikely, given that the room temperature is above the dew point at the relative humidity of our laboratory (approximately 20%). Furthermore, our extremely sensitive VHRE was not able to detect the adsorption of water molecules underneath, inside or above the bilayer, which would be clearly distinguishable from the DPPC molecules given their different refractive indices and polarizabilities. Additionally, the AFM measurements showed no signs of the presence of a significant amount of water.

Our results have shown that SLBs fabricated by our dry two-step procedure can be used for applications in dry environments as well as for conventional applications under physiological conditions, taking advantage of the extended storage period of our dry and long-time stable SLBs. We believe that water helps the SLB to stabilize mechanically, exhibiting higher rupture forces under physiological conditions than in dry environments, as shown in Figure 4.21.

4.8 Study of the temperature cycles effect in the SLB using Ellipsometry and AFM

To confirm the DPPC bilayer formation, complementary ellipsometric measurements were performed in order to observe phase transitions, by applying heating and cooling temperature ramps between room temperature (RT) and 347 K. Figure 4.22 shows the variation in the polarizer angle (ΔP), which represents variations in the polarizability of the bilayer molecules [75]. The ellipsometric data , based on the models of Paul Drude [76] and the equivalent model [65] of Dignam and Fedyk [75], produces an interpretation of the collective behavior on a molecular scale. Figure 4.22 a) corresponds to the first temperature ramp applied to the sample of ~60 Å DPPC on SiO_2/Si, while Figure 4.22 b) and c) show the data obtained during the second and third heating ramp, respectively.

Changes in slope, I.e. the inflection points of the ellipsometric signal indicate changes in the phase of the DPPC bilayers. The three transitions measured in the sample corresponding to Figure 4.22 b) and c) are from left to right: The gel to ripple at 311 K, ripple to liquid crystalline at 322 K and liquid crystalline to fluid disordered at 330 K, respectively, marked in Figure 4.22 with vertical dashed lines. Further experiments on four different samples prepared under the same (all curves are shown in Figures 4.23–4.30) conditions produced a gel to ripple transition at 311.5 ± 0.9 K, ripple to liquid crystalline at 323.8 ± 2.5 K and a liquid crystalline to fluid disordered at 330.4 ± 0.9 K (see Table 6.4).

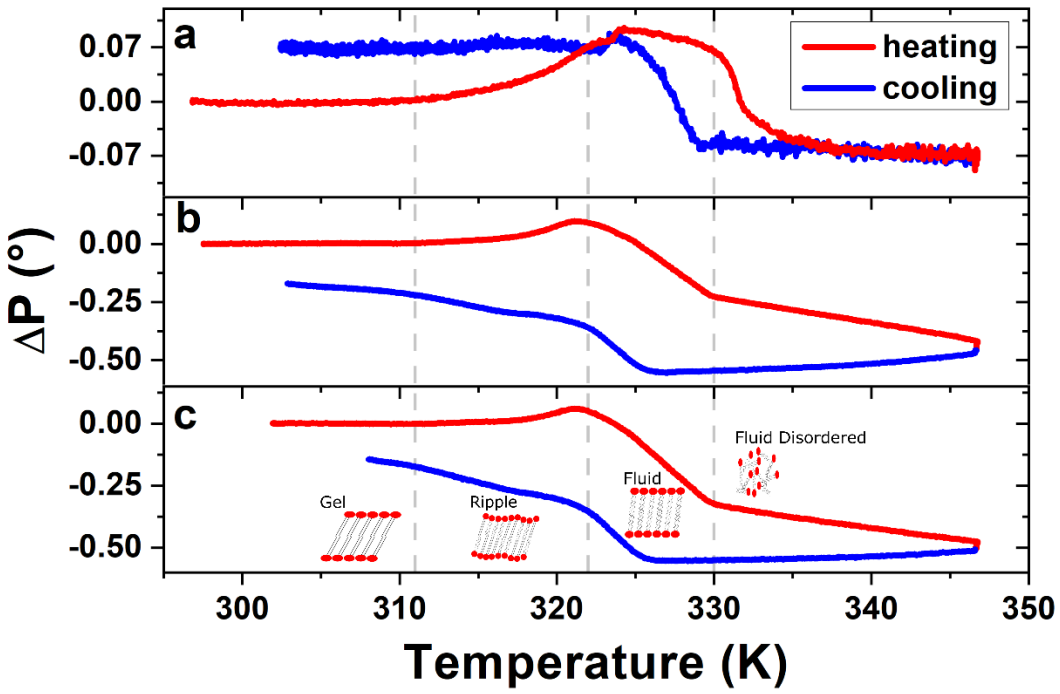

Figure 4.22. Ellipsometric changes in polarizer angle ΔP of DPPC bilayer, measured during a) the first, b) the second and c) the third heating–cooling cycle. Vertical dashed lines indicate the phase transition temperatures as described in the text. The ΔP signal of the following heating–cooling cycles show the same characteristics of figures b) and c), leading to the conclusion that the structure formed after the first heating–cooling cycle remains stable.

From the ellipsometry measurements, as shown in Figure 4.22, one can observe that after the first temperature cycle the general shape of the heating-cooling curve stabilizes, indicating that the first heating ramp produced an irreversible change in the morphology of the sample, which was maintained throughout the following heating-cooling cycles. In other words, the system was transformed into a stable structure at room temperature in a two-step self-assembly process; i.e., after the first heating ramp, no rearrangements of the molecules were observed in samples stored over at least fifteen months (see Figure 6.9). This contrasts to previous observations of alkane monolayers, which are metastable at room temperature, showing mobility that leads to the formation of macro-crystals and depleting areas around them [77]. The phase transitions seen in Figure 4.22 are characterized by different collective molecule

behaviors [52]. The gel phase is an ordered phase formed by slightly inclined phospholipid molecules. In this phase, the ellipsometric signals remain constant. At 311.5 K we see a smooth onset of the gel to ripple transition, caused by increased molecular dynamics, resulting in an undulated surface and a straightening of the molecules. This straightening of the molecules leads to an increase in the measured polarizability of the molecules, which in our setup is reflected by an increase in the signal. At 323.8 K, the transition from ripple to liquid crystalline (fluid ordered) phase occurs, which implies a collective inclination of the molecules and an increase of gauche defects or kinks in the alkane chains of the phospholipid molecules, dramatically reducing their contribution to the measured polarizability, or ellipsometric signal [65]. At 330.4 K the system starts the transition from liquid crystalline to the fluid disordered phase, where the bilayer structure disappears completely and the surface converts into an almost flat fluid, where the average orientation of the molecules contributes even less to the measured polarizability, or ellipsometric signal. The transition temperatures for ripple to liquid crystalline and liquid crystalline to fluid disordered suggests the existence of a structural first-order phase transition [78], [79].

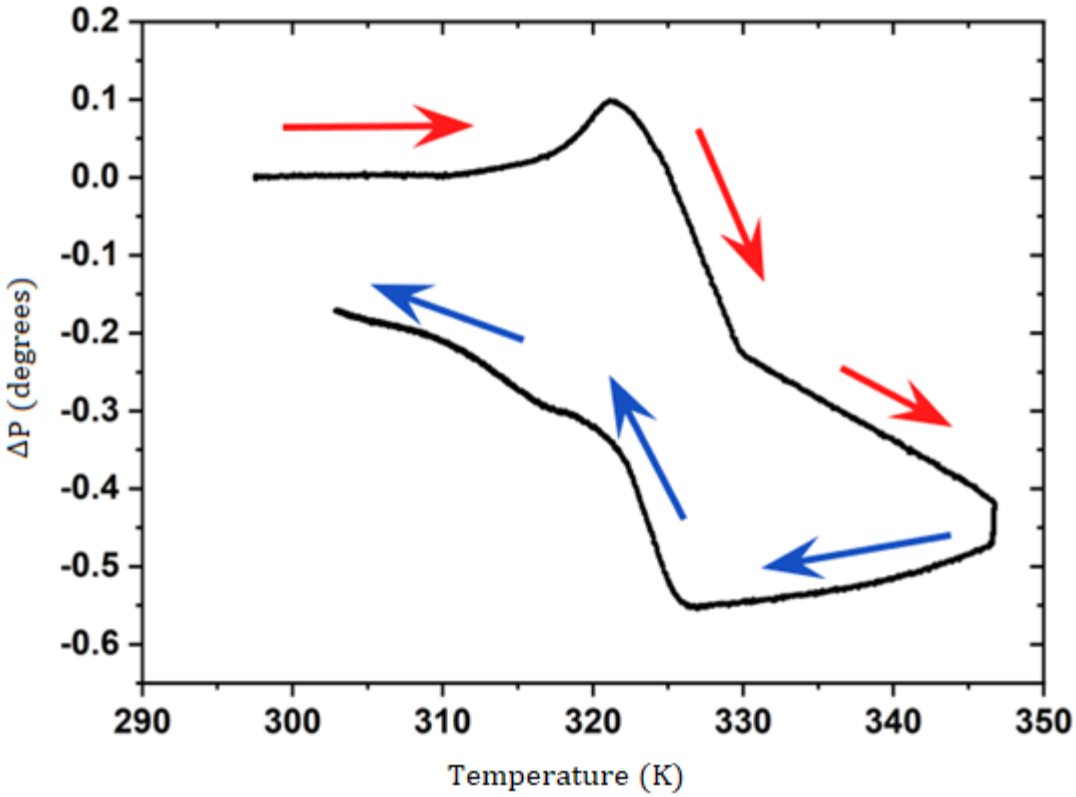

Figure 4.23: Temperature ramp ΔP (degrees) vs. Temperature (K) corresponding to sample NE01 ramp number 7.

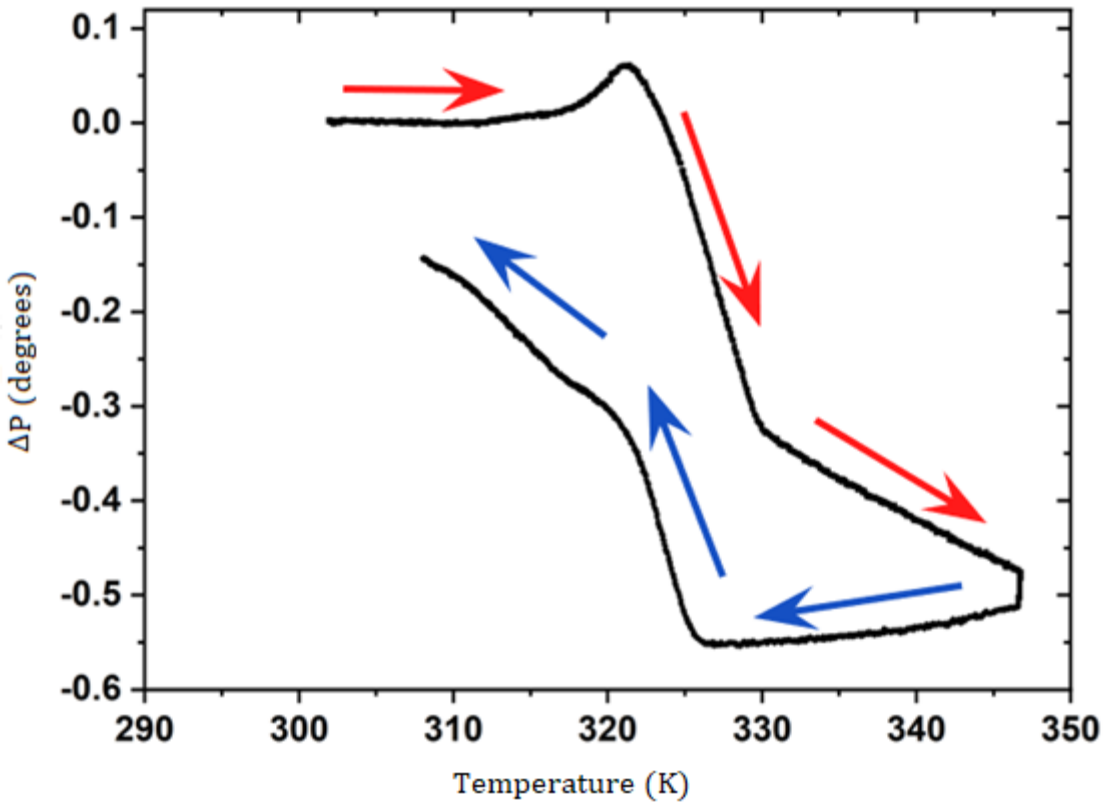

Figure 4.24: Temperature ramp ΔP (degrees) vs. Temperature (K) corresponding to sample NE01 ramp number 8.

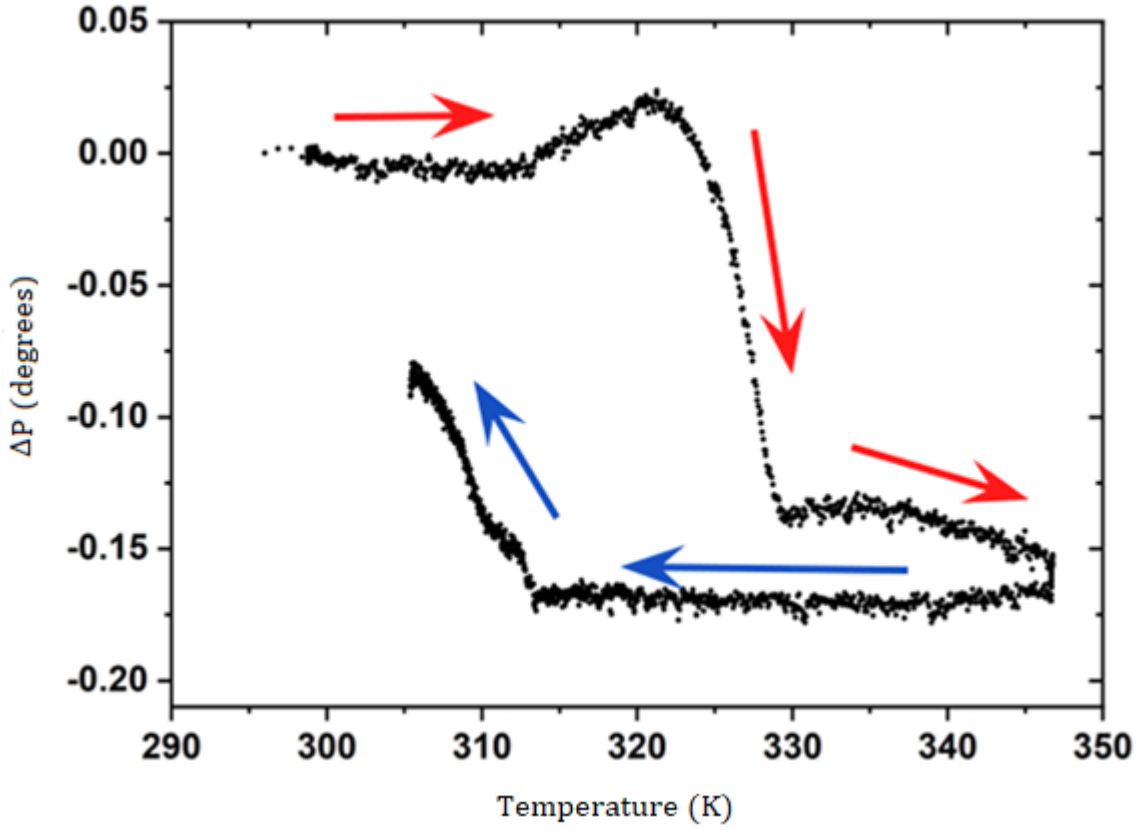

Figure 4.25: Temperature ramp ΔP (degrees) vs. Temperature (K) corresponding to sample H14 ramp number 3.

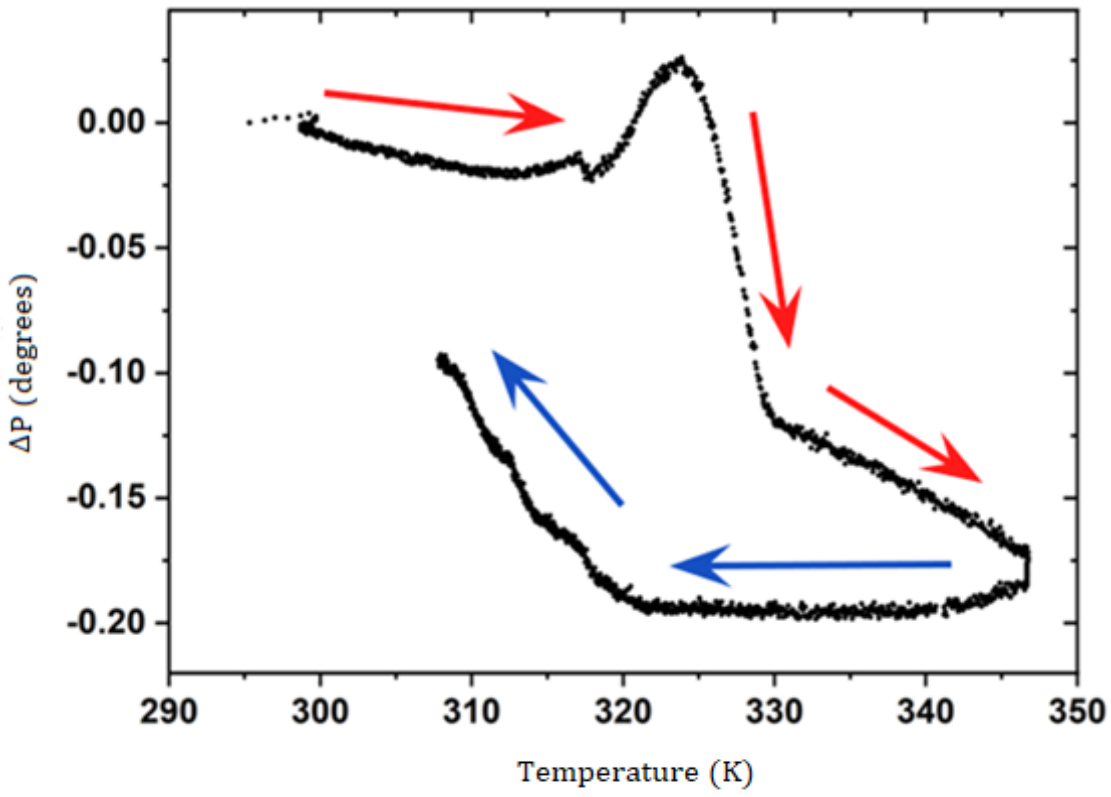

Figure 4.26: Temperature ramp ΔP (degrees) vs. Temperature (K) corresponding to sample H14 ramp number 6.

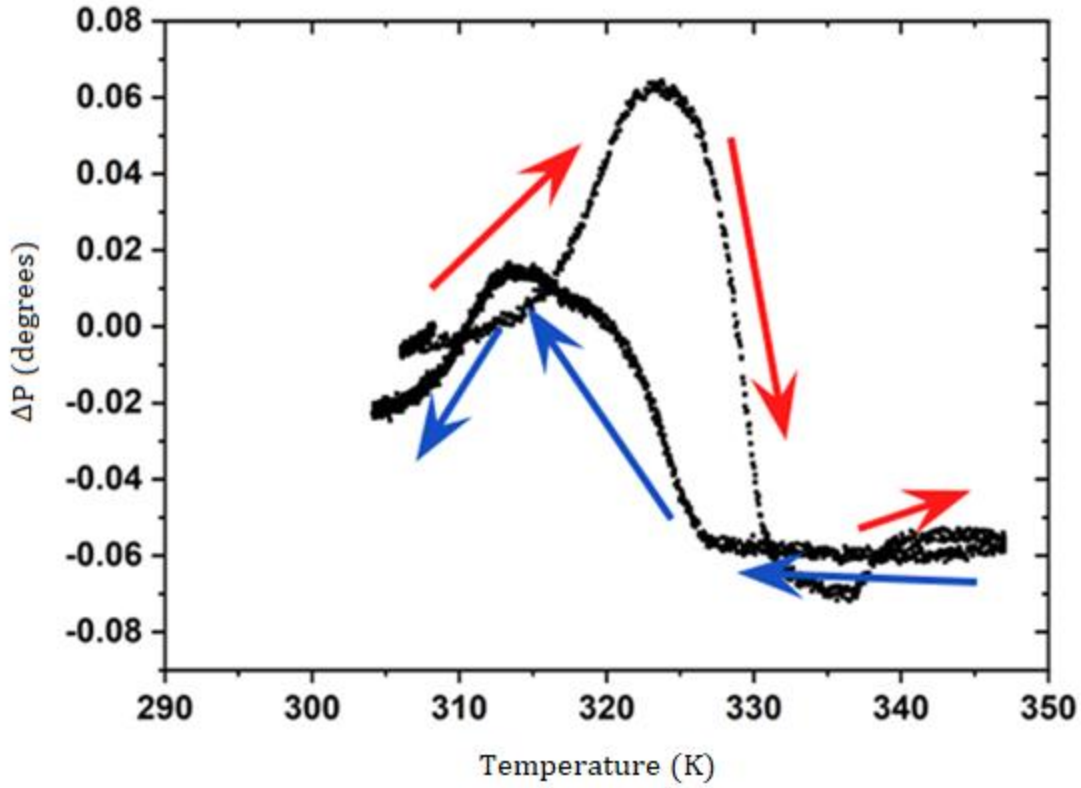

Figure 4.27: Temperature ramp ΔP (degrees) vs. Temperature (K) corresponding to sample H15 ramp number 5.

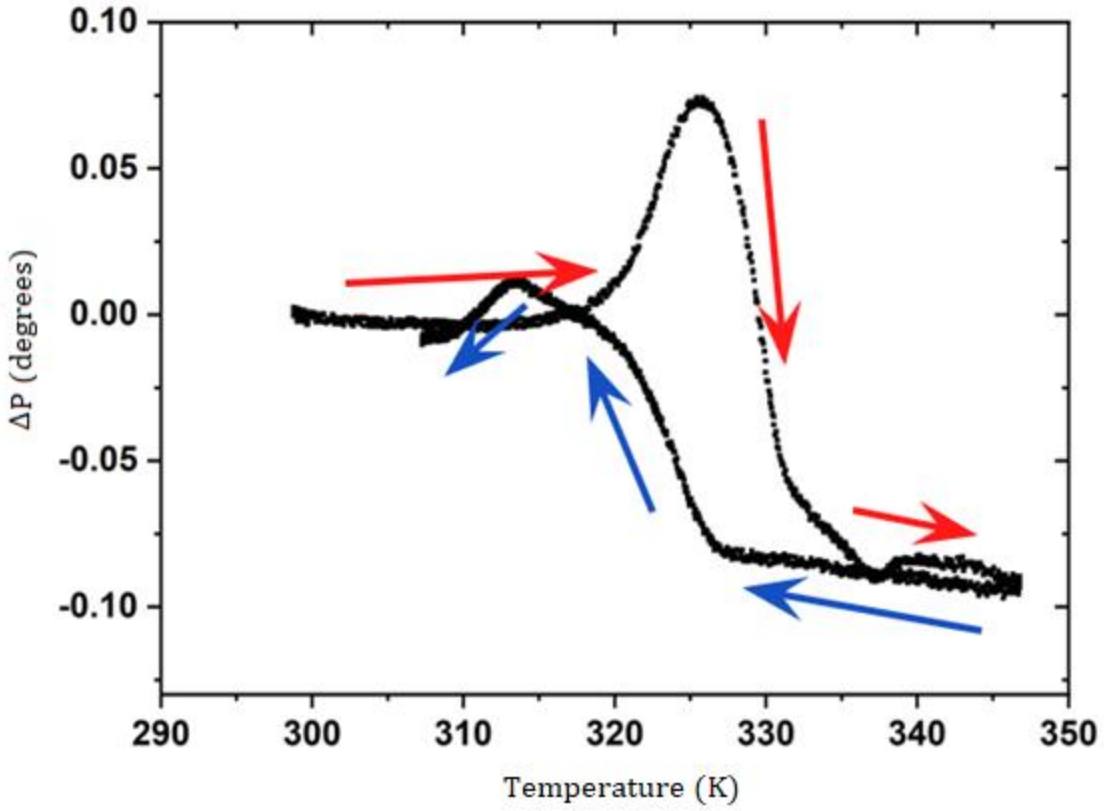

Figure 4.28: Temperature ramp ΔP (degrees) vs. Temperature (K) corresponding to sample H15 ramp number 6.

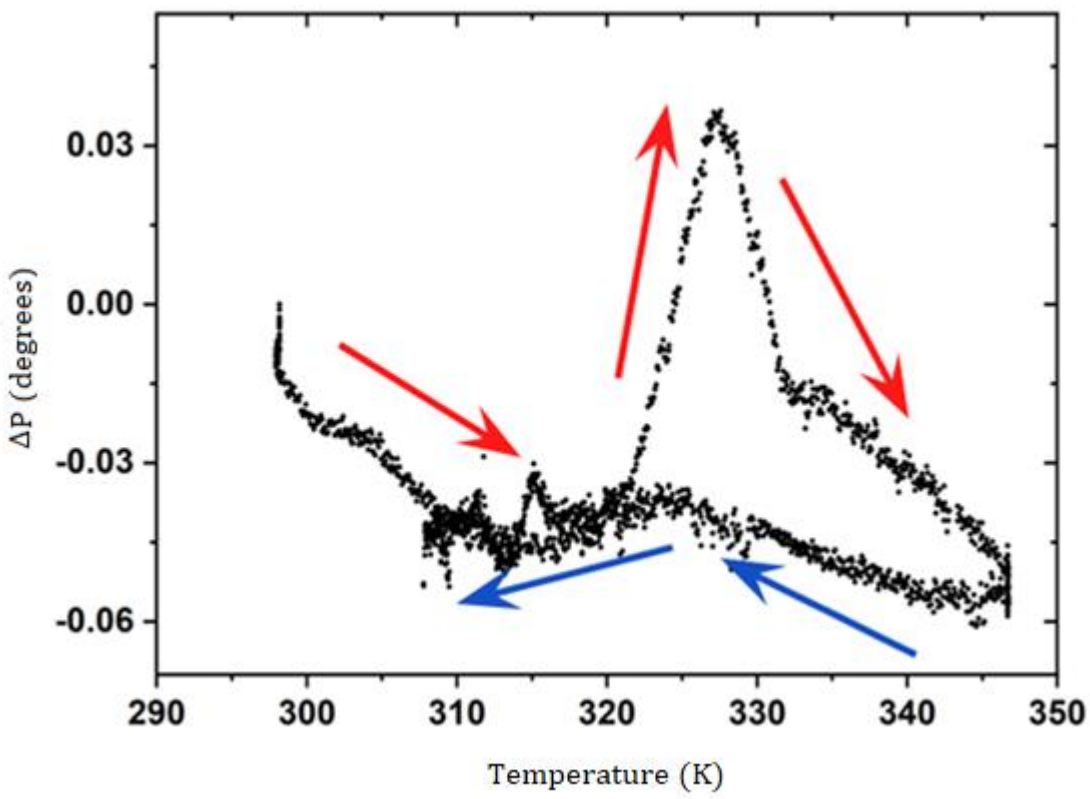

Figure 4.29: Temperature ramp ΔP (degrees) vs. Temperature (K) corresponding to sample H16 ramp number 6

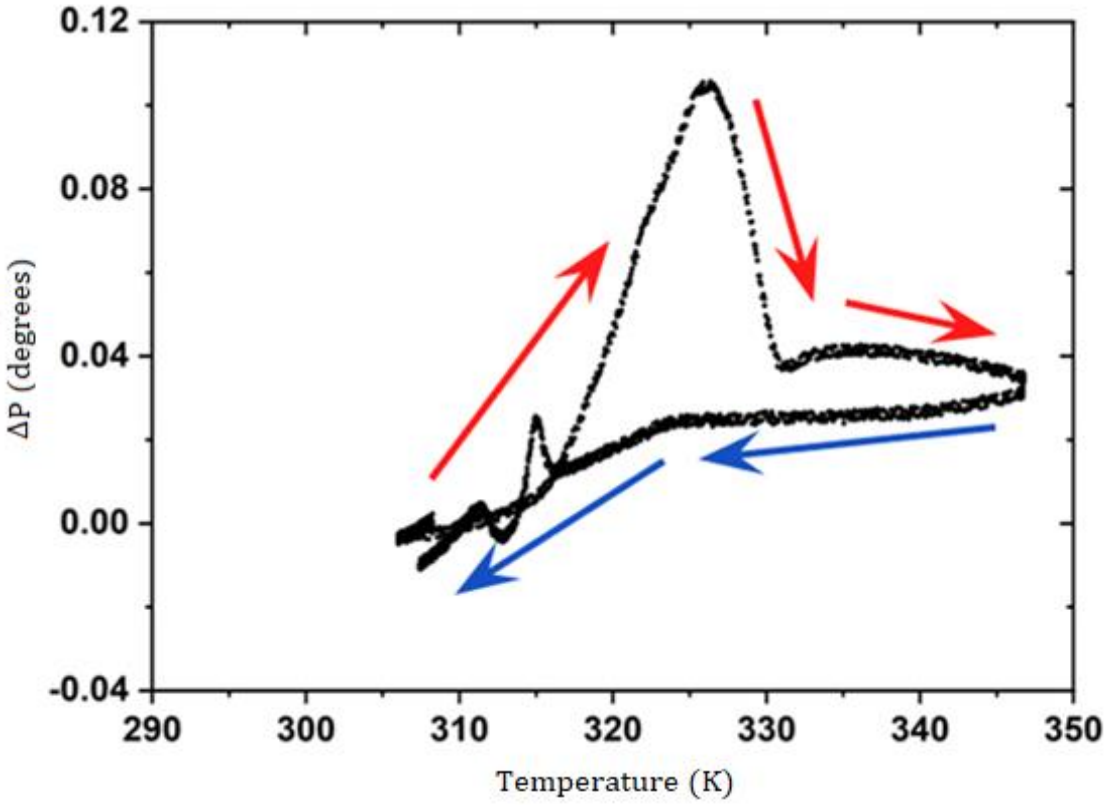

Figure 4.30: Temperature ramp ΔP (degrees) vs. Temperature (K) corresponding to sample H16 ramp number 7

Given that the transition seen at 311 K (gel to ripple) is a smooth continuous transition, we performed complimentary QI™ AFM measurements in this low temperature range. Adhesion maps of 2 µm × 2 µm were recorded over a total of 3 SLB samples. Temperature ramps were taken using steps of 5 K, starting from room temperature to 328 K. Figure 4.31 a)–c) shows the adhesion maps at temperatures 296 K, 308 K and 323 K. A noticeable change in adhesion is observed between images when compared in the same adhesion range (1–20 nN). By extracting the adhesion distribution at the different temperatures and obtaining the center and half width of the distribution, the average adhesion force was then plotted as a function of temperature, as shown in Figure 4.31 d), for three representative samples. Another adhesion map used to build the graph in the Figure 4.31 d) is shown in the Figure 6.4. As seen in

Figure 4.31 d), the adhesion value rises between room temperature and 308–312 K and then drops abruptly.

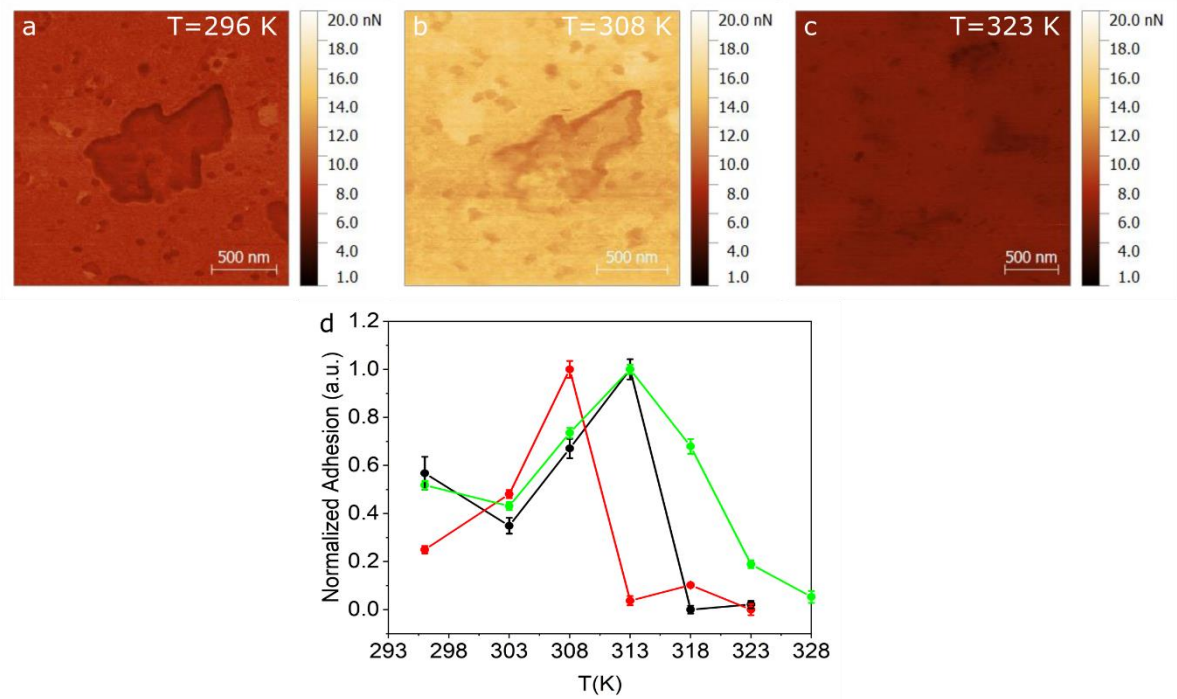

Figure 4.31. Adhesion maps obtained using QI^{TM} mode for (a) 296 K (b) 308 K and (c) 323 K. (d) Normalized adhesion taken for three different samples as a function of temperature.

AFM adhesion measurements in Figure 4.31 exhibit two regimes, one where the adhesion increases between room temperature and ~308–313 K and a regime where the adhesion drops above 313 K. From the literature, it is known that the temperature range of the gel-ripple transition corresponds to 306–310 K [31]. We believe that the increase in adhesion as seen in Figure 4.31 between room temperature up to 308–312 K, is related to the appearance of ripples in the membrane. These ripples have a reported wavelength of 14 nm [80], which is comparable to the AFM tip radius, which means the tip could fit partially within the groves, generating an increase in contact area and, therefore, an increase in adhesion, as compared to a flat and unwrinkled membrane. The three curves in Figure 4.31 show a maximum range between 308 and 312 K, after which the adhesion shows a sharp decrease related to a phase transition. This temperature range falls within the reported values for the ripple to liquid crystalline

phase transition [31]. We believe that this sharp drop is related to the ripple to liquid crystalline transition given that the membrane smoothens, i.e., loses its ripples, generating a decrease in the contact area with the tip.

4.9 Effect of the AFM tip over the scanned area

For further proof of the formation of dry phospholipid bilayers, we draw on a more detailed study of the well-known behavior of conventionally wet produced SLBs. Attwood et al. [81] and Gosvami [82] described an AFM-tip induced changes in morphology of SLBs on mica produced by vesicles in water (DOPC, DPPC) and by the Langmuir–Blodgett (LB) technique (DODAB), respectively. In both cited studies, AFM measurements performed in water show a morphological modification of the scan area due to the interaction of the SLB with the cantilever tip. We analyzed the tip-surface interaction as a function of temperature and compared our AFM measurements with temperature-dependent ellipsometric analysis. The latter is a non-invasive method, based on low energy photon-solid interactions, which does not affect the structure of the molecules nor the morphology of the crystalline or fluid ordered phases. In other words, we analyzed the topographical channels as a function of temperature to study structural changes in the film. Figure 4.32 shows AFM topography images before and after temperature ramps, ranging between room temperature (RT) and 347 K, performed within the ellipsometer (Figure 4.32 a)–c)) and within the AFM (Figure 4.32 d)–f)). Figure 4.32 a) shows the topography of the evaporated SLBs at RT before the first temperature ramp was performed within the ellipsometer. In Figure 4.32 b) and c), we observe the sample at RT after the first and sixth temperature ramps carried out within the ellipsometer, respectively. A reorganization of the initial surface (Figure 4.32 a)) into an even more homogeneous bilayer surface was observed (Figure 4.32 b) and c)). In order to study the reorganization of the sample shown in Figure 4.32 a)–c), we performed temperature cycles within the AFM to map the surface topography with increasing temperature operating in air. The AFM topography images were taken every 5 K throughout the ramps, starting from RT up to 343 K (see Figure 6.6). Figure 4.32 d) shows the topography of the evaporated DPPC sample before any temperature ramp. The morphology of Figure 4.32 d) is similar to that of Figure 4.32 a). Figure 4.32 e) shows the AFM topography of the SLBs after the first temperature ramp was performed within the AFM in the same scanning zone as Figure 4.32 d). Figure 4.32 f) shows the AFM topography of the same sample after the first temperature in a contiguous region

to the scanned area shown in Figure 4.32 e), i.e., it was not imaged during the temperature cycle. The scanned area during the temperature cycle (Figure 4.32 e)) has a roughness parameter (R_q is referred to as the root-mean-square roughness) of R_q = 28 nm, while the contiguous region (Figure 4.32 f)) has a roughness of R_q = 3.3 nm.

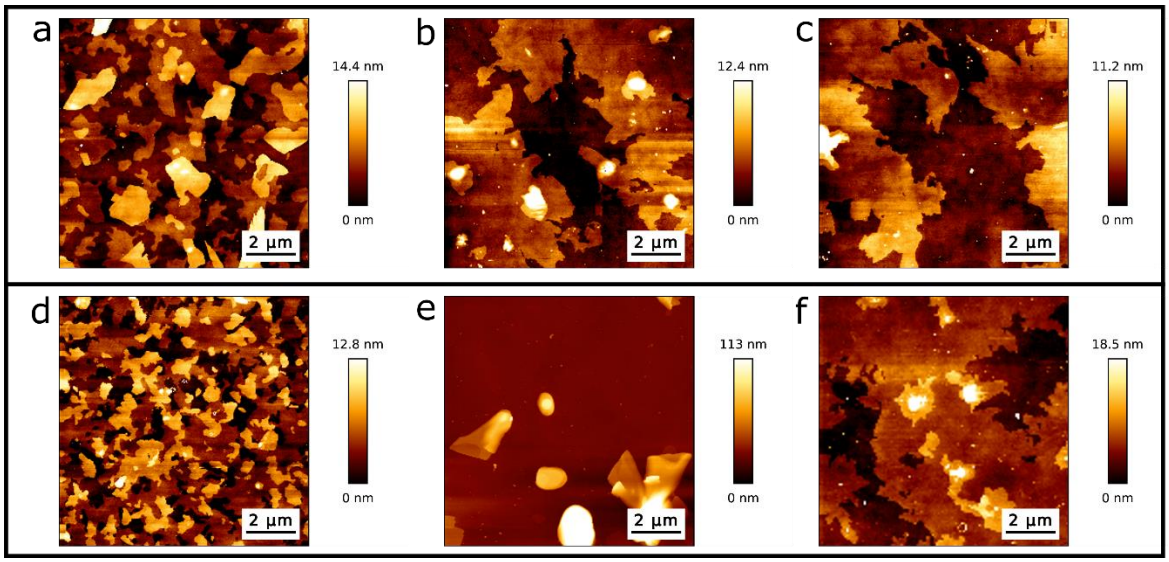

Figure 4.32. Topographic AFM images from DPPC/SiO_2/Si samples at RT: a) directly after evaporation and before the first temperature cycle, b) after the first and c) sixth temperature cycle performed within the ellipsometer. d) The topography image directly after evaporation and before temperature cycling within the AFM, e) after the first temperature cycle while scanning with AFM, and f) after the first temperature cycle in a contiguous region to the scanned area.

By the observation of Figure 4.33, the AFM topography images lead us to believe that the AFM tip is interacting with the SLB in air, affecting its morphology and roughness, during the heating cycle. Restructuring of an SLB on mica due to tip interactions has been reported on DODAB, DOPC and DPPC on mica in liquid [81], [82]. It is important to emphasize that in the AFM images seen in Figure 4.33 a)-d) and in Figure 4.33 f), the first layer, corresponding to an initial height of 0 nm for the AFM data, contains a complete phospholipid bilayer, which was confirmed by the observation of a single rupture event in the force curves. Meanwhile in Figure 5e there is no DPPC bilayer in the first height layer, since it was removed and piled up due to

the interaction between the AFM tip and the sample during the temperature cycle. This was confirmed by force curves which do not show a rupture event.

To quantify the effect of the tip - SLB interaction we performed AFM imaging in air at RT upon DPPC single- and double bilayers. Consecutive AFM images were obtained in intervals of 7 minutes. In figure 4.33, one can observe the dynamics of a double bilayer and a single bilayer induced by the AFM tip. A total of 10 AFM images were recorded. The first 5 images were taken at a force set point of 1 nN (figure 4.33 a) to c)), while the following 5 were taken at 3 nN (figure 4.33 d) to f)). There is a clear reduction of the double bilayer area, as well as, a restructuring of the single bilayer.

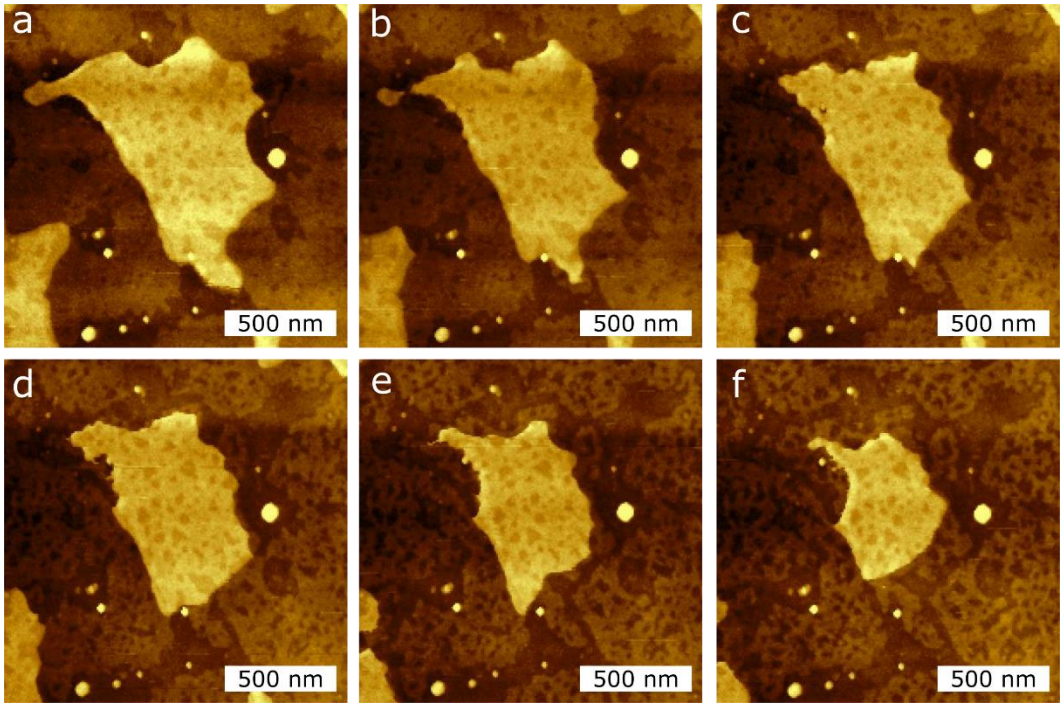

Figure 4.33: AFM topography images of the DPPC bilayer taken at RT in air during consecutive measurements in the same scan region (2 µm × 2 µm), initiated to induce the reduction of the island-like DPPC bilayer surface area, applying two different tip forces, a)–c): 1 nN; d)–f): 3 nN.

The holes seen in the SLBs in Figure 6 were measured by taking cross-sections that have a depth of ~1.2 nm, which is independent of the loading force. We believe these holes are due to a local interdigitation or intercalation of the alkane legs or gauche

defects/kinks in the lipid molecules' hydrocarbon chains. From these measurements one can see that the SLB is a dynamic system that interacts with the AFM tip in air, even though the applied forces are below any possible rupture of the membrane (<5 nN).

We measured the area of the DPPC islands, as seen in Figure 4.33, by masking the image by height using an image processor (Gwyddion) and obtaining the area as a function of scan number, for two different applied tip forces. Figure 4.34 shows the reduction in area of the DPPC islands as a function of scan number. For scan numbers 1–5, the applied force was 1 nN, and for scan numbers 6–10, 3 nN. The measured area reduction follows a linear behavior and there is a clear difference in rates between two applied tip forces. For a set point of 1 nN the measured reduction rate was -2.4×10^4 nm^2/scan and for 3 nN we obtain -6.5×10^4 nm^2/scan.

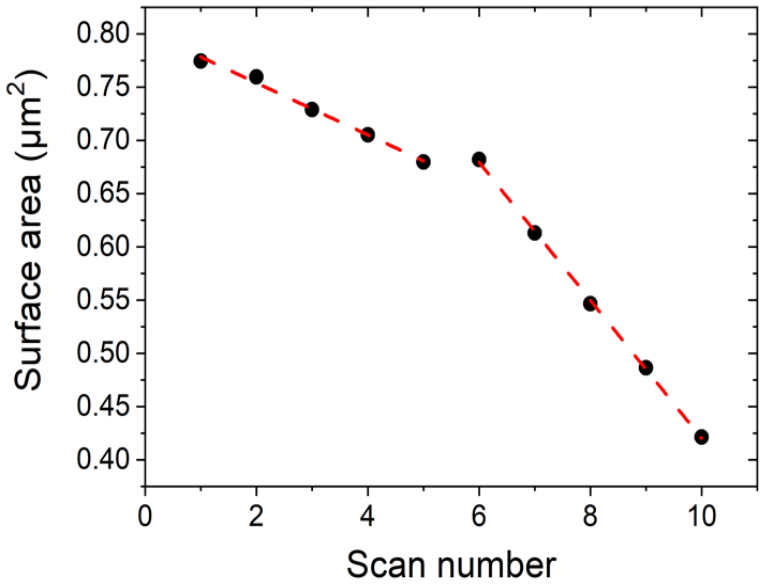

Figure 4.34. Surface area reduction during consecutive scans at RT using two different tip forces applied in the same scan regions. Scans 1–5 are taken at 1 nN, while scans 6–10 are taken at 3 nN.

We also analyzed the depth of the holes created by the AFM tip in the SLBs, as seen in the second bilayer island of Figure 4.33. The average hole depth was 1.2 ± 0.4 nm, as measured by cross-sections over the hole (see Figure 6.8). These holes are lower in height than the DPPC monolayer thickness, and do not change with the different setpoints used, i.e., 1 nN and 3 nN.

Figure 4.34 shows the reduction rate dependence on the external tip force. We emphasize that these results are time-independent. The observed reduction only depends on the number of scans and on the intensity, i.e., force setpoint 1 nN or 3 nN, of the "hammer blows" executed by the AFM tip. During these measurements in QI™ mode, only vertical forces act on the surface. In other words, there are no lateral forces involved, except on the borders of the bilayer islands. This means we are not dragging material across the scanned area, so we can rule out this effect on the reduction dynamics seen in Figure 4.34.

5. Conclusions

In this work, we have shown a dry two-step method for SLB formation, consisting of thickness-controlled phospholipid deposition in high vacuum onto bare SiO_2/Si substrates, followed by a subsequent heating cycle performed in air. The SLBs were stable in air without the application of water or buffer solution to the sample. These vapor-deposited SLBs exhibited phase transitions, which we measured using VHRE in air, which were found to be consistent with literature values of SLBs in liquid. The observed phase transitions lead us to believe that our SLBs are biologically functional. AFM measurements carried out in air exhibited rupture forces which were roughly 5 nN. These rupture forces were lower than values we measured in liquid (>15 nN) for samples prepared under the same conditions. This confirmed that water has a stabilizing effect on the mechanical properties of the membranes. Our control measurements in water corroborated that the first monolayer of the vapor-deposited stable DPPC bilayer assembled with the polar heads towards the substrate. We have observed that our SLBs tend to restructure in air when interacting with the AFM tip, even though the applied forces were lower than the rupture force. Our evaporated membranes showed long-term stability and no restructuring after storage in air for at least nine months. This extreme stability of the SLB structures studied herein makes this system interesting for technical applications in the field of functional biointerfaces, e.g., for the fabrication of biosensors and membrane protein platforms, including cleanroom-compatible fabrication technology. Our SLBs could also help us gain insight into the lifetime of viral structures protected by a surrounding phospholipid bilayer adsorbed on static solid surfaces or on inhalable particulate material (PM), which contributes to the spread of the SARS-CoV-2 virus.

6. Supporting information

6.1 Measuring the rupture force of the bilayer

The determination of the rupture force was realized with AFM force curves using force mapping mode on a 7 μm x 7 μm area. We analyzed the breakthrough events at all observable points, which showed 1, 2 or 3 breakthrough events. With these measurements we corroborated that we can form a complete phospholipid bilayer on the silicon substrate and that the measured force value is similar independent of the number of the breakthrough events. Table 6.1 show the values of different rupture forces of curves that showed only one rupture. Table 6.2 show the values of different rupture forces of curves that showed two ruptures. Table 6.3 show the values of different rupture forces of curves that showed three ruptures. Figure 6.1 show force curves of the DPPC bilayer in water conditions that not show ruptures at least at 16 nN.

Peak 1	
Position (nm)	Height (nN)
−0.9	0.6
−4.6	6.4
−4.8	6.6
−4.8	7.1
−1.4	0.8
−5.0	6.9
−4.9	6.6
−5.4	6.7
−5.0	6.6
−5.1	6.2
−3.1	3.9
Average	5.3
Standard deviation	2.4

Table 6.1. Value of different rupture forces of curves that showed only one rupture.

Peak 1		Peak 2	
Position (nm)	Height (nN)	Position (nm)	Height (nN)
−0.7	0.8	−1.3	1.1
−6.6	7.0	−11.3	7.0
−4.7	6.0	−9.5	5.0
−5.0	6.9	−9.7	5.9
−5.1	5.2	−9.4	4.9
−5.6	6.6	−8.4	4.7
−5.5	6.8	−9.6	5.5
−5,6	5.9	−9.8	5.3
−5.1	5.6	−10.6	6.5
−6.0	5.5	−9.8	4.9
−5.7	6.6	−8.7	4.0
−4.8	5.4	−9.0	5.0
−4.6	6.2	−9.3	4.9
−4.3	6.0	−7.9	4.8
−5.3	5.5	−10.0	5.5
−4.0	5.4	−8.3	3.7
−5.2	6.5	−9.8	5.5
−4.8	5.3	−8.4	3.9
−4.3	4.7	−9.4	4.7
−5.7	5.0	−10.0	5.3
−4.2	5.3	−9.4	5.3
5.1	5.4	−10.6	6.3
−4.7	5.6	−9.9	6.1
−5.1	6.9	−10.3	5.8
−4,1	4.8	−9.3	4.3
−4.4	5.3	−9.3	4.9
−5.8	6.2	−9.3	4.9
−4.0	4.2	−9.3	5.2
−4.6	6.3	−8.8	6.0
Average	5.6		5.1
Standard deviation	1.2		1.1

Table 6.2 Value of different rupture forces of curves that showed two ruptures.

Level 3		Level 2		Level 1	
Position (nm)	Vertical Deflection (nN)	Position (nm)	Vertical Deflection (nN)	Position (nm)	Vertical Deflection (nN)
−5.7	6.9	−9.7	7.1	−13.6	6.9
−6.1	6.9	−10.0	6.6	−14.8	6.8
−6.3	7.2	−9.7	5.9	−13.6	5.7
−4.2	5.8	−8.2	5.1	−9.9	5.4
−3.6	4.4	−5.7	6.0	−9.9	4.8
−4.3	6.1	−8.8	5.8	−9.8	5.6
−2.1	2.1	−6.6	2.3	−9.1	2.7
−2.4	2.7	−4.1	2.5	−6.4	2.4
Average	5.3		5.2		5.0
Standard deviation	2.0		1.8		1.7

Table 6.3 Value of different rupture forces of curves that showed three ruptures.

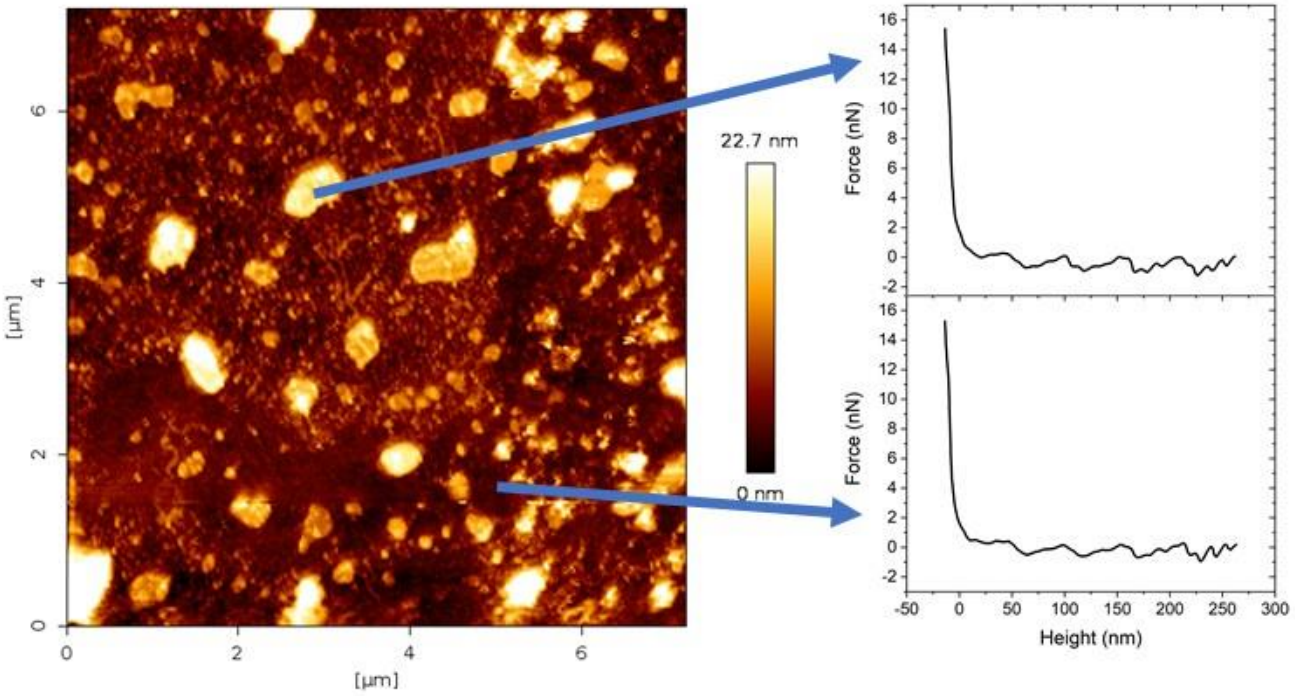

Figure 6.1. Left panel: Vapor deposited DPPC membrane in liquid conditions measured with AFM. Right panel: Force curves on a bilayer island (top panel) and bottom level (lower panel). Force curves show no evidence of a rupture.

6.2 Measuring the phase transition temperature

The determination of the phase transition temperature was realized using four different samples and two ellipsometric curves (not considering the first temperature cycle) of each sample. Each sample was constructed in similar conditions of pressure and evaporation rate controlled by the termocoax® current applied. The film thicknesses were above the 40 Å and below 80 Å and we believe that the differences of the curves formed is due to these thickness variation, but it is important to emphasize, that the phase transition temperature can be detected independently of the film thickness as expected.

The analysis of the data is shown in figure 6.2 and the detailed example is shown in figure 6.3. The objective of this analysis was to determine the changes in the slope associated with the changes in the behavior of bilayer molecules attributed to the changes in the phase of the system. For this purpose, a linear curve was fitted to the consecutive linear behavior part of the curve; to the point where the linear fittings crossed, we assigned the temperature where the phase transition is occurring.

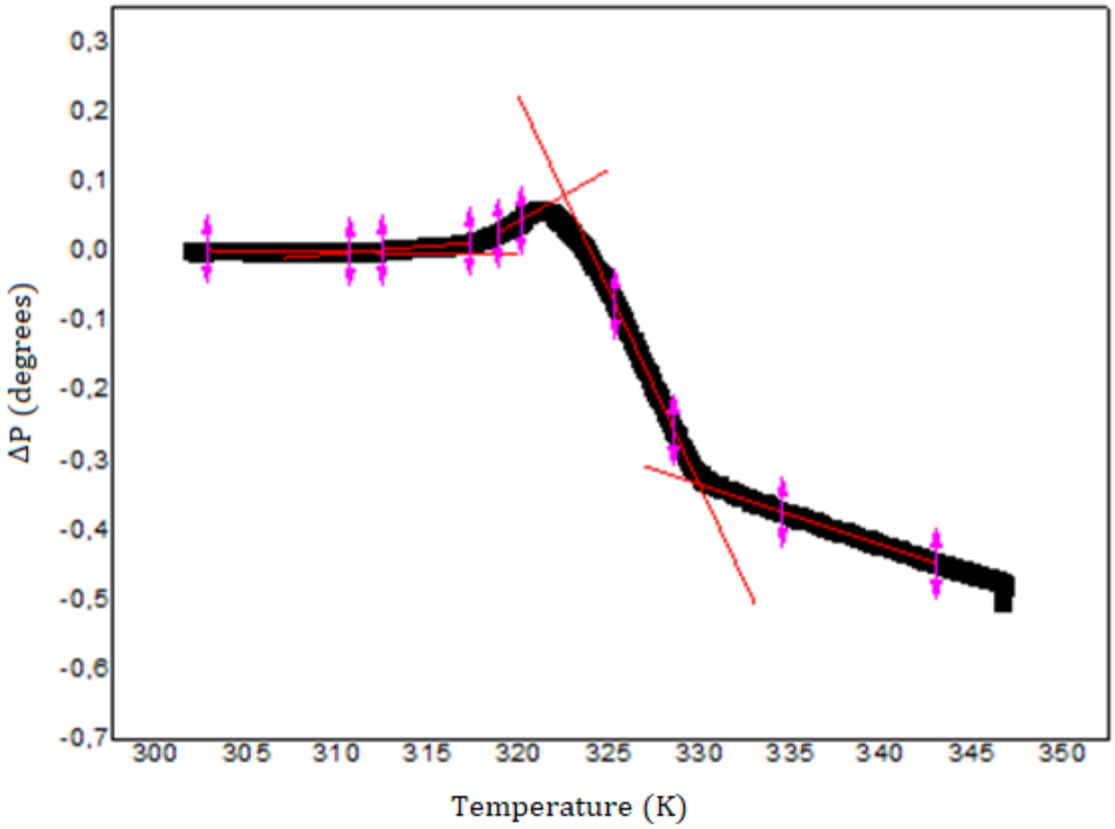

Figure 6.2: Example of the linear fitting realized to the ellipsometric curves obtained from the thermal cycle applied to the samples.

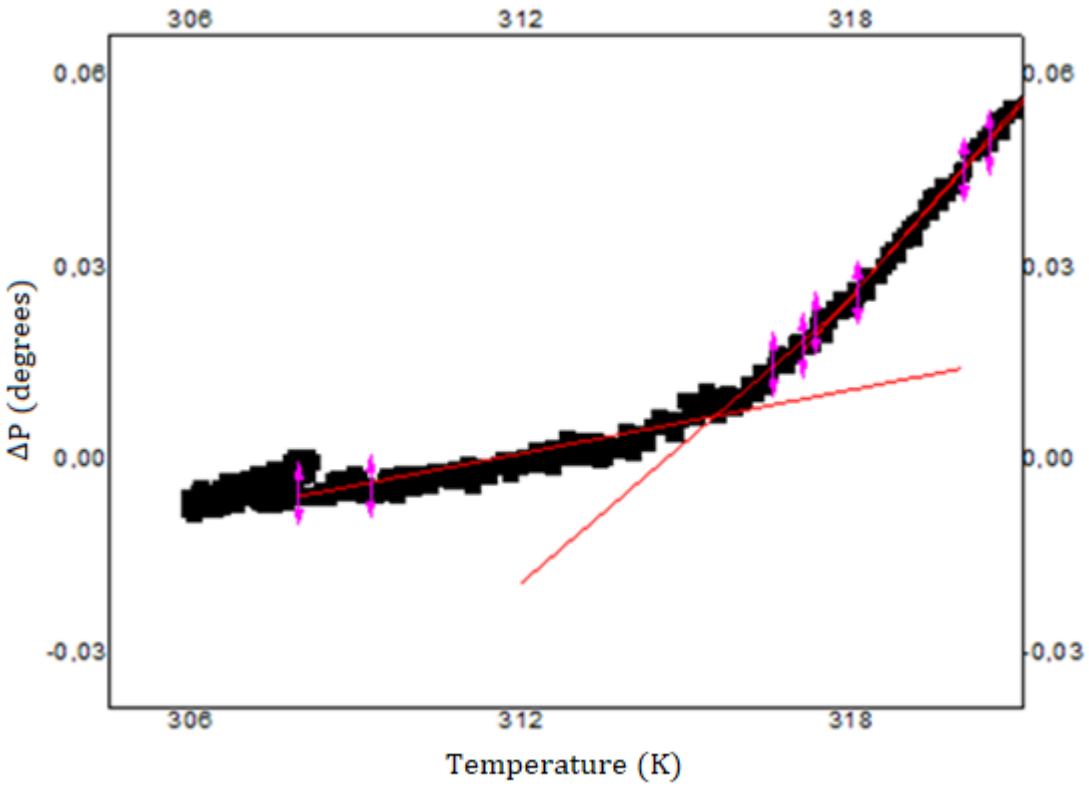

Figure 6.3: Detailed example of the linear fitting realized to the ellipsometric curves obtained from the thermal cycle applied to the samples.

The results obtained from the linear fitting on the ellipsometric curves are placed in table 6.4. The results showed that the values of the phase transition temperature have a standard deviation below 1 K for the Gel-Ripple and Liquid Crystalline-Fluid Disordered transitions and in the case of Ripple – Liquid Crystalline transition, the standard deviation increased up to 2.5 K. In all of cases, the value of the phase transitions are concordant with the literature despite the small standard deviations measured.

Sample	Ramp number	Temp (Gel-Ripple)	Temp (Ripple-Liquid Crystalline)	Temp (LC-Fluid Disordered)
NE01	**7**	311.3	321.3	329.9
NE01	**8**	310.9	321.1	330.0
H14	**3**	311.0	321.3	329.4
H14	**6**	312.4	323.9	329.5
H15	**5**	310.0	323.4	330.9
H15	**6**	311.4	325.6	331.1
H16	**6**	312.8	326.6	330,3
H16	**7**	312.3	327.3	332.1
Average		**311.5**	**323.8**	**330.4**
Standard deviation		**0.9**	**2.5**	**0.9**

Table 6.4 Values for the temperatures in Kelvin of three different phase transitions obtained from 8 ellipsometric measurements on 8 different samples.

6.3 Adhesion map measurements using AFM

Adhesion maps of 2 µm × 2 µm were recorded for a total of 3 SLB samples. Temperature ramps were taken using steps of 5 K, starting from room temperature to 328 K. Figure 6.4 show the adhesion maps obtained using QI™ mode for sample H14 (a) 296 K (b) 308 K and (c) 323 K and sample H15 (d) 296 K (e) 313 K and (f) 323 K. Figure 6.5 shows (a) adhesion map of silicon at room temperature after a complete heating-cooling cycle and (b) Histogram of the white rectangle shown in the adhesion map that represents the substrate, silicon.

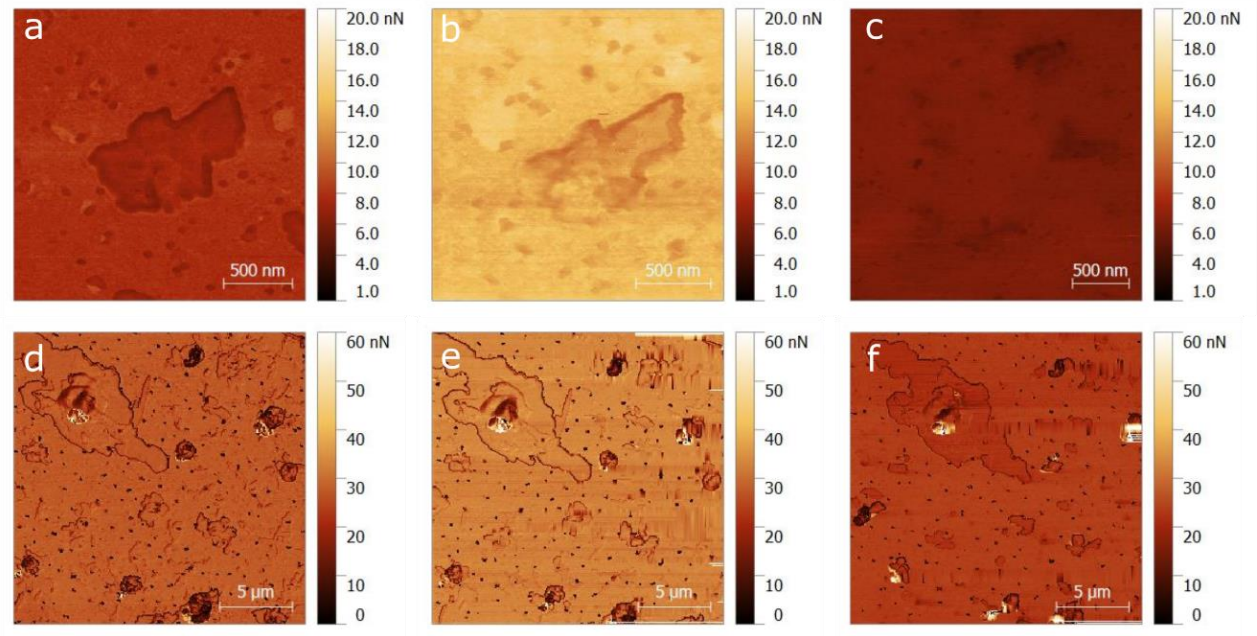

*Figure 6.4 Adhesion maps obtained using QI™ mode for sample H14 (**a**) 296 K (**b**) 308 K and (**c**) 323 K and sample H15 (**d**) 296 K (**e**) 313 K and (**f**) 323 K.*

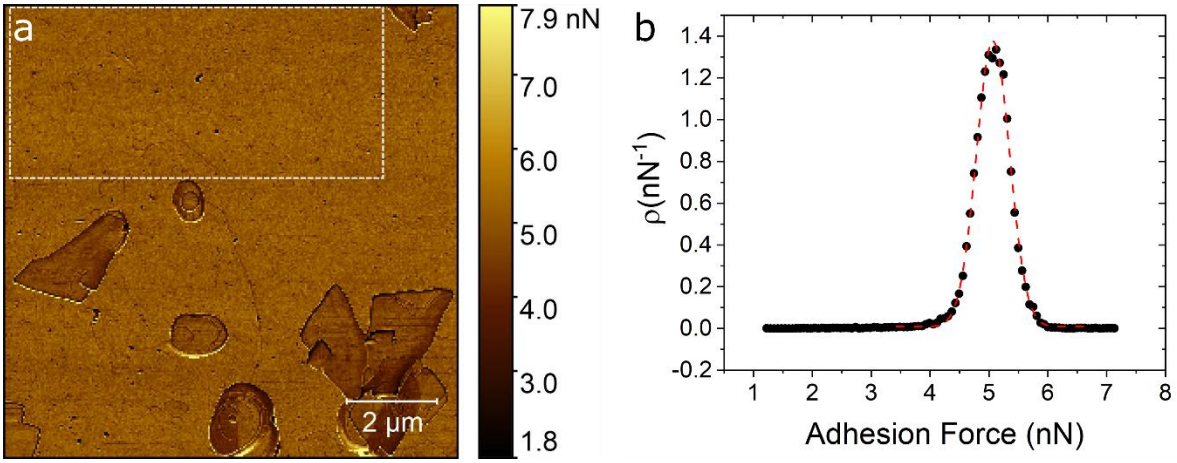

Figure 6.5. (a) Adhesion map of silicon at room temperature after a complete heating-cooling cycle corresponding to image figure 5 (e). In the marked area (white frame) the AFM-tip removed the SLB material on top of the SiO2/Si substrate. (b) Histogram of the white rectangle shown in the adhesion map that represents the substrate, silicon. The main adhesion peak of silicon is around 5 nN.

6.4 Complete set of AFM images during the temperature ramp

The complete AFM temperature ramp applied to the sample, associated with the images showed in the figure 4.32 d) and e), can be observed in the figure 6.6. All images shown in figure 6.6 are taken in the same scan zone. With these topography images it is possible to observe the tip effect during the temperature cycle when the temperature rises above the Liquid Disordered phase. The constant movement of the AFM tip produces the effect of material drag in the scan zone that cannot be observed in the contiguous region (see figure 4.32 f))

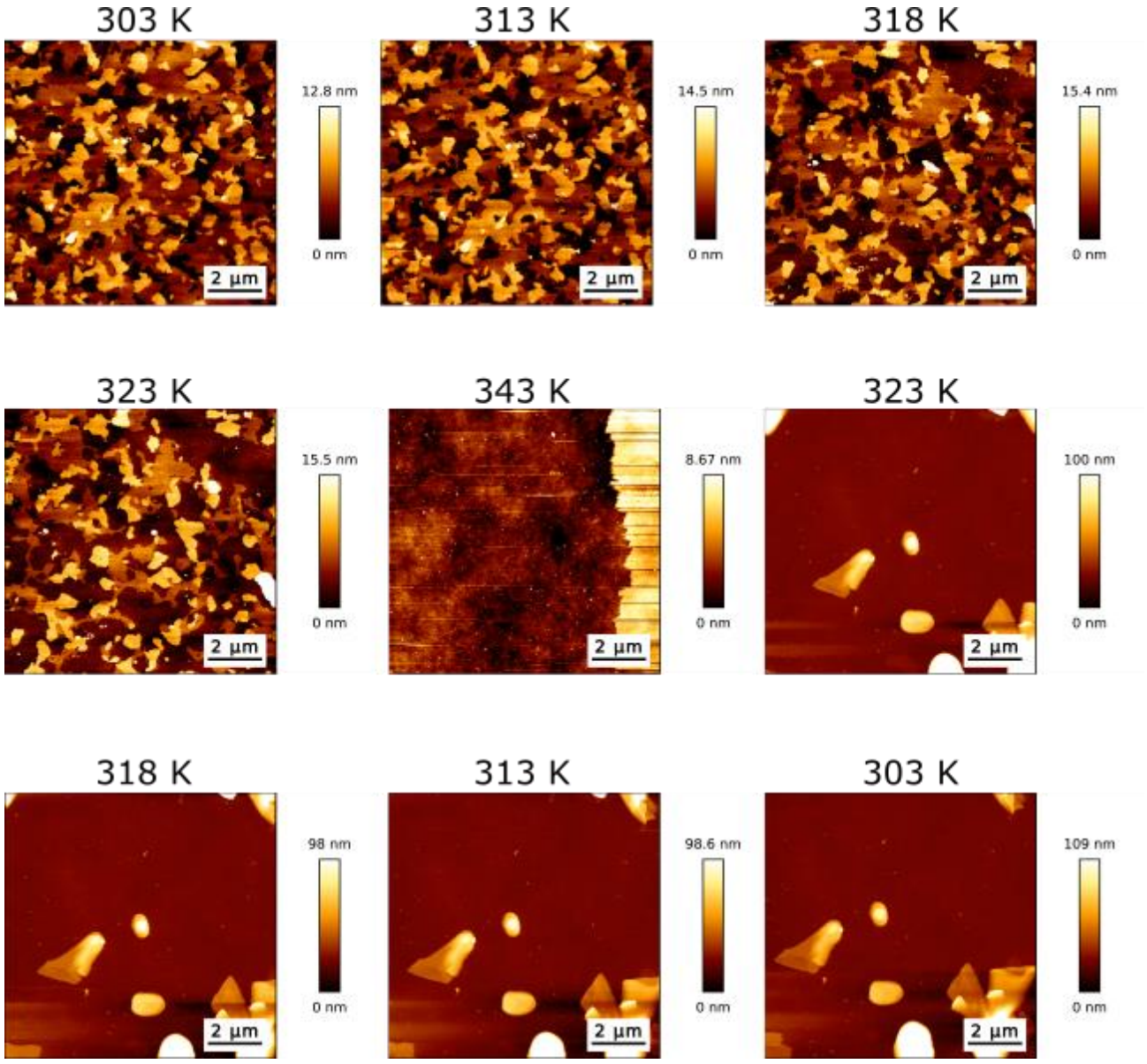

Figure 6.6: Topographical AFM images of DPPC bilayer during the heating-cooling temperature cycle. At 343 K the SLB is in the fluid disordered phase and the AFM cantilever accumulates material at the right side of the image.

6.5 Study of the bilayer surface area

The determination of the decreasing area reported in figure 4.33 was analyzed with the Gwyddion software in order to measure the grain threshold with the aim of obtaining information about the surface area coverage of the DPPC bilayer and its corresponding volume occupied. An example of this process is observed in the figure 6.7. With this technique, it was possible to quantify the surface area covered by the specific bilayer and measuring its reduction due to the drag of material effect produced by the AFM tip.

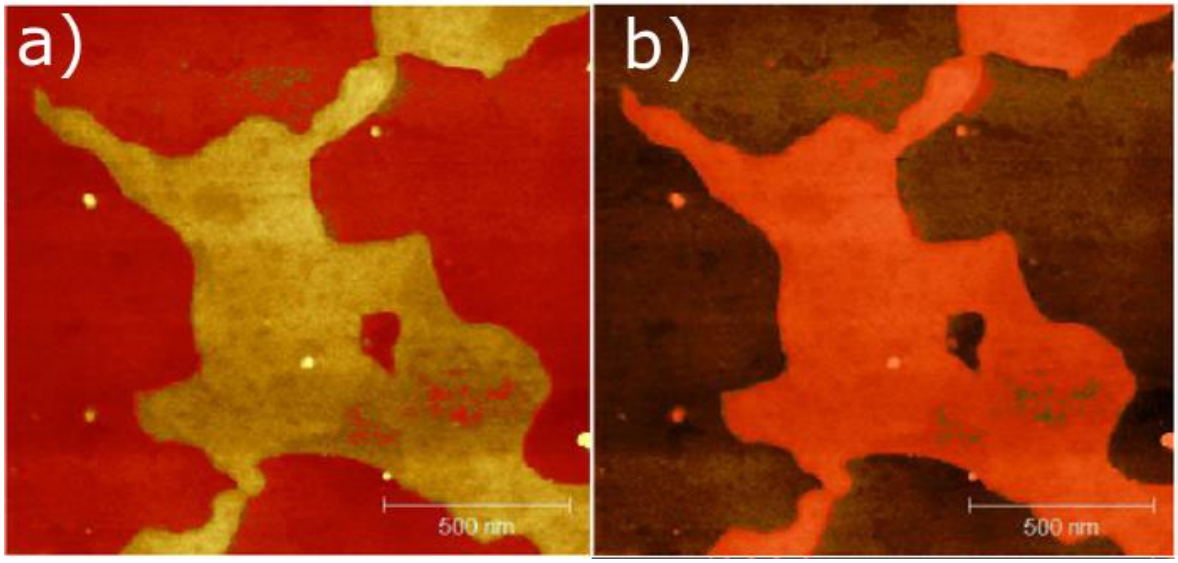

Figure 6.7: a) image of the masked red area called zone 1, which corresponds to the level 1 or the first DPPC bilayer on the silicon substrate and b) image that shows the red masked zone 2 that correspond to the second bilayer on the first bilayer.

Figure 6.8 shows in detailed the holes seen in the SLBs in figure 4.33, which were measured by taking cross-sections that have a depth of ~1.2 nm.

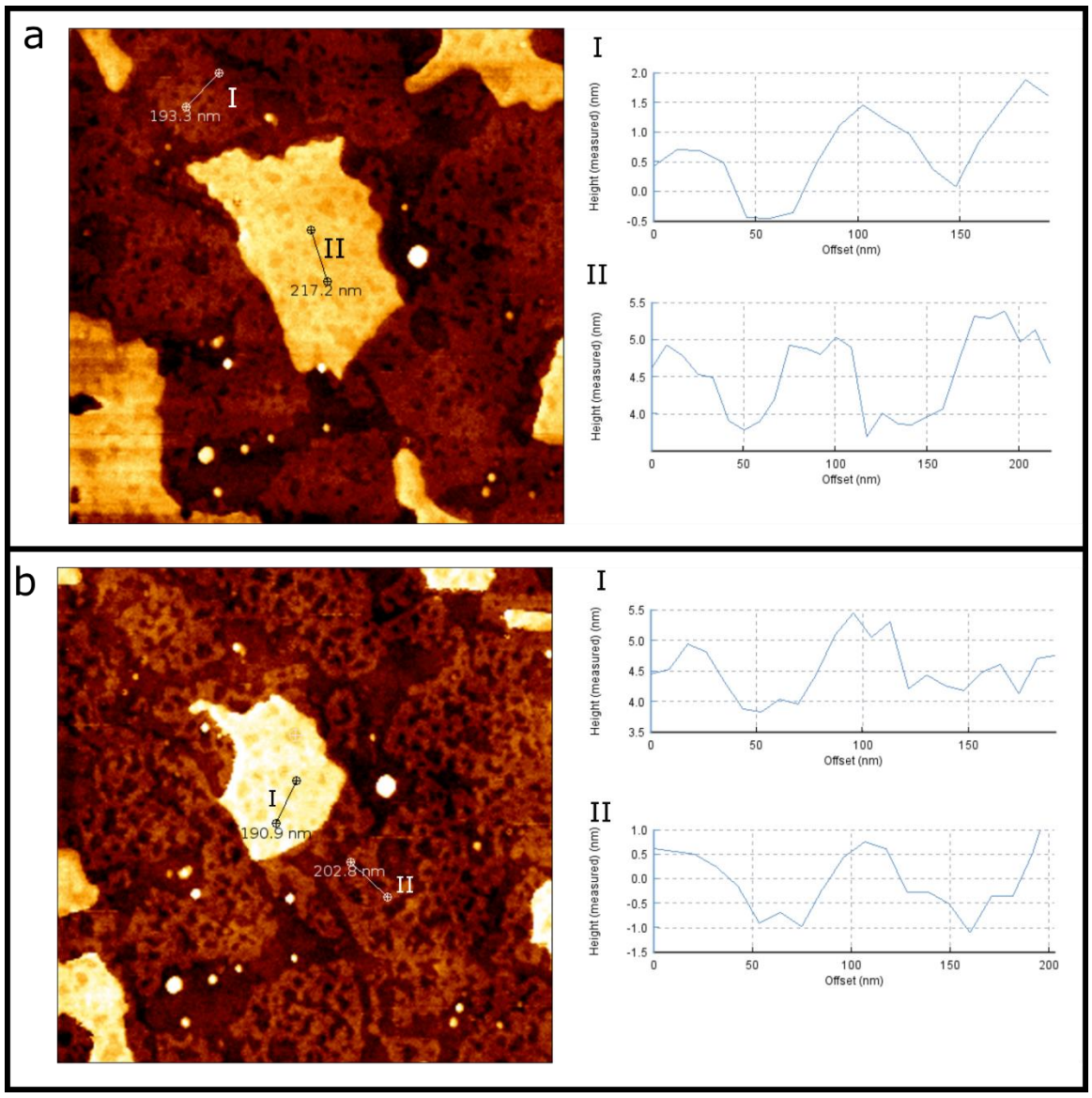

Figure 6.8. Topographical image and cross section of the image corresponding to (a) figure 4.25*c) and (b)* figure 4.25f*).*

6.6 Study of the long term stability of the SLBs formed in Surflab UC

The study of the stability of the SLBs formed in our laboratory was realized comparing the same sample with a difference of 15 months that can be observed in figure 6.9.

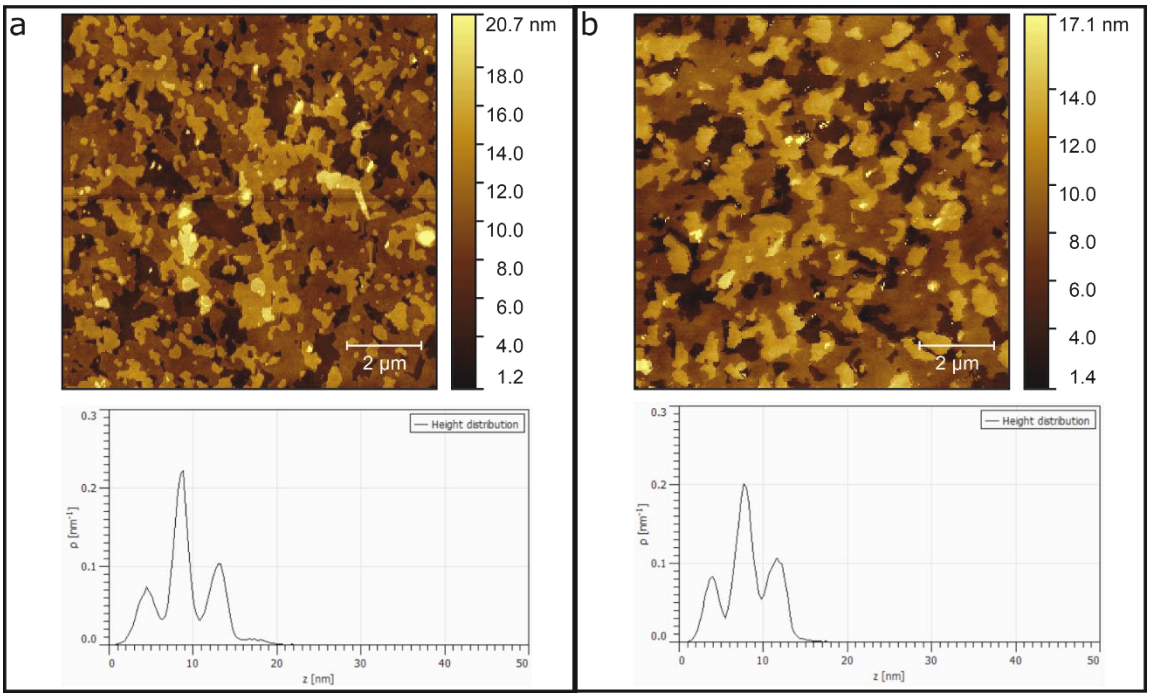

Figure 6.9. AFM images and histograms of (a) DPPC on SiO_2/Si two hours after evaporation and (b) nine months later. The images were taken on the same sample at different areas. The sample was stored in air inside a Petri dish in the laboratory.

6.7 Calibration process of the temperature sensor of the ellipsometer

During the process of the temperature cycle, the temperature controller was used to change and measure *in situ* the temperature of the sample. This sensor is a Pt-100 probe located in a cooper block inside the temperature controller. To study phase transitions in SLBs, it was necessary to measure the temperature directly on the sample (on the silicon surface). Due to the implementation of a suited system to measure the temperature on the sample, which does not interfere with the laser optical path worked out, being somewhat complex, an alternative solution to this problem (that permits us even to recalibrate measurements realized previously) was an extra probe (thermocouple K type) placed on the substrate which was calibrated to the known response measured on the surface of the bilayer.

The result obtained for this calibration process is shown in the figure 6.10 and figure 6.11 corresponding to the curve adjusted during heating and the cooling parts of the temperature cycle. In both calibration curves, the slopes are similar but still considered separate in order to produce a more accurate result.

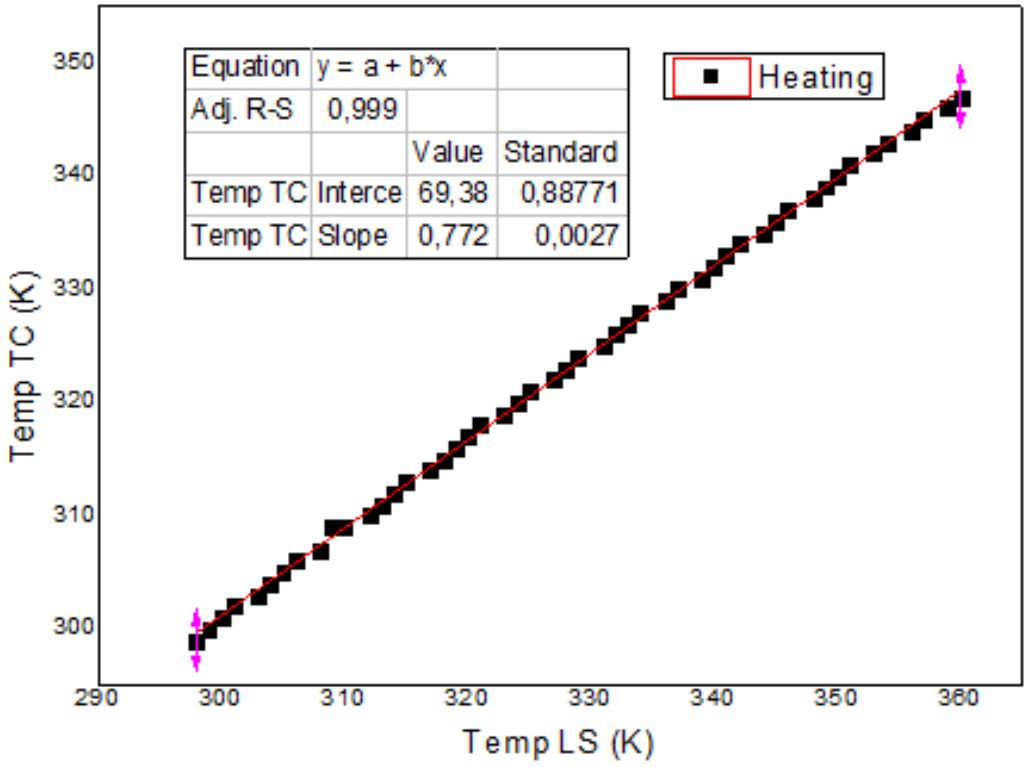

Figure 6.10: Calibration curve during the heating process that compare the temperature measured with the thermocouple (Temp TC) and the temperature measured with the Pt-100 probe of the lakeshore temperature controller (Temp LS).

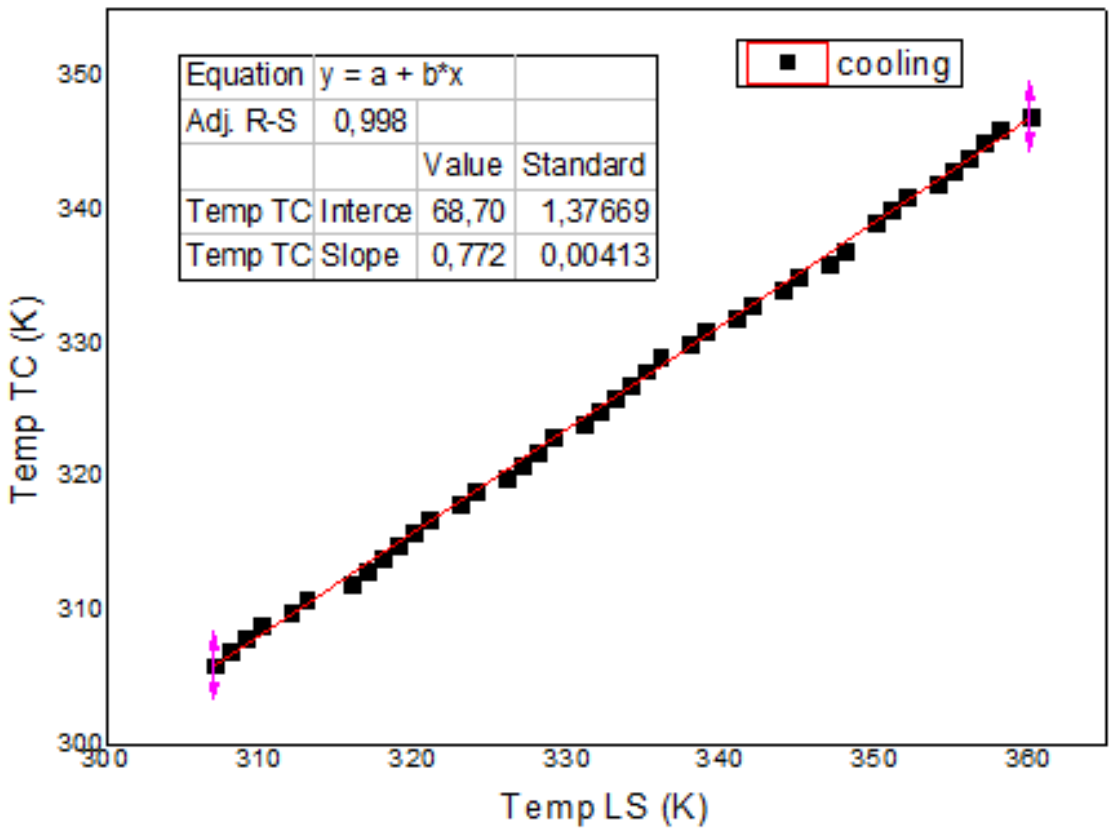

Figure 6.11: Calibration curve during the cooling process that compare the temperature measured with the thermocouple (Temp TC) and the temperature measured with the Pt-100 probe of the lakeshore temperature controller (Temp LS).

6.8 Analysis of the Straylight Intensity (SLI) results

A useful tool to observe phase transitions in thin films is to measure the straylight emitted from the sample surface. Results obtained from these measurements are shown in figure 6.12 to figure 6.21. Figure 6.12 represents the first temperature cycle from room Temperature to 360 K. In this curve one can observe the change from the unstable initial state of the bilayers, after the evaporation process, to the stable state of the DPPC SLB. Figures 6.13 to figure 6.15 show the following temperature cycles realized to the sample NE01 that were performed upon the same area of the sample (the sample was not moved in the holder during the four first temperature cycles). Figure 6.13 and figure 6.14 show the complete temperature cycles for the stable state of the SLB. Figure 6.15 shows only the heating part of the curve to make the analysis easier to read. In this figure it was possible to conclude that the straylight shows a similar information as ΔP, but if we observe the figure 6.15, the straylight intensity changes its shape and this situation makes the analysis confusing, because for ΔP the intensity does not change.

In figure 6.16 it was possible to observe the complete thermal cycle in the sample NE01, but this measurement was realized in a different region of the sample. This temperature cycle shows that both delta P and the straylight change in shape in comparison with the second and third thermal cycles and that suggested that the shape of both delta 6.18 show a complete temperature ramp both in the same region of the results showed in figure 6.16. In this case both delta P and straylight maintain their shapes during at least three thermal cycles.

In figure 6.20 and figure 6.21 it was possible to observe two measurements realized to samples with thicknesses below 30 Å, for which it was not possible to observe (as expected) changes in the ΔP signal, but in the case of straylight for figure 6.20 it was not possible to observe anything; for figure 6.21 it was possible to observe a slight step that could be misinterpreted as a possible phase transition. Still, alongside analyzing the potential repeatability of such ambiguous results with respect to varying

straylight effects, a more detailed study to better understand the behavior of the straylight and its effect upon the ellipsometric results for the SLBs may be necessary.

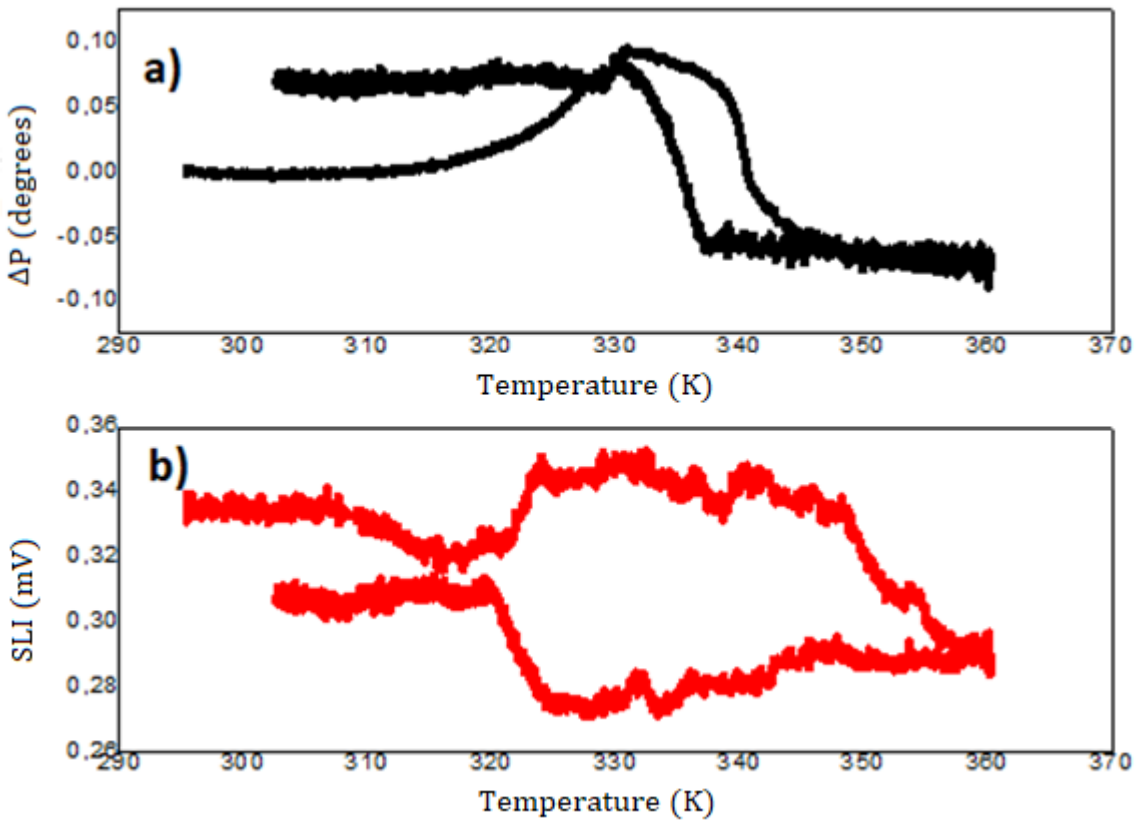

Figure 6.12: a) Changes in the polarization state ΔP of the thin film measured using VHRE and b) Straylight intensity of the thin film measured during the temperature cycle. The sample shown is NE01 thermal cycle number 1.

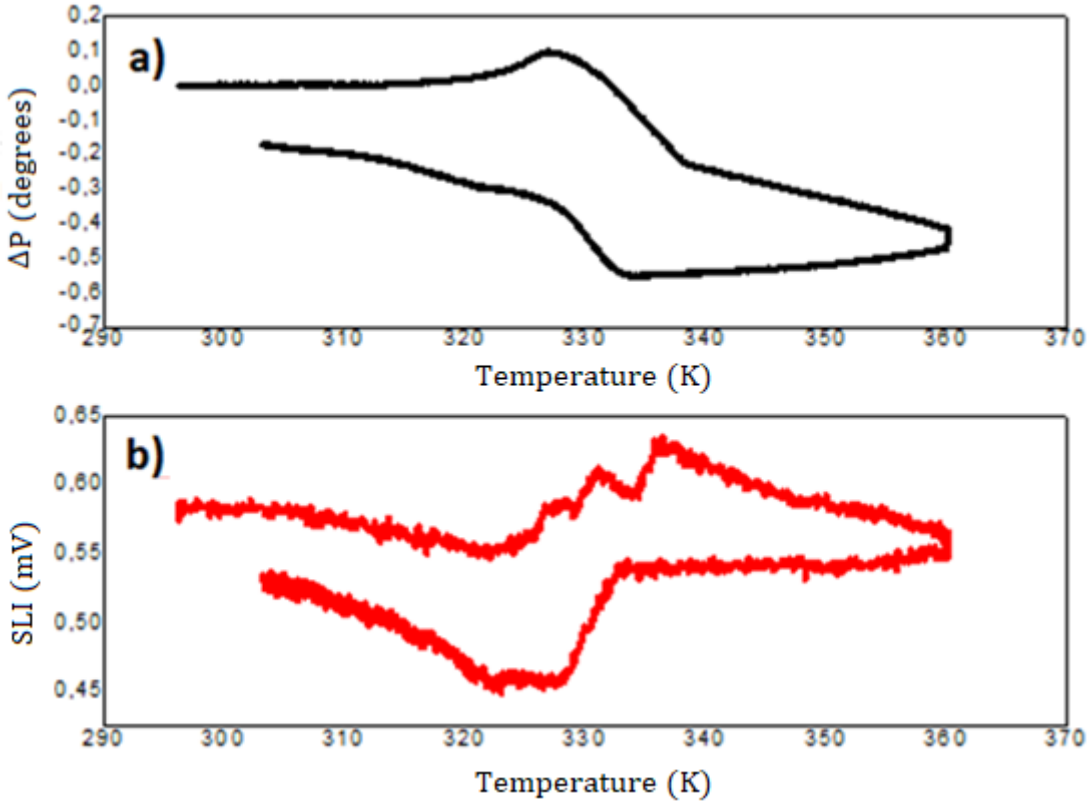

Figure 6.13: a) Changes in the polarization state ΔP of the thin film measured using VHRE and b) Straylight intensity of the thin film measured during the temperature cycle. The sample shown is NE01 thermal cycle number 2.

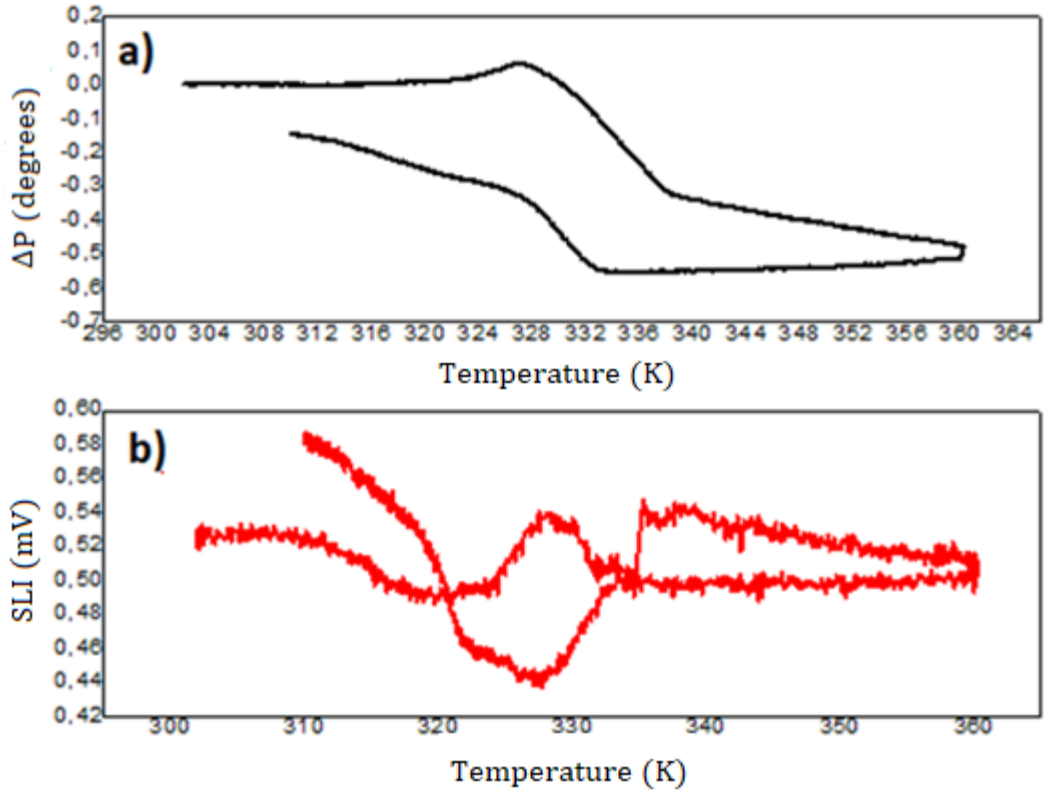

Figure 6.14: a) Changes in the polarization state ΔP of the thin film measured using VHRE and b) Straylight intensity of the thin film measured during the temperature cycle. The sample shown is NE01 thermal cycle number 3.

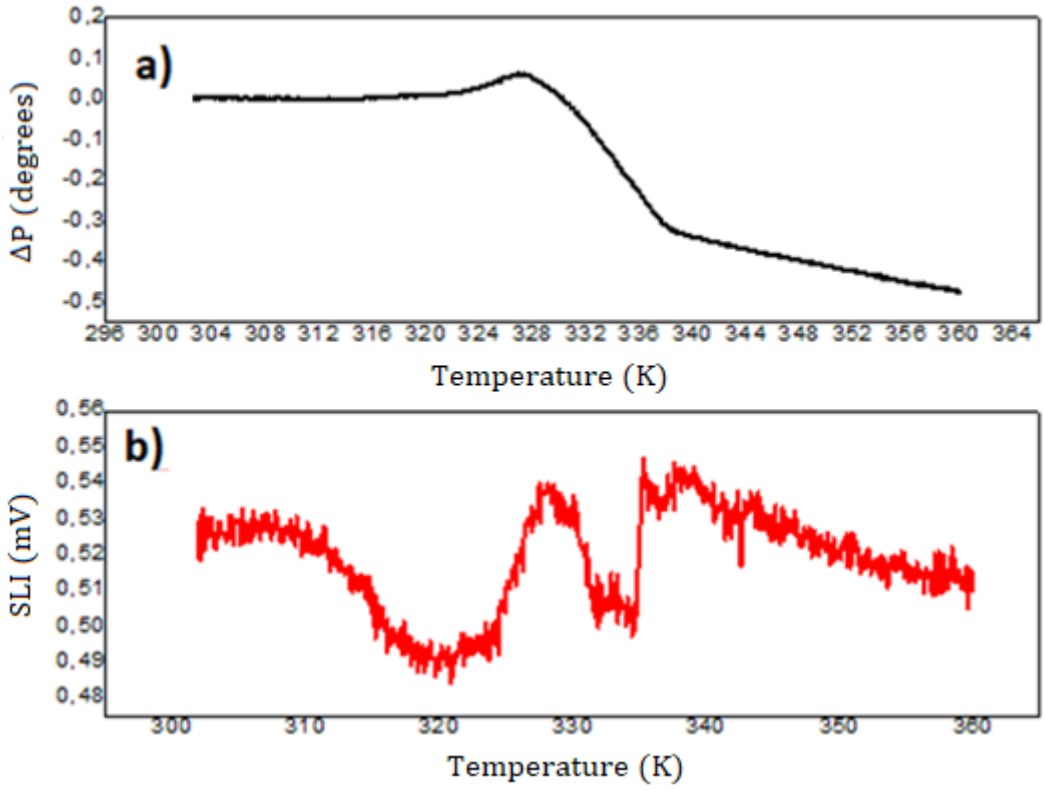

Figure 6.15: a) Changes in the polarization state ΔP of the thin film measured using VHRE and b) Straylight intensity of the thin film measured during the temperature cycle. The sample shown is NE01 heating ramp number 3.

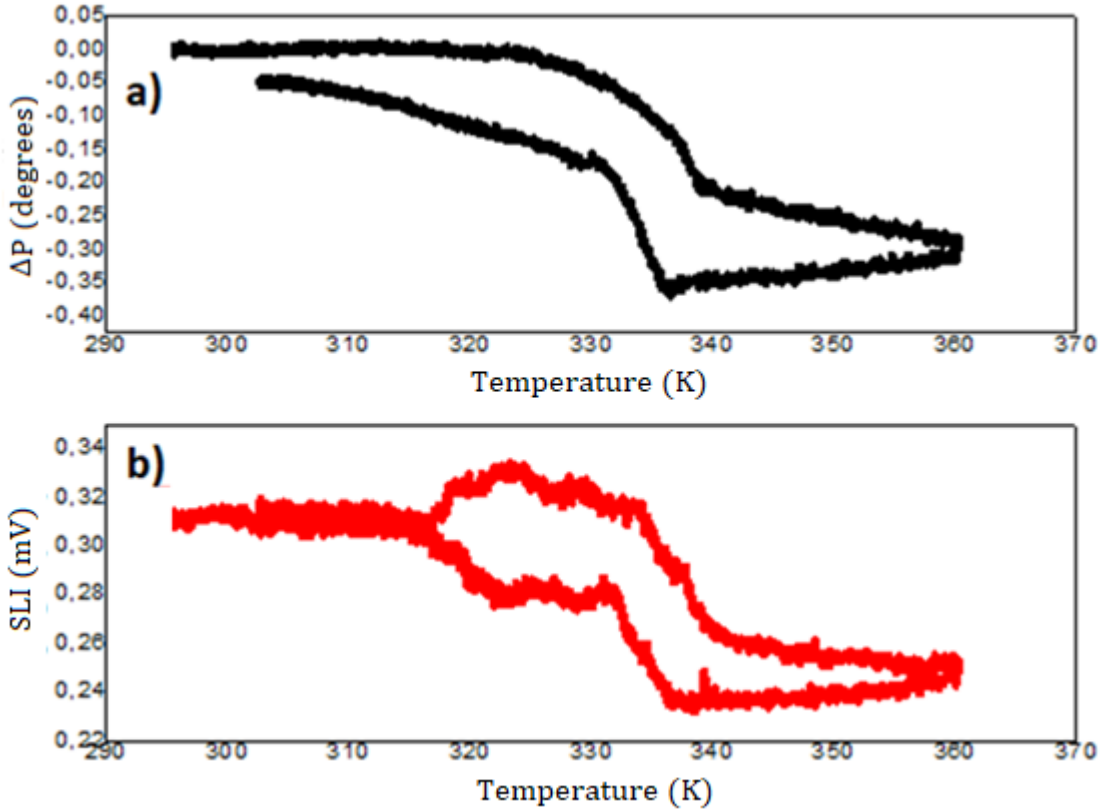

Figure 6.16: a) Changes in the polarization state ΔP of the thin film measured using VHRE and b) Straylight intensity of the thin film measured during the temperature cycle. The sample shown is NE01 thermal cycle number 5.

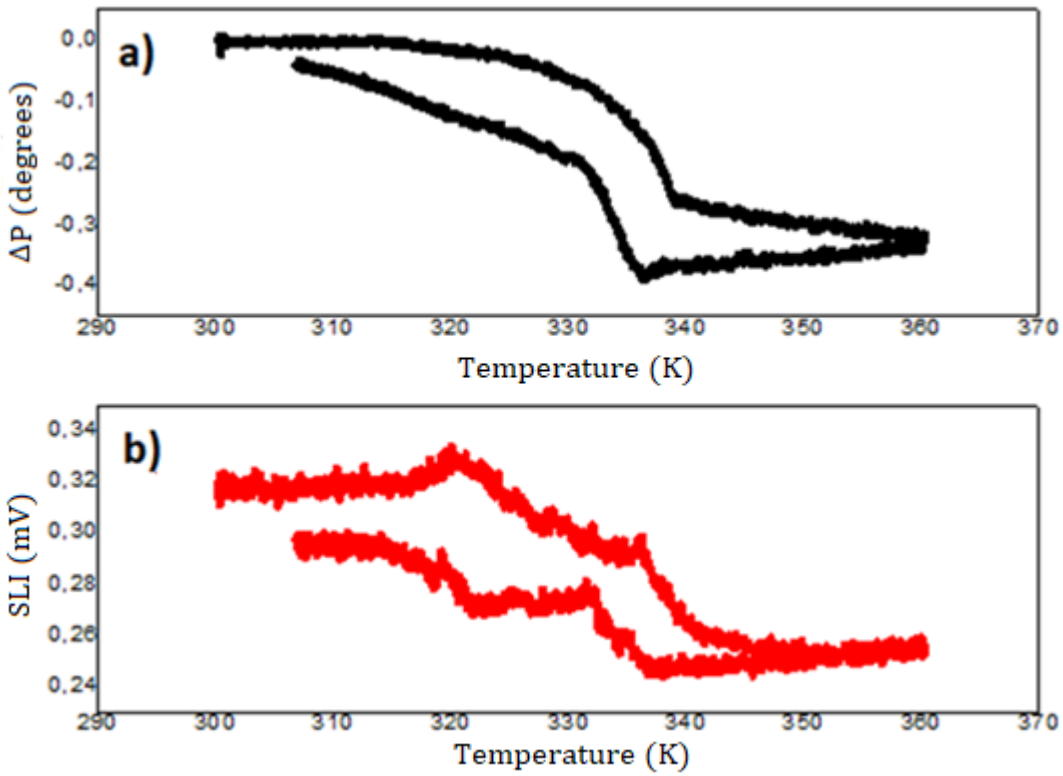

Figure 6.17: a) Changes in the polarization state ΔP of the thin film measured using VHRE and b) Straylight intensity of the thin film measured during the temperature cycle. The sample shown is NE01 thermal cycle number 6.

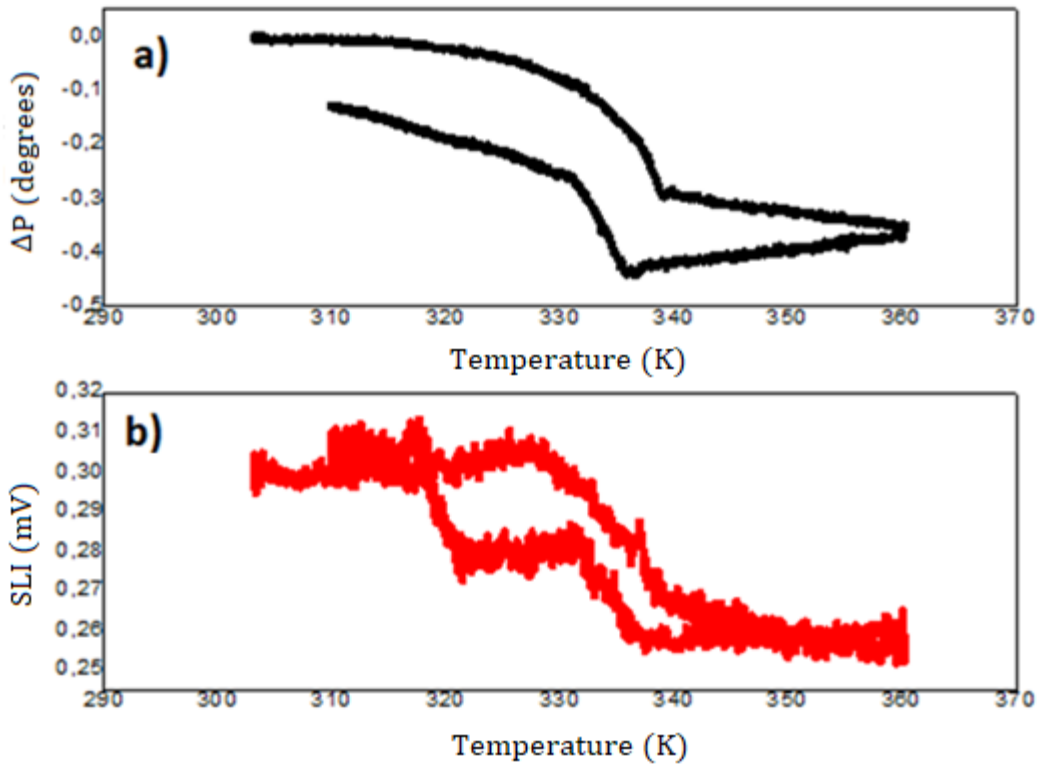

Figure 6.18: a) Changes in the polarization state ΔP of the thin film measured using VHRE and b) Straylight intensity of the thin film measured during the temperature cycle. The sample shown is NE01 thermal cycle number 7.

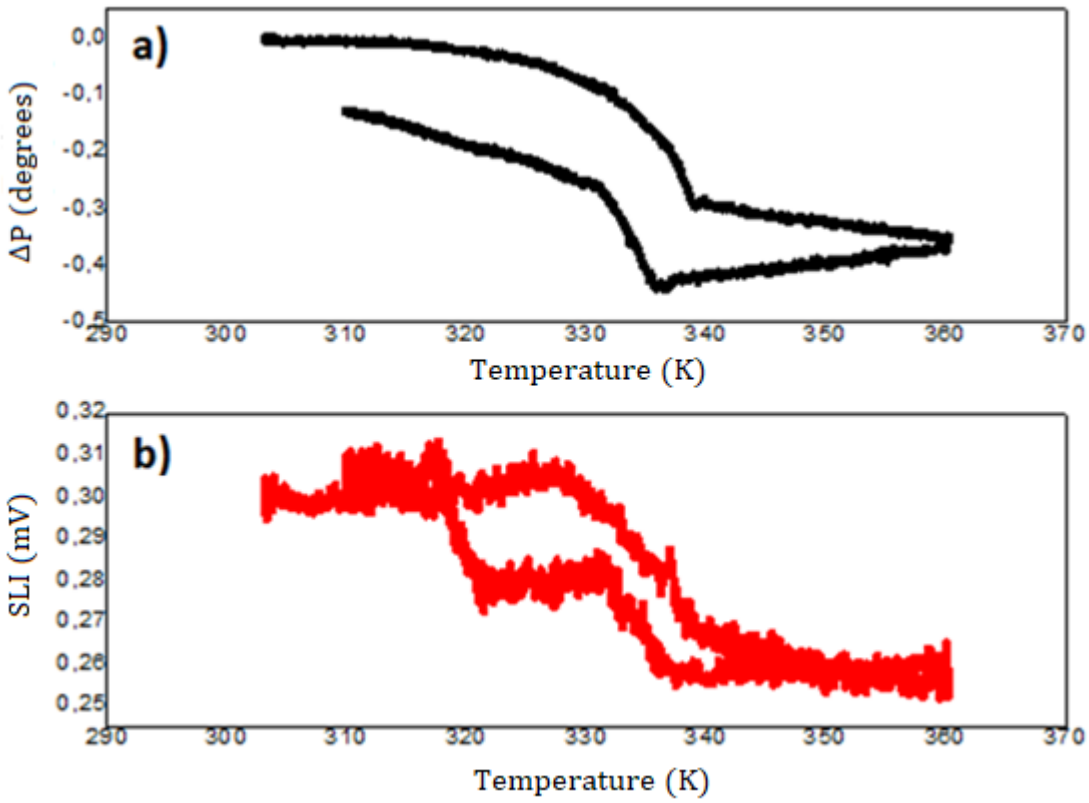

Figure 6.19: a) Changes in the polarization state ΔP of the thin film measured using VHRE and b) Straylight intensity of the thin film measured during the temperature cycle. The sample shown is NE01 thermal cycle number 8.

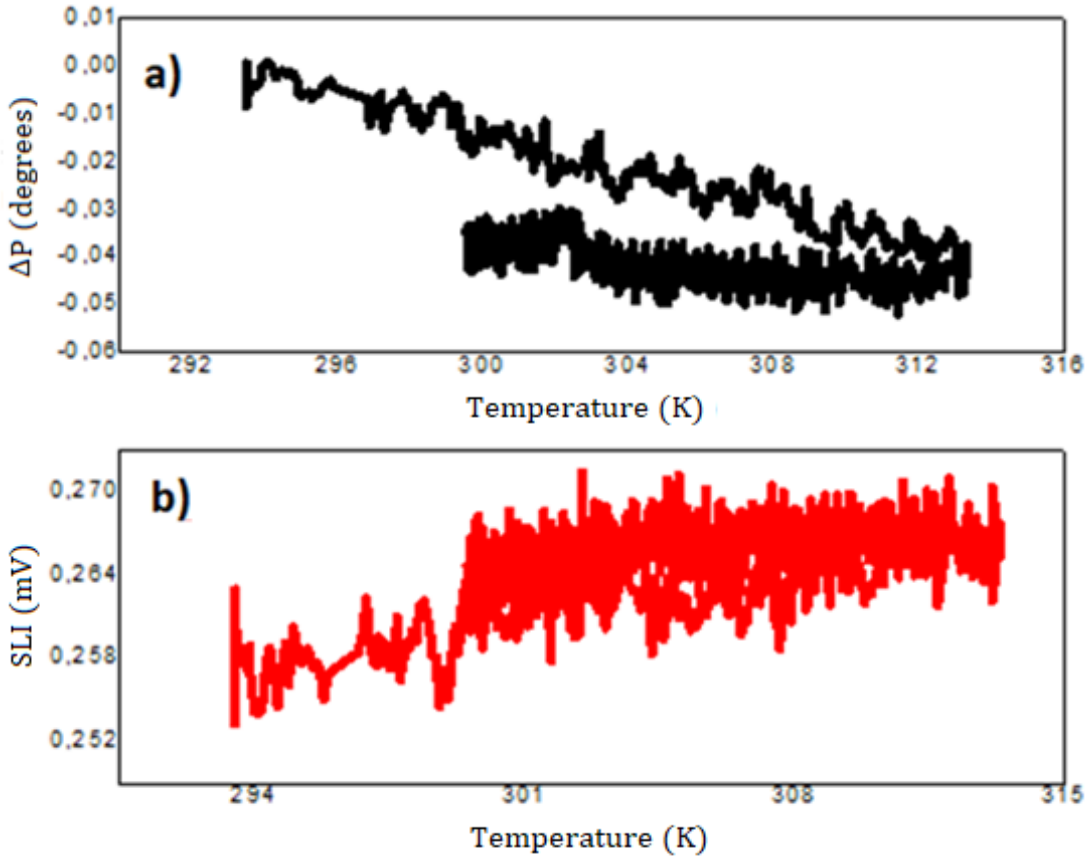

Figure 6.20: a) Changes in the polarization state ΔP of the thin film measured using VHRE and b) Straylight intensity of the thin film measured during the temperature cycle. The sample shown is NE17 ramp number 6.

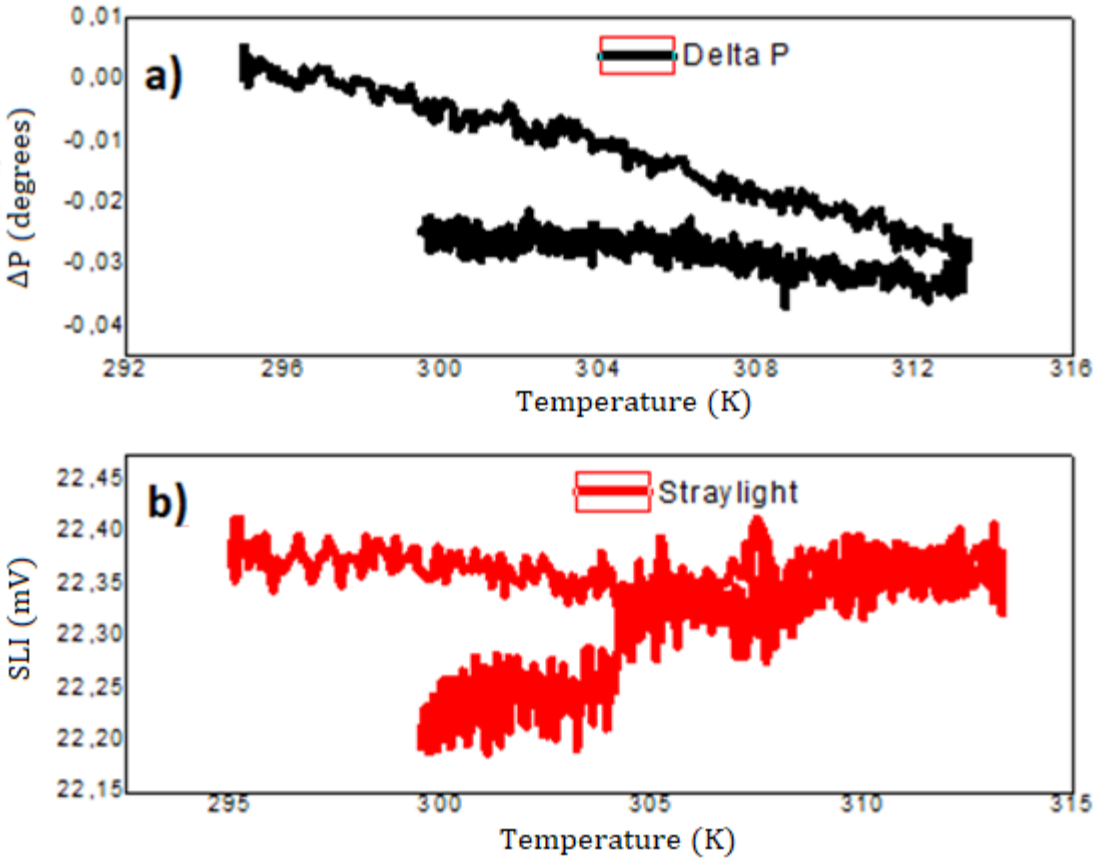

Figure 6.21: a) Changes in the polarization state ΔP of the thin film measured using VHRE and b) Straylight intensity of the thin film measured during the temperature cycle. The sample shown is NE17 ramp number 8.

6.9 Postulated Projects, conferences and publications

6.9.1 Postulated Projects

1. 15° Concurso Nacional de Proyectos I+D+i Copec-UC, 2017. (Finalists)

2. CONCURSO NACIONAL DE PROYECTOS IV Concurso IDeA en Dos Etapas Convocatoria 2017.

3. Concurso Covid-19 ANID 2020.

6.9.2 International Conferences

1. Sebastian Molina, **Marcelo Cisternas**, Maria J. Retamal, Nicolas Moraga, Hugo Zelada, Jonas Fortmann, Tomas P. Corrales, Patrick Huber, Marco Soto-Arriaza and Ulrich G. Volkmann. **"Soft Thermal Treatment Stabilizes Vacuum-deposited Phospholipid Layers for Sensor Applications"** DPG Spring Meeting, March 31-April 05, 2019, Regensburg, Germany.

2. **Marcelo Andres Cisternas**, Sebastian D. Molina, Maria Jose Retamal, Nicolas H. Moraga, Hugo I. Zelada, Tomas P. Corrales, Diego I. Diaz, Rodrigo S. Catalan and Ulrich G. Volkmann. **"Study of the Behavior of an Artificial Membrane Immersed in Aqueous Medium"**. 2018 MRS Fall Meeting & Exhibit, November 25-30, 2018, Boston, Massachusetts, USA.

3. Nicolas Moraga, **Marcelo Cisternas**, Diego Diaz, Rodrigo Catalan, Maria J. Retamal, Tomas P. Corrales, Mark Busch, Patrick Huber, Marco Soto-Arriaza, and Ulrich G. Volkmann. **"Formation and phase transitions of vapour deposited phospholipid bilayers on porous silicon substrates"** DPG March Meeting, March 11-16, 2018, Berlin, Germany.

4. MJ Retamal, R Catalan, **M Cisternas**, N Moraga, D Diaz, TP Corrales, M Busch, P Huber, M Soto-Arriaza, and UG Volkmann. **"Study of elastic modulus of phospholipid bilayers"** DPG March Meeting, March 11-16, 2018, Berlin, Germany.

5. Diego Diaz, Robert Wheatley, Martín Roble, **Marcelo Cisternas**, Donovan Diaz, Ulrich G. Volkmann, Alejandro Cabrera, Birger Seifert, and Sascha Wallentowitz. **"Wetting properties of CuFeO2 delafossite for photo-catalytic processes"** DPG March Meeting, March 11-16, 2018, Berlin, Germany.

6. Diego Diaz, Tomas P. Corrales, Maria J. Retamal, **Marcelo Cisternas**, Nicolas Moraga, Rodrigo Catalan, Mark Busch, Patrick Huber, Marco Soto-Arriaza, and

Ulrich G. Volkmann. **"Rearrangement of nanopatterns: Wetting of n-alkane Molecular Films"** DPG March Meeting, March 11-16, 2018, Berlin, Germany.

7. **Marcelo A. Cisternas**, Nicolas Moraga, Rodrigo Catalan, Maria Jose Retamal, Diego Diaz, Tomas P. Corrales, Tomas Perez-Acle, Marcos Soto-Arriaza, Patrick Huber, Birger Seifert and Ulrich G. Volkmann. **"Optimized pore geometry on silicon substrate surface for long time phospholipid cell membrane stability"** American Physical Society (APS) March Meeting, March 5-9, 2018, Los Angeles, California, USA.

8. Ulrich G. Volkmann, Rodrigo Catalan, Maria Jose Retamal, **Marcelo A. Cisternas**, Nicolas Moraga, Diego Diaz, Tomas P. Corrales, Marcos Soto-Arriaza and Patrick Huber. **"Atomic force microscopt (AFM) study of elastic modulus of artificial phospholipid membranes"** American Physical Society (APS) March Meeting, March 5-9, 2018, Los Angeles, California, USA.

9. **Marcelo A. Cisternas**, Maria Jose Retamal, Partha Saikia, Nathalie Casanova, Nicolas Moraga, America Chandia, Alejandra Alvarez, Donovan E. Diaz-Droguett, Fernando Guzman, Stephan Mändl, Darina Manova, Tomas P. Corrales, Ulrich G. Volkmann, Mario Favre and Heman Bhuyan. **"Study of phospholipid bilayer supported on chitosan-titanium nitride coatings produced by plasma immersion ion implantation (PIII)"** 62nd Annual Meeting Biophysical Society (BPS 2018) 17-21 February, San Francisco, California, USA.

10. Ulrich G. Volkmann, Rodrigo Catalan, Maria Jose Retamal, **Marcelo A. Cisternas**, Nicolas Moraga, Diego Diaz, Tomas P. Corrales, Tomas Perez-Acle, Marcos Soto-Arriaza and Patrick Huber. **"AFM study of elastic module of physical-vapor-deposited phospholipid membranes"** 62nd Annual Meeting Biophysical Society (BPS 2018) 17-21 February, San Francisco, California, USA.

11. Tomas P. Corrales, Diego Diaz, Rodrigo Catalan, Maria Jose Retamal, **Marcelo Cisternas**, Nicolas Moraga, Marcos Soto-Arriaza and Ulrich G. Volkmann. **"Formation and morphology of singles phospholipid bilayers formed my velocity-controlled dip-coating"** 62nd Annual Meeting Biophysical Society (BPS 2018) 17-21 February, San Francisco, California, USA.

12. Diego Diaz, Tomas P. Corrales, Nicolas Moraga, **Marcelo Cisternas**, Rodrigo Catalan, Maria Jose Retamal, Patrick Huber, Ulrich G. Volkmann. **"The Reverse Coffee-Ring Effect: Wetting of n-alkane Molecular Films"**. 31rst Conference of the European Colloid and Interface Society (ECIS 2017) 3-8 September, Madrid, Spain.

13. Rodrigo Catalan, Maria Jose Retamal, Diego Diaz, **Marcelo Cisternas**, Nicolas Moraga, Tomas P. Corrales, Marco Soto-Arriaza, Patrick Huber, and Ulrich G. Volkmann. **"AFM study of evaporated phospholipidic bilayer on thin film chitosan in liquid environment"**. DPG March Meeting, March 19-24, 2017, Dresden, Germany.

14. **Marcelo Cisternas**, Vanessa Zepeda, Maria Jose Retamal, Tomas P. Corrales, Nicolas Moraga, Diego Diaz, Rodrigo Catalan, Sebastian Gutierrez, Tomas Perez-Acle, Patrick Huber, and Ulrich G. Volkmann, **"Study of the ion channels insertion in artificial membranes"**. DPG March Meeting, March 19-24, 2017, Dresden, Germany.

15. Ulrich G. Volkmann, María J. Retamal, **Marcelo A. Cisternas**, Vanessa Zepeda, Nicolás Moraga, Rodrigo Catalán, Diego Díaz, Tomas P. Corrales, Tomas Pérez-Acle, Sebastián E. Gutiérrez-Maldonado, Marco Soto-Arriaza, Mark Busch, Patrick Huber. **"Vapor-deposited phospholipid membranes on chitosan and porous silicon (psi) for novel lab-on-chip platforms to study membrane-proteins"**. Biophysical Society, 61th Annual Meeting, February 11-15, 2017 - New Orleans - Louisiana -USA.

16. H. Bhuyan, M. Favre, **M. Cisternas**, A. Henríquez, E. Wyndham, S. Mandl, D. Manova and M. Walczak. **"Nitriding of Super-Ferritic Stainless Steel by Plasma Immersion Ion Implantation in Radio Frequency and ECR Microwave Plasma System"**. The 42nd IEEE International Conference on Plasma Physics (ICOPS 2015), Belek, Antalya, Turkey.

6.9.3 National Conferences

1. **M. Cisternas**, S. Molina, M.J. Retamal, N. Moraga, H. Zelada, R. Catalán, D. Diaz, T. Corrales y U.G. Volkmann. **"Estudio elipsométrico de una membrana fosfolipídica sumergida en un medio acuoso"**. XXI Simposio Chileno de Física, 14-16 Noviembre 2018, Antofagasta, Chile.

2. N. Moraga, **M. Cisternas**, M. J. Retamal, D. Díaz, R. Catalán, T. Corrales, S. Molina, H. Zelada y U. G. Volkmann. **"Formación y detección de bicapas lípidicas de DPPC depositadas desde la fase de vapor sobre sustratos de silicio poroso"**. XXI Simposio Chileno de Física, 14-16 Noviembre 2018, Antofagasta, Chile.

3. R. Catalán, M.J. Retamal, N. Moraga, **M. Cisternas**, S. Molina, H. Zelada, T. Corrales, M. Soto-Arriaza, U.G. Volkmann. **"Estudio de propiedades el´asticas de**

bicapas fosfolipídicas evaporadas". XXI Simposio Chileno de Física, 14-16 Noviembre 2018, Antofagasta, Chile.

4. **M. Cisternas**, S. Molina, M. J. Retamal, T. Corrales, N. Moraga, D. Diaz, R. Catalán y U. G. Volkmann. **"Estudio del comportamiento de una membrana artificial en un medio acuoso"**. V Congreso Nacional de Nanotecnología, 25-29 Noviembre 2018, Pucón, Chile.

5. M. Cisternas, V. Zepeda, M. J. Retamal, T. Corrales, N. Moraga, D. Diaz, R. Catalán, S. Gutierrez, T. Perez-Acle y U. G. Volkmann: **"ESTUDIO DE LA INSERCIÓN DE CANALES IÓNICOS EN MEMBRANAS ARTIFICIALES"**. XX Simposio Chileno de Física (SOCHIFI), 30 de Noviembre, 1 y 2 de Diciembre 2016, Casa Central UTEM, Santiago, Chile.

6. María José Retamal, Tomás Corrales, Marcelo Cisternas, Nicolás Moraga, Rodrigo Catalán, Diego Díaz, Marco Soto-Arriaza, Ulrich G. Volkmann. **"EVAPORACIÓN DE PELÍCULAS DE QUITOSANO: EVIDENCIA DE "SOLID-STATE DEWETING"** en biopolímeros". XX Simposio Chileno de Física, 30 de Noviembre, 1 y 2 de Diciembre, 2016, Santiago, Chile.

7. Nicolás Moraga, Rodrigo Catalán, Marcelo Cisternas, María José Retamal, Diego Díaz, Tomas P. Corrales, Ulrich G. Volkmann. **"Diseño e implementación de una celda electroquímica para la fabricación de silicio poroso (pSi): Caracterización y optimización"**. XX Simposio Chileno de Física, 30 de Noviembre, 1 y 2 de Diciembre, 2016, Santiago, Chile.

8. Rodrigo Catalán, María José Retamal, Diego Díaz, Marcelo Cisternas, Nicolás Moraga, Tomás Corrales, Marco Soto-Arriaza, Ulrich G. Volkmann. **"Estudio térmico y morfológico de fosfolípidos mediante microscopía de fuerza atómica en ambiente acuoso"**. XX Simposio Chileno de Física, 30 de Noviembre, 1 y 2 de Diciembre, 2016, Santiago, Chile.

9. Diego I. Díaz, Tomás P. Corrales, Ulrich G. Volkmann, María José Retamal, Marcelo Cisternas, Nicolás Moraga, Rodrigo Catalán. **"Estudio de mojabilidad de monocapas de n-alcanos"**. XX Simposio Chileno de Física, 30 de Noviembre, 1 y 2 de Diciembre, 2016, Santiago, Chile.

10. Ulrich G. Volkmann, Héctor Jorquera, María José Retamal, Marco Soto, Marcelo Cisternas, Nicolás Moraga, Diego Díaz, Rodrigo Catalán, Tomás Corrales. **"Nanopartículas provenientes de procesos de combustión y su impacto en el medio ambiente"**. XX Simposio Chileno de Física, 30 de Noviembre, 1 y 2 de Diciembre, 2016, Santiago, Chile.

11. Marcelo Cisternas, Vanessa Zepeda, María José Retamal, Tomás Corrales, Nicolás Moraga, Diego Diaz, Rodrigo Catalán, Sebastián Gutierrez, Tomás Perez-Acle y Ulrich G. Volkmann: **"ESTUDIO DE LA INSERCIÓN DE CANALES IÓNICOS**

EN MEMBRANAS ARTIFICIALES". 12° Seminario Internacional de Fundación Copec-UC, 15 de Noviembre de 2016, Casa Central UC, Santiago, Chile.

12. M. Cisternas, A. Henríquez, H. Bhuyan, M.J. Retamal, N. Casanova, A. Chandía, A. Alvarez, S. Mändl, D. Manova, F. Guzmán, N. Moraga, M. Favre, and U. G. Volkmann: **"Formation and characterization of TiN coatings over Ti, using Plasma Immersion Ion Implantation (PIII), aiming to applications in artificial membranes"**. 2 Workshop de Biofísica, 30 de Septiembre a 2 de Octubre 2015, Hotel Gala, Viña del Mar, Valparaíso, Chile.

13. A. Henriquez, N. Soto, H. Bhuyan, M. Favre, J. R. Maze, V. Waselowski, R. Gonzalez, J. Armijo, M. Cisternas, E. Wyndham: **"Observation of posible changes in the fluorescence spectrum of NV centers due to electron irradiation"**. 2 Workshop de Biofísica, 30 de Septiembre a 2 de Octubre 2015, Hotel Gala, Viña del Mar, Valparaíso, Chile.

6.9.4 Publications

1. Marcelo A. Cisternas, Francisca Palacios-Coddou, Sebastian Molina, Maria Jose Retamal, Nancy Gomez-Vierling, Nicolas Moraga, Hugo Zelada, Marco A. Soto-Arriaza, Tomas P. Corrales and Ulrich G. Volkmann. **"Dry Two-Step Self-Assembly of Stable Supported Lipid Bilayers on Silicon Substrates"**, Int. J. Mol. Sci. **21(18)**, (2020) 6819; DOI: 10.3390/ijms21186819. This publication was included in the Encyclopedia from MDPI under the Category: Biomaterials, Surfaces, Coatings & Films and Condensed Matter Physics. Title: **Lipid Bilayers on Silicon Substrates.** https://encyclopedia.pub/3619

2. M. Cisternas, H. Bhuyan, M.J. Retamal, N. Casanova-Morales, M. Favre, U.G. Volkmann, P. Saikia, D.E. Diaz-Droguett, S. Mändl, D. Manova, N. Moraga, A. Chandía-Cristi, A. Alvarez, F. Guzman. **"Study of nitrogen implantation in Ti surface using plasma immersion ion implantation & deposition technique as biocompatible substrate for artificial membranes"**, Materials Science & Engineering C **113** (2020) 111002. DOI: 10.1016/j.msec.2020.111002

3. Sebastian E. Gutierrez-Maldonado, Jose Antonio Garate, Maria Jose Retamal, Marcelo A. Cisternas, Ulrich G. Volkmann, Tomas Perez-Acle. **"Accessing the Structural and Thermodynamic Properties of Ultra-thin Layers of C32 Adsorbed on a SiO_2 surface"**, Chemical Physics Letters **674**, 64-70 (2017). DOI: 10.1016/j.cplett.2017.01.065.

4. Maria Jose Retamal, Tomas P. Corrales, Marcelo A. Cisternas, Nicolas H. Moraga, Diego I. Diaz, Rodrigo E. Catalan, Birger Seifert, Patrick Huber and Ulrich Volkmann. **"Surface Morphology of Vapor-Deposited Chitosan: Evidence of Solid-State Dewetting during the Formation of Biopolymer Films"**, BioMacroMolecules **17**, 1142-1149 (2016). DOI: 10.1021/acs.biomac.5b01750.

7. References:

[1] C. G. Siontorou, G.-P. Nikoleli, D. P. Nikolelis, and S. K. Karapetis, “Artificial Lipid Membranes: Past, Present, and Future.,” *Membranes (Basel).*, vol. 7, no. 3, Jul. 2017.

[2] A. Salehi-Reyhani, O. Ces, and Y. Elani, “Artificial cell mimics as simplified models for the study of cell biology,” *Exp. Biol. Med.*, vol. 242, no. 13, pp. 1309–1317, 2017.

[3] R. Glazier and K. Salaita, “Supported lipid bilayer platforms to probe cell mechanobiology.,” *Biochim. Biophys. acta. Biomembr.*, vol. 1859, no. 9 Part A, pp. 1465–1482, Sep. 2017.

[4] M. J. Retamal *et al.*, “Towards bio-silicon interfaces: Formation of an ultra-thin self-hydrated artificial membrane composed of dipalmitoylphosphatidylcholine (DPPC) and chitosan deposited in high vacuum from the gas-phase,” *J. Chem. Phys.*, vol. 141, no. 10, pp. 104201–7, 2014.

[5] G.-P. Nikoleli, D. Nikolelis, C. G. Siontorou, and S. Karapetis, “Lipid Membrane Nanosensors for Environmental Monitoring: The Art, the Opportunities, and the Challenges.,” *Sensors (Basel).*, vol. 18, no. 1, Jan. 2018.

[6] G.-P. Nikoleli, D. P. Nikolelis, C. G. Siontorou, M.-T. Nikolelis, and S. Karapetis, “The Application of Lipid Membranes in Biosensing.,” *Membranes (Basel).*, vol. 8, no. 4, Nov. 2018.

[7] M. Rother, M. G. Nussbaumer, K. Renggli, and N. Bruns, “Protein cages and synthetic polymers: A fruitful symbiosis for drug delivery applications, bionanotechnology and materials science,” *Chem. Soc. Rev.*, vol. 45, no. 22, pp. 6213–6249, 2016.

[8] M. Ni and S. Zhuo, “Applications of self-assembling ultrashort peptides in bionanotechnology,” *RSC Adv.*, vol. 9, no. 2, pp. 844–852, 2019.

[9] Q. Sun *et al.*, “Functional Silver-Coated Colloidosomes as Targeted Carriers for Small Molecules,” *Langmuir*, vol. 33, no. 15, pp. 3755–3764, 2017.

[10] S. Bhaskar and S. Lim, “Engineering protein nanocages as carriers for biomedical applications,” *NPG Asia Mater.*, vol. 9, no. 4, pp. e371-18, 2017.

[11] G. Elender, M. Kühner, and E. Sackmann, “Functionalisation of Si/SiO2 and glass surfaces with ultrathin dextran films and deposition of lipid bilayers,” *Biosens. Bioelectron.*, vol. 11, no. 6, pp. 565–577, 1996.

[12] E. Sackmann, “Supported Membranes: Scientific and Practical Applications,” *Science*, vol. 271, no. 5245, pp. 43–48, 1996.

[13] L. Schmitt, C. Dietrich, and R. Tampe, “Synthesis and Characterization of Chelator-Lipids for Reversible Immobilization of Engineered Proteins at Self-Assembled Lipid Interfaces,” *J. Am. Chem. Soc.*, vol. 116, no. 19, pp. 8485–8491, Sep. 1994.

[14] K. Albert, X. C. Huang, and H. Y. Hsu, “Bio-templated silica composites for next-generation biomedical applications,” *Adv. Colloid Interface Sci.*, vol. 249, no. 1001, pp. 272–289, 2017.

[15] R. P. Richter, R. Bérat, and A. R. Brisson, “Formation of solid-supported lipid bilayers: An integrated view,” *Langmuir*, vol. 22, no. 8, pp. 3497–3505, 2006.

[16] I. Gözen, P. Dommersnes, I. Czolkos, A. Jesorka, T. Lobovkina, and O. Orwar, “Fractal avalanche ruptures in biological membranes,” *Nat. Mater.*, vol. 9, no. 11, pp. 908–912, 2010.

[17] E. T. Castellana and P. S. Cremer, “Solid supported lipid bilayers: From biophysical studies to sensor design,” *Surf. Sci. Rep.*, vol. 61, no. 10, pp. 429–444, 2006.

[18] H. Pace *et al.*, “Preserved Transmembrane Protein Mobility in Polymer-Supported Lipid Bilayers Derived from Cell Membranes,” *Anal. Chem.*, vol. 87, no. 18, pp. 9194–9203, 2015.

[19] F. Mazur, M. Bally, B. Städler, and R. Chandrawati, “Liposomes and lipid bilayers in biosensors,” *Adv. Colloid Interface Sci.*, vol. 249, no. May, pp. 88–99, 2017.

[20] R. Tero, M. Takizawa, Y. J. Li, M. Yamazaki, and T. Urisu, “Lipid membrane formation by vesicle fusion on silicon dioxide surfaces modified with alkyl self-assembled monolayer islands,” *Langmuir*, vol. 20, no. 18, pp. 7526–7531, 2004.

[21] A. L. Plant, M. Brigham-Burke, E. Petrella, and D. O’Shannessy, “Phospholipid/Alkanethiol Bilayers for Cell-Surface Receptor Studies by Surface Plasmon Resonance,” *Anal. Biochem.*, vol. 226, pp. 342–348, 1995.

[22] S. Lingler, I. Rubinstein, W. Knoll, and A. Offenhäusser, “Fusion of small unilamellar lipid vesicles to alkanethiol and thiolipid self-assembled monolayers on

gold," *Langmuir*, vol. 13, no. 26, pp. 7085–7091, 1997.

[23] J. Andersson and I. Köper, "Tethered and polymer supported bilayer lipid membranes: Structure and function," *Membranes (Basel).*, vol. 6, no. 2, p. 30, 2016.

[24] S. Rebaud, O. Maniti, and A. P. Girard-Egrot, "Tethered bilayer lipid membranes (tBLMs): Interest and applications for biological membrane investigations," *Biochimie*, vol. 107, no. Part A, pp. 135–142, 2014.

[25] K. Sumitomo and A. Oshima, "Liquid-Ordered/Liquid-Crystalline Phase Separation at a Lipid Bilayer Suspended over Microwells," *Langmuir*, vol. 33, no. 46, pp. 13277–13283, 2017.

[26] Z. W. Zhu *et al.*, "Electrochemical impedance spectroscopy and atomic force microscopic studies of electrical and mechanical properties of nano-black lipid membranes and size dependence," *Langmuir*, vol. 28, no. 41, pp. 14739–14746, 2012.

[27] J. Kurniawan, J. F. Ventrici De Souza, A. T. Dang, G. Y. Liu, and T. L. Kuhl, "Preparation and Characterization of Solid-Supported Lipid Bilayers Formed by Langmuir-Blodgett Deposition: A Tutorial," *Langmuir*, vol. 34, no. 51, pp. 15622–15639, 2018.

[28] M. Jurak, R. Mroczka, R. Łopucki, and A. E. Wiącek, "Structure and wettability of heterogeneous monomolecular films of phospholipids with cholesterol or lauryl gallate," *Appl. Surf. Sci.*, vol. 493, pp. 1021–1031, 2019.

[29] A. Ortiz, S. Arciniegas, J. Prat, M. Muñoz-Juncosa, and M. Pujol, "Lipid domains in LB films and giant vesicles to study GBV-C peptides interaction in the context of HIV-1 FP inhibition at membranes," *Colloids Surfaces A Physicochem. Eng. Asp.*, vol. 578, p. 123620, 2019.

[30] T. Maekawa *et al.*, "Molecular diffusion and nano-mechanical properties of multi-phase supported lipid bilayers," *Phys. Chem. Chem. Phys.*, vol. 21, no. 30, pp. 16686–16693, 2019.

[31] Z. V Leonenko, E. Finot, H. Ma, T. E. S. Dahms, and D. T. Cramb, "Investigation of temperature-induced phase transitions in DOPC and DPPC phospholipid bilayers using temperature-controlled scanning force microscopy," *Biophys. J.*, vol. 86, no. 6, pp. 3783–3793, 2004.

[32] S. L. Duncan, I. S. Dalal, and R. G. Larson, “Molecular dynamics simulation of phase transitions in model lung surfactant monolayers,” *Biochim. Biophys. Acta*, vol. 1808, no. 10, pp. 2450–2465, 2011.

[33] S. Mabrey and J. M. Sturtevant, “Investigation of phase transitions of lipids and lipid mixtures by high sensitivity differential scanning calorimetry,” *Proc. Natl. Acad. Sci.*, vol. 73, no. 11, pp. 3862–3866, 1976.

[34] W. A. Petri, T. N. Estep, R. Pal, T. E. Thompson, R. L. Biltonen, and R. R. Wagner, “Thermotropic Behavior of Dipalmitoylphosphatidylcholine Vesicles Reconstituted with the Glycoprotein of Vesicular Stomatitis Virus,” *Biochemistry*, vol. 19, no. 13, pp. 3088–3091, 1980.

[35] A. E. Wiacek, L. Holysz, and E. Chibowski, “Effect of temperature on n-tetradecane emulsion in the presence of phospholipid DPPC and enzyme lipase or phospholipase A2,” *Langmuir*, vol. 24, no. 25, pp. 7413–7420, 2008.

[36] M. J. Retamal *et al.*, “Surface Morphology of Vapor-Deposited Chitosan: Evidence of Solid-State Dewetting during the Formation of Biopolymer Films,” *Biomacromolecules*, vol. 17, pp. 1142–1149, 2016.

[37] D. P. Cherney, T. E. Bridges, and J. M. Harris, “Optical Trapping of Unilamellar Phospholipid Vesicles: Investigation of the Effect of Optical Forces on the Lipid Membrane Shape by Confocal-Raman Microscopy,” *Anal. Chem.*, vol. 76, no. 17, pp. 4920–4928, 2004.

[38] T.-L. Phang and E. I. Franses, “Physically self-assembled monolayers (PSAMs) of lecithin lipids at hydrophilic silicon oxide interfaces.,” *Langmuir*, vol. 22, no. 4, pp. 1609–1618, Feb. 2006.

[39] C. Steinem and A. Janshoff, “Multicomponent membranes on solid substrates: Interfaces for protein binding,” *Curr. Opin. Colloid Interface Sci.*, vol. 15, no. 6, pp. 479–488, 2010.

[40] A. C. Simonsen and L. A. Bagatolli, “Structure of Spin-Coated Lipid Films and Domain Formation in Supported Membranes Formed by Hydration,” *Langmuir*, vol. 20, no. 22, pp. 9720–9728, Oct. 2004.

[41] M. Schlame, C. Casals, B. Rüstow, H. Rabe, and D. Kunze, “Molecular species of phosphatidylcholine and phosphatidylglycerol in rat lung surfactant and different

pools of pneumocytes type II.," *Biochem. J.*, vol. 253, no. 1, pp. 209–215, Jul. 1988.

[42] "http://www.sigmaaldrich.com/ content/ dam/sigma-aldrich/ docs/ SAFC/general_Information/ 1/dppc-eqpd.pdf." .

[43] F. Hansen *et al.*, "Intramolecular Diffusive Motion in Alkane Monolayers Studied by High-Resolution Quasielastic Neutron Scattering and Molecular Dynamics Simulations," *Phys. Rev. Lett.*, vol. 92, no. 4, p. 046103, Jan. 2004.

[44] C. B. Fox, R. H. Uibel, and J. M. Harris, "Detecting phase transitions in phosphatidylcholine vesicles by raman microscopy and self-modeling curve resolution," *J. Phys. Chem. B*, vol. 111, pp. 11428–11436, 2007.

[45] T. Kaasgaard, C. Leidy, J. H. Crowe, O. G. Mouritsen, and K. Jørgensen, "Temperature-controlled structure and kinetics of ripple phases in one- and two-component supported lipid bilayers.," *Biophys. J.*, vol. 85, no. 1, pp. 350–360, Jul. 2003.

[46] A. E. Wiacek, L. Holysz, and E. Chiboski, "Under the influence of alcohol: The effect of ethanol and methanol on lipid bilayers," *Langmuir*, vol. 24, no. 14, pp. 7413–7420, Aug. 2008.

[47] M. Savva, V. P. Torchilin, and L. Huang, "Effect of Polyvinyl Pyrrolidone on the Thermal Phase Transition," vol. 165, pp. 160–165, 1999.

[48] T. Parasassi, G. De Stasio, A. D'Ubaldo, and E. Gratton, "Phase fluctuation in phospholipid membranes revealed by Laurdan fluorescence.," *Biophys. J.*, vol. 57, no. 6, pp. 1179–1186, Jun. 1990.

[49] S. N. Ahmed, D. A. Brown, and E. London, "On the origin of sphingolipid/cholesterol-rich detergent-insoluble cell membranes: physiological concentrations of cholesterol and sphingolipid induce formation of a detergent-insoluble, liquid-ordered lipid phase in model membranes.," *Biochemistry*, vol. 36, no. 36, pp. 10944–10953, Sep. 1997.

[50] W. A. Petri, T. N. Estep, R. Pal, T. E. Thompson, R. L. Biltonen, and R. R. Wagner, "Thermotropic behavior of dipalmitoylphosphatidylcholine vesicles reconstituted with the glycoprotein of vesicular stomatitis virus," *Biochemistry*, vol. 19, no. 13, pp. 3088–3091, Jun. 1980.

[51] S. J. Marrink, J. Risselada, and A. E. Mark, "Simulation of gel phase formation and

melting in lipid bilayers using a coarse grained model.," *Chem. Phys. Lipids*, vol. 135, no. 2, pp. 223–244, Jun. 2005.

[52] F. Meersman, I. Daniel, D. H. Bartlett, R. Winter, R. Hazael, and P. F. McMillan, "High-Pressure Biochemistry and Biophysics," *Rev. Mineral. Geochemistry*, vol. 75, no. 1, pp. 607–648, 2013.

[53] K. L. Willes, J. R. Genchev, and W. F. Paxton, "Hybrid Lipid-Polymer Bilayers: pH-Mediated Interactions between Hybrid Vesicles and Glass," *Polymers (Basel).*, vol. 12, no. 4, p. 745, 2020.

[54] U. G. Volkmann and K. Knorr, "Ellipsometric study of krypton physisorbed on graphite," *Surf. Sci. Lett.*, vol. 221, p. A512, 1989.

[55] G. B. Hess, *Phase Transitions in Surface Films 2*. 1991.

[56] R. M. A. Azzam and N. M. Bashara, *Ellipsometry and Polarized Light*. 1987.

[57] K. Hinrichs and K.-J. Eichhorn, *Ellipsometry of Functional Organic Surfaces and Films.* Editorial Springer, 2014.

[58] P. Drude, *The theory of optics*, Second Edi. New York, 1902.

[59] F. Jonas, "Design, construction and calibration of a null ellipsometer with high resolution," Clausthal University of Technology and Pontificia Universidad Católica de Chile, unpublished, 2019.

[60] H. G. Tompkins, *Handbook of Ellipsometry*, vol. 30. 2005.

[61] M. Wilson, K. Kannangara, G. Smith, M. Simmons, and B. Raguse, *Nanotechnology, basic science and emerging technologies.* 2002.

[62] N. Yao and Z. L. Wang, *Handbook of Microscopy for Nanotechnology.* Editorial Kluwer academic publishers, 2005.

[63] I. M. Tidswell, B. M. Ocko, P. S. Pershan, S. R. Wasserman, G. M. Whitesides, and J. D. Axe, "X-ray specular reflection studies of silicon coated by organic monolayers (alkylsiloxanes)," *Phys. Rev. B*, vol. 41, no. 2, pp. 1111–1128, 1990.

[64] H. Mo, "Neutron and X-ray scattering study of intermediate-length alkane films adsorbed on solid surfaces," 2004.

[65] E. A. Cisternas *et al.*, "Crystalline-to-plastic phase transitions in molecularly thin n-dotriacontane films adsorbed on solid surfaces.," *J. Chem. Phys.*, vol. 131, no. 11, p. 114705, Sep. 2009.

[66] R. E. Catalan, “Atomic Force Microscopy study of elastic properties of vapor-phasedeposited lipid membranes,” Master Thesis, Instituto de Fisica, Pontificia Universidad Catolica de Chile, https://repositorio.uc.cl/handle/11534/21962, 2018.

[67] L. Chopinet, C. Formosa, M. P. Rols, R. E. Duval, and E. Dague, “Imaging living cells surface and quantifying its properties at high resolution using AFM in QI™ mode,” *Micron*, vol. 48, pp. 26–33, 2013.

[68] U. Volkmann, T. Perez-Acle, S. Gutierrez, M. J. Retamal, and M. Cisternas, “U.S. Provisional Patent Application 62/037,027,” 2014.

[69] F. Palacios-Coddou, “STUDY OF ELASTIC PROPERTIES OF DPPC ARTIFICIAL MEMBRANES ASSEMBLED ON SILICON SUBSTRATES,” Bachelor Thesis, Instituto de Fisica, Pontificia Universidad Catolica de Chile, unpublished, 2019.

[70] P. Balgavý, M. Dubničková, N. Kučerka, M. A. Kiselev, S. P. Yaradaikin, and D. Uhríková, “Bilayer thickness and lipid interface area in unilamellar extruded 1,2-diacylphosphatidylcholine liposomes: A small-angle neutron scattering study,” *Biochim. Biophys. Acta - Biomembr.*, vol. 1512, no. 1, pp. 40–52, 2001.

[71] M. A. Cisternas *et al.*, “Dry two-step self-assembly of stable supported lipid bilayers on silicon substrates,” *Int. J. Mol. Sci.*, vol. 21, no. 18, pp. 1–15, 2020.

[72] A. Alessandrini, H. M. Seeger, A. Di Cerbo, T. Caramaschi, and P. Facci, “What do we really measure in AFM punch-through experiments on supported lipid bilayers?,” *Soft Matter*, vol. 7, no. 15, pp. 7054–7064, 2011.

[73] S. Garcia-Manyes, L. Redondo-Morata, G. Oncins, and F. Sanz, “Nanomechanics of lipid bilayers: Heads or tails?,” *J. Am. Chem. Soc.*, vol. 132, no. 37, pp. 12874–12886, 2010.

[74] D. I. Diaz, “Wetting Properties of n-alkane thin films to understand the adherence mechanism of articial membranes on silicon substrates,” Master Thesis, Instituto de Fisica, Pontificia Universidad Catolica de Chile, https://repositorio.uc.cl/handle/11534/21543, 2017.

[75] M. J. Dignam and J. Fedyk, “Infrared Ellipsometric Spectroscopy of Adsorbed Species,” *Appl. Spectrosc. Rev.*, vol. 14, no. 2, pp. 249–285, 1978.

[76] P. Drude, “Zur Elektronentheorie der Metalle,” *Ann. Phys.*, vol. 306, no. 3, p. 556,

1900.

[77] T. P. Corrales, “Self-Assembly of Submonolayer-Coverage Organic Films,” Master Thesis, Instituto de Fisica, Pontificia Universidad Catolica de Chile, http://repositorio.conicyt.cl/handle/10533/193507, 2009.

[78] Y. Mnyukh, “Second-order phase transitions, L. Landau and his successors,” *Am. J. Condens. Matter Phys.*, vol. 3, no. 2, pp. 25–30, 2013.

[79] L. Landau, “On the theory of phase transitions in polypeptides,” *Zh.Eksp.Teor.Fiz.*, pp. 19–32, 1937.

[80] K. Sengupta, V. Raghunathan, and J. Katsaras, “Structure of the ripple phase of phospholipid multibilayers,” *Phys. Rev. E*, vol. 68, no. 3, p. 031710, Sep. 2003.

[81] S. J. Attwood, Y. Choi, and Z. Leonenko, “Preparation of DOPC and DPPC supported planar lipid bilayers for atomic force microscopy and atomic force spectroscopy,” *Int. J. Mol. Sci.*, vol. 14, no. 2, pp. 3514–3539, 2013.

[82] N. N. Gosvami, E. Parsons, C. Marcovich, M. L. Berkowitz, B. W. Hoogenboom, and S. Perkin, “Resolving the structure of a model hydrophobic surface: DODAB monolayers on mica,” *RSC Adv.*, vol. 2, no. 10, pp. 4181–4188, 2012.